Confidential

Monitoring the dynamic behaviour of a free-hanging deep sea riser

S.C.W. de Jong

Master of Science Thesis

Delft University of Technology

Offshore Engineering

MSCCONFIDENTIAL

Monitoring the dynamic behaviour of a free-hanging deep sea riser

Master of Science Thesis

For the degree of Master of Science in Offshore Engineering at Delft University of Technology

S.C.W. de Jong

February 10, 2017

Faculty of Mechanical, Maritime and Materials Engineering (3mE) · Delft University of Technology

The work in this thesis was supported by Royal IHC. Their cooperation is hereby gratefully acknowledged.

Delft University of Technology
Department of
Offshore and Dredging Engineering (ODE)

Monitoring the dynamic behaviour of a free-hanging deep sea riser

by

S.C.W. de Jong

Dated: February 10, 2017

Graduation committee TU Delft:	prof.dr.ir. R.H.M. Huijsmans
	dr.ir. J.W. van Wingerden
	dr.ir. P. Wellens
Graduation committee Royal IHC:	ir. W.B.A. Boomsma

Abstract

In deep sea mining polymetallic nodules are harvested that are found in large parts of the oceans at depths of up to 5000 metres. A deep sea mining system collects such nodules using a seabed crawler and transports them to a continuously sailing ship by pumping them via a jumper through a free-hanging riser. The position of the seabed crawler must be known for two main reasons. Firstly, object on the seabed spotted in bathymetric surveys can be avoided. To this end monitoring should be done in real time. Secondly, the crawler can follow optimized mining patterns depending on the seabed lay-out.
Use of conventional subsea positioning techniques such as short and long baseline systems is inaccurate or expensive. Using a short baseline system leads to inaccurate results due to the large depth and surrounding noise created by the deep sea mining system, while using a long baseline system requires a vast array of subsea transponders since the crawler is constantly moving. Because the ability to actively respond in case of an unexpected situation is desired the crawler position must be known in real time. The position of the crawler relative to the position of the tip of the free-hanging riser can be determined. This means that if the position of the tip of the free-hanging riser is known the position of the crawler can be obtained. In this thesis project a system is proposed that determines the position of the tip of the free-hanging riser.

All observations are made in two dimensions to reduce computational time. An estimation of the position of the tip of the riser is made in two steps. First a finite element model of the riser is made that is used to estimate the deflections of the free-hanging riser. As a second measurements are done at the booster stations along the riser. The model estimations and measurements are combined using a Kalman filter in an attempt to increase the estimation accuracy.
Combining the finite element model with measurements improves the position estimation compared to a system using only a finite element model or only measurements. A system creating a position estimation in two dimensions can do this in real time. An optimal estimation is not reached, as a steady offset remains that cannot be filtered out. It is attempted to decrease this offset by adding temporary position measurements. Adding position measurements improves the accuracy of the estimated position, but the improvement does not last

when position measurements are lost.
Reducing the steady offset can be achieved by improving the estimation made by the finite element model. The results can be improved by maintaining the accurate results obtained from temporary positions measurements. This could be done using a system capable of altering the finite element model parameters. For Royal IHC, it will be important to determine a minimum position accuracy that is required to get a profitable mining operation.

Table of Contents

List of Figures

List of Tables

Chapter 1

Introduction

This introductory chapter first discusses the background of the thesis project. A description of how the deep sea mining system should operate is included in order to understand the requirements of the subsystem that is the focus of this thesis. Next the challenge that is addressed in this work is explained, leading to the main research question and the project approach. For a more extensive read of the entire process of deep sea mining and some history of deep sea mining, the reader is referred to (Smit et al., 2014; Stanislav et al., 2014; Heydon, 2012).

1-1 Background

Within the Blue Mining project, Royal IHC is developing a deep sea mining system that can harvest large volumes of polymetallic nodules from depths of up to 6000 metres. This system can be divided into four main components which are seen in figure 1-1.

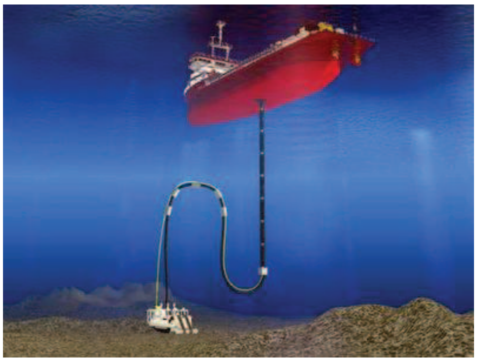

Figure 1-1: Deep sea mining system (Blue Mining, 2013)

Driving around on the bottom of the ocean is the Seafloor Mining Tool (SMT). The SMT, also referred to as crawler, is designed to harvest polymetallic nodules of the sea bed and separate them from most of the sediment. The SMT manoeuvres the seabed using its own propulsion and steering. A slurry of leftover sediment and nodules is then pumped to the Vertical Transport System (VTS) via a flexible riser, also referred to as jumper. The jumper allows the distance between the SMT and the VTS to vary, and it provides power to the propulsion and separation mechanisms of the SMT. Attached to the flexible riser is the VTS. The VTS, also referred to as riser or free-hanging riser, is a five kilometre long steel pipe with booster stations that transfers the slurry of harvested nodules, seawater and sediment to the Mining Support Vessel (MSV). This free-hanging riser is built up like a drill-string and tensioned by a clump-weight at the tip of the riser. The MSV is a ship that processes the nodules harvested from the seabed.

Position monitoring

The nodules that are being harvested are located in large fields at depths of 3500 to 6000 metres. The clarion clipperton zone (figure 1-2) with a size of approximately 9 million square kilometres is one of the largest areas in which nodules are found.

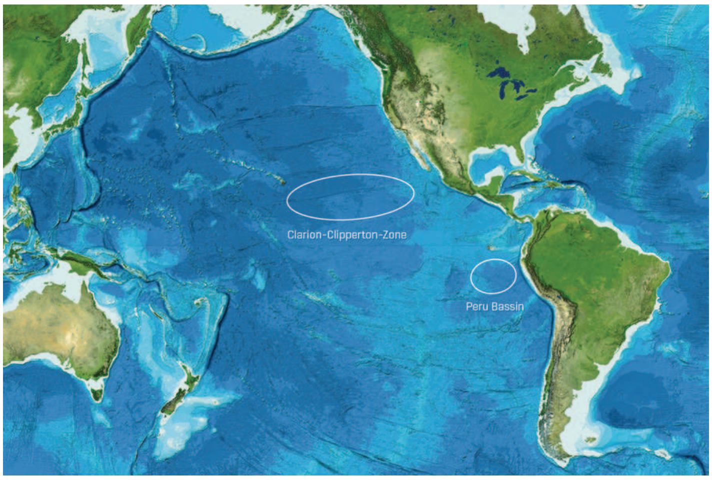

Figure 1-2: Clarion clipperton zone (Vella, 2013)

When the deep sea mining system becomes operational, the MSV and the crawler will be constantly moving at an average pass of $0.5m/s$. The movement of the SMT through the area that is being mined needs to be monitored for two reasons.
Firstly, if the position of the crawler is known damage to the system can be avoided. In the area that is being mined trenches, hills, rocks and debris can be spread over the seabed surface. The lay-out of the seabed can be obtained from seafloor bathymetric surveys. If the position of the crawler is known obstacles can be avoided. Also the jumper has a finite length, if the motions of the crawler and the tip of the riser are known it can be avoided that the distance between the two becomes too large. The jumper is not designed to transfer force, tensioning it can damage the system.
Secondly, if the coordinates of the crawler are known it can be recorded which parts of the seabed have already been mined. Since the nodules are all in the top layer of the seabed it is sufficient to crawl across each part of the seabed only once. The crawler empties the seabed by creating parallel lanes, when the coordinates of the SMT are accurately known the risk of

mining an area of seabed twice is minimized. If the coordinates of the SMT are accurately known, the distance between two parallel lanes can be kept to a minimum so the amount of material that can be harvested per mining area is maximized.
The position of the crawler can be monitored using conventional techniques like short and long baseline systems, but it is expected that these techniques will fall short in this application. Short baseline systems perform determine the subsea position of an object using a sonar pulse sent from the sea level. The large depth at which the SMT is used and noise generated by the booster makes this technique inaccurate. Also the updating rate is slow since sound travel through seawater with a speed about $1500 m/s$. A long baseline system should be accurate, but it is expected that this will take a large array of subsea beacons due to the size of the area that is mined.
However it is possible to determine the position of the SMT relative to the tip of the riser. The distance between the two is short enough for a technique like fibre-optic monitoring or sonar to work. This way, in order to obtain the crawler positions, only the motions of the clump-weight have to be monitored.
Monitoring the position of the clump weight can be done by estimating the deflection of the entire riser. A model of the riser can be made, that simulates the riser behaviour from top to bottom. This way the position of the clump weight can be related to the position of the ship. Using this relation, and the known distance between the clump-weight and the crawler, the position of the crawler is determined.

Measurements

A model of a large system as the VTS is never able to fully describe the riser behaviour. Internal and external effects that are unknown, and often assumptions are made that allow for a simpler model setup. These unknown or neglected properties create uncertainties in the model. To improve the model it can be combined with measurements that can be taken in real-time. Positions cannot be obtained, but it is possible to acquire data like accelerations, relative current velocity and angles of the riser. These measurement units serve two functions. First, measurements form a reference to the real world system. By actively measuring data, inputs to the system and states of the system can be estimated. This way external effects can be modelled more accurately. Second, the measurements can be used to decrease the computational power required by the riser model. Why a decrease in computational power is desired is explained in the next subsection.

Real time monitoring

Monitoring the motions of the riser must be done in real time, so the SMT can be actively controlled to avoid damage and optimize nodule harvesting. This also allows for direct intervention in the case of unexpected circumstances. In order to achieve real-time monitoring, a riser model has to be created that is both computationally fast and accurate when measuring tip positions. This means a trade-off has to be made between computational efficiency and accuracy.
Combining a model with measurement data can decrease the computational power required by a model, while keeping the accuracy. The riser is exited by external influences, both linear and non-linear. Taking all influences into account in the model makes the model accurate but

computationally expensive. If a lot of measurement units are placed and these measurement units update at a very high frequency, a simple model can be used to describe behaviour between two measurement points, because the motions vary little over a small distance. When less measurement units are used the harder it is to describe the dynamic behaviour of the beam between two measurement points, so a more accurate description of the behaviour between two point is required. Placement of the measurement units is restricted to the booster stations where power and data transfer infrastructure is available.
The aim of this thesis is monitoring the position of the clump weight in real time, by combining a riser model and measurements.

1-2 Problem analysis

Research is done in current literature to obtain information on how the challenge in this thesis can be solved. Information on techniques that deal with similar problems, or that provide information about parts of the problem is searched for. Research is done on free-hanging deep sea risers. Also techniques that are used in structural monitoring, both in subsea and non-subsea situations, are researched in order to find a technique that can be used to model or monitor the riser.

Position monitoring

Research on tracking objects above water is found in abundance. The tracking of objects is done by combining measurements with a numerical model that estimates the behaviour of the object. Estimates and measurement are combined using a Kalman Filter (KF), for example when determining the position of a ship (Cadet, 2003). Subsea position monitoring is also done using a KF, but no examples are found that do not include an acoustic reference signal. The use of a KF requires a model that can estimate the behaviour of the riser.

Free-hanging risers

Information specifically about free-hanging subsea risers is searched in order to find out if a technique exists that can be used to monitor the tip of the riser without using position measurements.
An application in which it is important to monitor the position of the tip of a free-hanging riser is in deep-sea drilling. When the drill string has to re-enter the well the position of the tip of the system needs to be known. The method used to do this is described in (Australian Drilling Industry Training Committee Limited, 2015). In this application a subsea beacon is used which uses an acoustic signal to determine distance to the drill hole.
Research about vibrations in water inlet pipes was done by (Kuiper and Metrikine, 2005). This research is mainly about vibrations created by the suction behaviour of the pipe, which are not an issue in the free hanging riser in the deep sea mining system. The modelling techniques that are described in this paper are interesting and can be used for modelling the riser in this thesis. Parametric resonance in free-hanging ultra-deep sea risers was researched by (Yang and Li, 2009). The work uses no measurement inputs or updating algorithm but it is an interesting paper because it is one of the little papers which is about free-hanging

marine risers. Like in (Kuiper and Metrikine, 2005), some of the modelling techniques used can be usefull.
A study about deep-water drilling riser fatigue monitoring has been performed by (Li et al., 2014) and deep-water drilling riser fatigue is described by (Xu et al., 2011). In the study performed by (Li et al., 2014) acoustic positioning is used to monitor the fatigue of a riser connecting from platform to well head. Sea trials are performed which confirm the results from the model used. This work uses acoustic signals, if the acoustic system will work in combination with noise generated by the Deep Sea Mining (DSM) system is unknown. Also the time delay due to the maximum velocity of sound in water of about $1500m/s$ in a system which reaches a depth of 5000 metres is expected to be too large.

Structural monitoring

Full size monitoring of structures is a technique often used for structural health monitoring and is a common technique in many applications, ranging from subsea pipelines and risers to aerospace composites. Several techniques are being used in these fields, fibre-optic monitoring is popular in subsea and aerospace applications, inertial measurement units are often used when monitoring large structures like bridges.
Fibre-optic monitoring techniques are described by (Brower et al., 2004; Jacques et al., 2010; Clarke et al., 2011; Pipa et al., 2010) for subsea riser applications. The same technique is also used in other applications like wind-turbine design (Pedrazzani et al., 2012). The technique uses fibreglass cables over the full-length of the riser or wind-turbine that is being monitored. These cables can either be attached to or encased in the housing of the system. The technique of monitoring risers by fibre-optics is owned by multiple companies. Attaching equipment to the riser over the full length of the riser is not an option, but using a similar technique over small sections might be usable. Also this technique can be used to accurately obtain the shape of the jumper that connects the clump-weight and the MSV.
Research using point-based measurement units, like inertial sensors, in subsea applications has also been done, like the offline analysis of Vortex Induced Vibrations (VIV) by (Kaasen et al., 2000). Results in on-line riser monitoring are found by (Karayaka et al., 2009), this research focuses on stresses in the touchdown and hang-off region of the submerged riser. Optimization of sensor placement in order to capture VIV response was done by (Natarajan et al., 2006). These researches are about steel catenary risers, but usefull information about the different measurement units that can be used is found.
Examples of non-subsea structural health monitoring are found in (Qing et al., 2012) for an aerospace application and (Ko and Ni, 2005; Miao et al., 2013) about the monitoring of large-scale bridges. In these works the placement of the sensors is carefully selected in order to obtain accurate results. Also the monitoring models described in these papers do not have to run in real time which makes it possible to create a computationally expensive model in order to obtain accurate results. In (Miao et al., 2013) a technique called Operational Modal Analysis (OMA) is used. This technique is used to obtain the frequency response of a system with unknown input excitations. The obtained frequency response is then compared to the frequency response function of the design model and then used to update the design of the model so that the dynamic behaviour of the design model more accurately represent the real system behaviour. This technique could be used to create a more accurate model of the VTS.

Real time modelling

The constraint that the model has to be able to run in real-time appears to be a challenge. There are tools that are able to simulate the behaviour of the VTS, Royal IHC for instance uses an in-house developed tool named VIVID. This is a design-tool, built to take linear and non-linear influences on the system into account and built to create simulations that are as accurate as possible when compared to real world riser behaviour. This makes that the tool requires a large amount of computational power. Even though design tools create relatively accurate predictions of system behaviour, a model will never show identical behaviour to the real world situation because of unknown external influences, or external influences not fully accounted for in the simulation can have a lot of influence. Existing design-tools can be used in order to create simulation data. Because the system has not yet been build or tested at the moment there is no reference data to compare output to. A simulation in the time domain created by a design tool can be used as 'real world' input in the system.

Conclusion

Summarizing research has been found about position tracking, which is often done by combining a model that can estimate system behaviour with measurements. The estimation from the model and the measurements are then combined in a KF. Subsea position tracking is used in situations where the object of interest, often an ROV, stays within a confined area where its position can be referenced to an acoustic position measurement.No research on subsea position tracking without position measurements was found.
Further is has been researched how a model of the free-hanging riser can be made that can estimate the riser movements. It was found that this is often done in structural monitoring applications. In multiple fields research is done about structural health monitoring but this research focuses on damage detection and high frequency vibrations that cause fatigue. In this field measurement techniques are used that can also be used to provide measurement information about the riser. A system designed to capture the tip motion of a drill string was found, but this system is designed to determine the offset to a specific location and not to track the system over distances. Also in this system a subsea beacon is used.
Riser design tools do exist but they require a lot of computational power and lack the ability to use real world input data. A system able to monitor the positions of an object moving subsea in a large area, without position measurements and in real time is not found in current literature.

1-3 Research questions

Based on the problem analysis from the previous section a main research question can be obtained which is defined as follows:

How can the position of the clump-weight of the VTS be monitored using limited observation points?

This main question is accompanied by sub questions that structure the research and must be answered in order to obtain a conclusion on the main question.

- What can be measured at the booster stations?
- How accurate is an approximate model compared to design tool data?
- How accurate can an approximate model combined with a Kalman filter track the position of the tip of the riser?

The research questions are answered during the thesis and the results are discussed at the end chapter of 7.

1-4 Approach

The aim of this research is to create a system that can track a real world VTS in real-time. A model of the riser will be created that can be combined with measurements using a Kalman filter. The model of the riser, referred to as approximate model, is created by using a numerical method with known and unknown external influences. In order to keep the required computing power and time low not all influenced are calculated, but depending on their influence they are either estimated or neglected. At first a study has to be done about the external and internal effects and their role in the dynamic behaviour of the system. This will provide insight in what part of the system can be estimated, what can be assumed to have a negligible effect or is important and has to be included properly.
Existing models used to create simulations take longer than real time to generate data. In order to have a model that can run in real-time, the existing model needs to be simplified, while keeping the monitoring accurate. An approximate model of the system runs faster but with decreased accuracy, so a solution to the loss of accuracy has to be found. A solution is sought in adding measurements to the system. The simplified model will be updated using data measured at different points along the riser. This provides a calculated estimate of the system which can combined with a measured estimation of how the system is moving. These estimations are combined using a KF. Creating a simple model will be done using the finite element method.
At the moment there is no measurement data about the system, because (full) scale riser tests have not yet been done. To create measurement data that can serve as an input to the KF, several simulations are run using a riser design tool to create reference data. The data generated by these simulations is then processed so only data from the points on which the real world system can measure is used. This data is then contaminated with noise which resembles sensor influence.

1-5 Thesis Layout

In chapter 2 an overview of different measurement units and their advantage and limitations is given. The theory about the approximate model and the Kalman filter is explained. Also a short description is given about the design tool used to create measurement data. In chapter 3 it is explained how the approximate model is build. Also the verification of the approximate model is done in this chapter. Chapter 4 explains how the linear KF is implemented. It is checked for stability and verified. In chapter 5 the sensitivities of the full system are checked. The response to variations in process noise, varying measurement frequencies and biased sensors is checked. After the sensitivities have been checked the system with a KF that performs best is compared to the model results without a KF in chapter 6. In this chapter it is also tried to improve on these results. Chapter 7 contains the conclusions and discussion, in chapter 8 the final recommendations are found.

Chapter 2

Literature

In this chapter parameters and methods that are used in order to build the final system are described. As a first options for measuring around the booster stations is looked at. Several techniques are described and one or more suitable techniques are chosen. In the next section the theory used to create a model of the riser and the parameters that make up the riser are described. Also external exiting forces are accounted for. This is followed by a description of the Kalman Filter (KF). In the last section a short description of techniques used by VIVID to create a model is given so the approximate model theory can be compared to that of the VIVID model.

2-1 Subsea measuring

At first acoustic positioning is reviewed, a technique commonly seen in subsea applications (Tomczak, 2011). Measurement techniques using fibre-optics and inertial sensors are introduced in section 2-1-2 and section2-1-3. Due to the large depths the visibility is extremely limited which makes visual observation not an option. In the end a conclusion is drawn and one or more techniques are chosen where the goal is monitoring the motions of the entire Vertical Transport System (VTS).

2-1-1 Acoustic positioning

The first technique that is researched is acoustic underwater positioning. Underwater positioning techniques were developed in the 1950s, and are commonly found in offshore applications (International Marine Contractors Association, 2014). Since the 1950s the technique has undergone a lot of technological changes, but the principle is still the same. A SOund Navigation And Ranging (SONAR) transmitter sends out an acoustic pulse, often called a 'ping'. This pulse is reflected and received again by the transmitter. Based on the difference in time between the transmitted and received pulse a range can be determined. Acoustic signals are used because compared to other forms of radiation, sound travels best through

water.
Acoustic positioning systems come in a few different forms, all with their advantages and disadvantages. All of the systems have to deal with the depth and the surrounding noise created by the booster stations. SONAR accuracy is goes down with an increase in range and the signal quality is highly dependent on background noise (Yu et al., 2005).

Long baseline

The Long Baseline system (LBL) works by deploying multiple beacons or transponders in an array which are set to transmit when triggered by a hydrophone (International Marine Contractors Association, 2014). The positions of these transponders have to be calibrated. When the range from at least three of the transponders to the hydrophone is known the position of the hydrophone can be determined. When more transponders are deployed the position of the hydrophone can be determined with a higher accuracy. With multiple hydrophones placed along the length of the riser this system has the potential to provide accurate measurements of the motions of points along the riser.

Downsides to this technique are that the field which has to be monitored is too large to be covered by a small amount of transmitters and receivers. Distance between transponders is limited to a few kilometres and with the Mining Support Vessel (MSV) sailing at about $1.8km/h$ it will be out of range within an hour. Setting up and calibrating many subsea beacons is an expensive and time consuming job. Another downside is that the update frequency of this system would be low, because sound travels trough seawater at a speed of about $1500m/s$ position updating would take multiple seconds. Also the influence of the noise created by the equipment makes it uncertain if reliable data can be obtained.

Short baseline

Short Baseline system (SBL) systems are different compared to LBL systems because they don't make use of fixed underwater transponders. The SBL system positions itself relative to the position of the surface vessel (International Marine Contractors Association, 2014). Through the hull two transducers are deployed with some tens of meters space between them. Based on the range of the object relative to these transducers the location of an object can be tracked. Just like the LBL this system could be used if on several points along the riser transponders are placed. The positions of these transponders should then be determined by a pulse. This system has the advantage that is easily deployed and the system travels with the MSV.

Downside to this way of measuring is that all of the pulses travel almost parallel with the VTS which generates a lot of noise potentially making the measurements unusable. Also due to the motions of the riser, transducers could be temporarily blocked if they are on the inside of a bend.

Ultra short baseline

The Ultra Short Baseline system (USBL) works in the same way as the SBL but it uses a short single combines transmitter and hydrophone for receiving and generating pulses (International

Marine Contractors Association, 2014). The transducer is installed through the hull of the ship and provides a direction and a range of the observed system. This technique has been investigated by (Li et al., 2014) for a drilling riser connected to the seabed.

Calibrating this system has to be done very careful and can take up a lot of time. Further it is unknown what the influence of the noise generated by the entire deep sea mining system on the accuracy will be. Also the low update frequency due to the limited speed of sound through water makes the system less usable.

Global Positioning System (GPS) buoy

A way to measure the position of the clump weight using multiple transmitters is using GPS buoys. These buoys can be placed away from the ship in an array like the LBL. But unlike this system the transponders are not placed on the seabed but they are attached to buoys at the sea surface. This makes it easier to position and reposition the buoys and they can keep track of their position using GPS. The update frequency and the accuracy of the measurements will still cause problems.

2-1-2 Fibre-optics

Another technique which is often used in structural monitoring systems is monitoring using fibre-optics (Clarke et al., 2011; Jacques et al., 2010). Fibre-optics strain measuring can be found in many applications, from aerospace (Qing et al., 2012) to subsea (Brower et al., 2004; Glisic, 2013) applications. The technique works by placing a fibreglass cable onto the subject which is being monitored or by encasing it in the structure (Pedrazzani et al., 2012). Fibre-optic sensors can be placed at certain points of the riser, in a few short lengths. These sensors can be used to measure strain and temperature. Positive about these sensors is that they are corrosion resistant, immune to electromagnetic interference and can transmit data to the MSV very fast. Feasibility of these fibre-optic sensors has been proven in full-scale tests (Brower et al., 2004). Applying fibre-optic cables along the length of the riser is challenging because the VTS is build up in multiple sections like a drillstring. This makes it hard to attach the cables properly to the riser.

2-1-3 Inertial measurement units

An Inertial Measurement Unit (IMU) is a combination of accelerometers and gyroscopes which is used to measure angular velocity and accelerations. These kind of sensors are used in a lot of applications, ranging from submarines to your cellphone. Data from these devices can be used to obtain information about accelerations and angles of the device. Multiple IMU's can be placed at the booster stations in order to track accelerations above and below the booster stations.
A downside of an accelerometer is that it will start to drift over time, creating offsets of hundreds of metres within minutes (Woodman, 2007), which is confirmed by tests in appendix G. When integrating accelerations in order to determine the velocity and the position of the system the sensors will not be able the accurately monitor the position for long. An acceleration sensor will have to have a high accuracy and little noise, since accelerations in

the system are expected to be low.
The most accurate accelerometers available to the market are those with navigational grade specifications. Characteristics for the sensor used in this thesis can be found in table 2-1 or in (Zwahlen et al., 2010). The noise standard deviation is added to the measured signals.

Parameter	**Value**	**Unit**
Input range (max)	± 11.7	g
Accuracy standard deviation	1.7	$\mu g/\sqrt{Hz}$
Bias stability (24hrs)	0.1	mg

Table 2-1: Inertial measurement sensor characteristics

Temperature offsets are expected to be mitigated by temperature sensors so they will not be of influence.

2-1-4 Angular sensors

An angular sensor is a sensor that can measure the angle at which an object is, starting from a calibration point zero. One of the most accurate way to measure angle variations of by using an optical gyroscope (Woodman, 2007). Even though an optical gyroscope measures the angular velocity of an object it is assumed to be more accurate than pendulum sensors or MicroElectro Mechanical Systems (MEMS) gyroscopes. In total thirteen angular sensors can be used in the system, two at every booster station (one at the top and one at the bottom) and one at the ship. The input rate and angular random walk of the sensor are found in (Honeywell, 2016).

Parameter	**Value**	**Unit**
Input rate (max)	900	$^\circ/s$
Accuracy standard deviation	0.0035	$^\circ$
Angular random walk	0.0035	$^\circ/\sqrt{hr}$

Table 2-2: Angular sensor characteristics

An assumption has been made for the accuracy standard deviation based on the gyroscope its bias stability. Just like with the IMU described in the previous subsection temperature fluctuations are expected to be of negligible influence if the temperature can be measured at the gyroscope.

2-1-5 Current velocity meter

Another sensor that can be placed at the top and bottom of the booster stations are current velocity meters. These meters measure the velocity of the current, relative to the velocity of the riser at that point. When placing the meters it has to be taken into account that the meters are not placed too close to the riser where the flow is disturbed.

Parameter	**Value**	**Unit**
Input range	0.03 to 5	m/s
Accuracy standard deviation	1.5	%
Bias stability	0.03	m/s

Table 2-3: Flow sensor characteristics

Data for this meter from table 2-3 has been found in (Valeport, 2016). In the datasheet no bias is mentioned so an assumption for the bias of the sensor has been made, based on the input range.

2-2 Riser model

In this section the technique used to create the approximate model is described. Modelling in sub sea conditions creates some effects that are not found on land. Apart from the decreased ability to observe the behaviour of the VTS, effects that are negligible above sea level, like viscous damping and added mass, have a large influence subsea.

2-2-1 Reference frame

The reference frame that is used throughout this thesis is seen in figure 2-1. All of the displacements in x-direction and in z-direction are measured from the MSV. This means that if a point along the riser has a deflection in x-direction of $100m$, it is $100m$ behind the ship. So if the riser at an arbitrary point is moving with a velocity of $0.1m/s$ in the x-direction, this velocity is measured independent from the speed of the MSV.

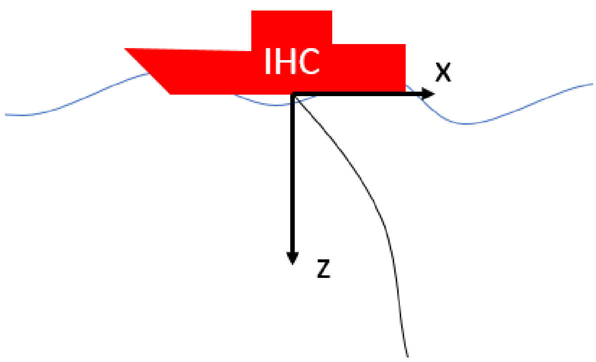

Figure 2-1: Reference frame

The MSV itself has a sailing speed as well which introduces a variation in the flow introduced on the riser. This would mean that the position x of the ship constantly varies. In order to keep the position of the ship at $x = 0$, which simplifies simulations later on, the current velocity is defined as the sailing speed of the ship combined with sea currents which are assumed to flow in the opposite direction of the ship. So if the ship is sailing with a velocity of $0.5m/s$ and a current of $0.1m/s$ is present the current velocity is said to be $0.6m/s$ and the ship velocity is set to $0m/s$.

2-2-2 Beam theories

Because the VTS is modelled in two directions a Finite Element Method (FEM) technique has to be implemented that can account for transverse motion and rotations. In FEM modelling these kind of problems are most often solved by using beam structures. There are two beam models which are commonly used, the Euler-Bernoulli beam and the Timoshenko beam model. The main difference between these two methods is that the Timoshenko beam model takes shear deformation into account and the Euler-Bernoulli beam does not. Deformation of the Timoshenko beam is different to the deformation of the Euler-Bernoulli beam because the imaginary line perpendicular to the center line, dotted red in figure 2-2, does not stay perpendicular when the beam is subject to bending in the Timoshenko model. This is the case with the Euler-Bernoulli beam as can be seen in the same figure.

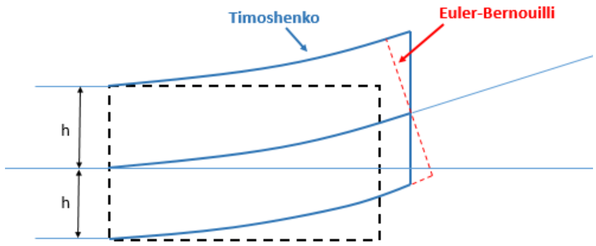

Figure 2-2: Bending beam

Euler-Bernoulli beams are best in long and slender flexure dominated problems, Timoshenko beams perform best in shear dominated problems. The VTS is seen as a long and slender beam since its length is at many times larger than its diameter. Therefore motions of the VTS are modelled using the Euler-Bernoulli beam model.

2-2-3 The Euler-Bernoulli beam

The beam equations used in this thesis have been derived in several textbooks on dynamics. In this chapter a short recollection of the equations is given. The equations derived in this section are the equations for a linear Euler-Bernoulli beam. More information on the derivation of the equations of the Euler-Bernouilli beam are found in (Carrera et al., 2011).

Analytical beam

For a beam with a distributed load q the vertical balance of forces is given by equation 2-1.

$$\rho A \Delta w \frac{\delta^2 w}{\delta t^2} = -V(z) + V(z+\Delta z) + q\Delta z = dV + q\Delta z \tag{2-1}$$

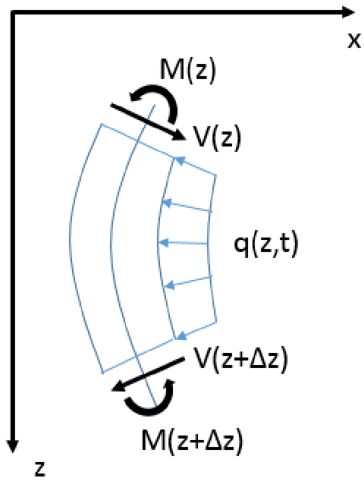

Figure 2-3: Beam section δz

The balance of moments seen in figure 2-3 is described by equation 2-2

$$V = \frac{\delta M}{\delta z} \tag{2-2}$$

Equation 2-1 is divided by Δz and after taking the limit $\Delta z \to 0$ and combining equations 2-1 and 2-2 the following equation is derived

$$\rho A \frac{\delta^2 w}{\delta t^2} = \frac{\delta V}{\delta z} + q \tag{2-3}$$

From the Euler-Bernoulli theory

$$M = -EI \frac{\delta^2 w}{\delta z^2} \tag{2-4}$$

Combining these equation results in the standard equation, equation 2-5, for a non-tensioned beam with a distributed load $q(z,t)$. In this equation x is the beam deflection at a point along the z-axis.

$$EI \frac{\delta^4 w}{\delta z^4} + \rho A \frac{\delta^2 w}{\delta t^2} = q(z,t) \tag{2-5}$$

2-2-4 Boundary conditions

In order to be able to solve the systems the boundary conditions of the system have to be defined. The hangoff point of the VTS will be a gimball system which can be seen in 2-4.

The gimball system is commonly used in the offshore industry and allows the riser to rotate at the connection point. Movement in the horizontal plane is not compensated for by the

Figure 2-4: Riser hang-off gimball (solutions, 2016)

system, at the MSV the gimball allows the VTS to rotate. When defining the boundary conditions it is assumed that there is an imposed movement at $z = 0$ and that the gimball allows for enough rotation to assume the system is hinged at the top.
At the bottom of the VTS is the clump-weight and the flexible riser that attaches the VTS to the Seafloor Mining Tool (SMT). It is assumed that the flexible riser does not influence the movement of the clump-weight, because the weight of the flexible hose is small compared to that of the clump-weight. Also the flexible riser takes the form of an s-bend which minimizes the tension force between the SMT and the clump-weight. Therefore the tip of the VTS is assumed to be free-hanging.

2-2-5 Added mass

When submerged the movements of the pipe will move the surrounding seawater as well. The mass of the fluid displaced by the cylinder adds hydrodynamic inertia to the system and is called added mass, written as m_a. The formula for added mass on a submerged cylinder is provided by (Kennard, 1967).

$$m_a = \rho_{sea} \frac{\pi}{4} D_o^2 \tag{2-6}$$

In this equation ρ_{sea} is the density of seawater and D_o is the outer diameter of the cylinder. The added mass is measured in kg/m and is added to the mass matrix in the equations of motion of the beam derived in section 2-2-3.

2-2-6 Damping

Damping is the rate at which energy dissipated from the system. Energy is dissipated by external damping influences, like the viscous damping from the seawater surrounding the VTS, but also from internal influences, this is called 'material damping'. The damping in a system is hard to estimate in a system, therefore techniques like Experimental Modal Analysis (EMA) have been developed which are used to measure damping ratios at varying frequencies. It is assumed that using material damping is sufficiently accurate and that its effect will be barely noticed, since viscous damping in the system is expected to be dominant.

2-2-7 Tension force

Tension is a very important aspect in the system. The riser is tensioned by its own weight and by the the clump weight at the end of the riser. Without tension, the hinged riser would be start moving with very large amplitudes, like an untensioned string.
The tension force is added to the system as an extra stiffness term. Most of the tension in the system comes from the weight of the steel of the riser, minus the buoyancy provided by the water surrounding the water. Adding to the tension is the density of the slurry transported in the pipe and the mass of the clump weight at the end of the riser. The tension force per meter is calculated using equation 2-7.

$$T = A_{st} * \rho_{st} + A_{in} * \rho_{sl} - A_o * \rho_{sea} \tag{2-7}$$

The tension force is added to the beam equation as

$$EI\frac{\delta^4 w}{\delta z^4} + \rho A\frac{\delta^2 w}{\delta t^2} = \delta\left(T\frac{\delta w\left(z,t\right)}{\delta z}\right) + q(z,t) \tag{2-8}$$

2-2-8 Drag force

Relative current along the length of the riser creates the largest forces on the riser. The relative current is calculated by taking the velocity of the riser at a point along the riser and adding the current velocity at that point. Over the length of the riser this force can vary, since subsea currents can vary over the length of the riser. At the top of the VTS currents are created by waves as well. The current velocity can be measured at the booster stations.

Morison equation

Morrison's equation can be used in order to estimate the force exerted on the riser by the velocity of the water relative to the velocity of the riser. The Morison equation gives the force on a standing body in the direction of the flow as:

$$F_{drag} = \rho C_m V \dot{u}_{cu} + \frac{1}{2}\rho C_d A u_{cu}|u_{cu}| \tag{2-9}$$

In equation 2-9 $F(t)$ is the drag force, u_{cu} the velocity of the surrounding water and C_d and C_m a dimensionless drag and inertia coefficient respectively. The equation can be divided into an inertia force $F_I = \rho C_m V \dot{u}_{cu}$ and a drag force $F_D = \frac{1}{2}\rho C_d A u_{cu}|u_{cu}|$. V is the displaced volume of the riser and A is the projected area, the diameter times section length. The inertia force will only play a role at the surface where waves still contribute to the force on the cylinder, which is on a relatively small part of the entire system. When moving down the riser it is assumed the inertia force becomes negligible quickly.

Moving body

When the body that is being observed is moving as well the Morison equation is adjusted as in equation 2-10

$$F_{drag} = \rho V \dot{u}_{cu} + \rho C_a V \dot{u_{cu} - \ddot{w}} + \frac{1}{2}\rho C_d A \left(u_{cu} - \dot{w}\right)\left|u_{cu} - \dot{w}\right| \tag{2-10}$$

This adjustment makes the drag force dependent of the relative velocity between the riser and the water, where $\dot{x}$ is the velocity of the riser. Values for the drag coefficient can be derived by calculating the Reynolds number 2-11 and finding the appropriate C_d value for this number (Journée and Masie, 2001).

$$Re = \frac{u_{cu}\, D}{\nu} \tag{2-11}$$

In table 2-4 the outside diameter of each section, and the outside diameter of the booster stations can be found. ν is the kinematic viscosity of seawater and u_{cu} the velocity of the flow. When the VTS reaches a steady-state the mean relative flow velocity will be equal to the velocity of the ship.
It is assumed that the flow velocity is constant at $0.5m/s$ and the seawater has have a uniform temperature of $10 \deg C$. From (Journée and Masie, 2001) it is found that flow is subcritical around the different riser sections which gives a drag coefficient of $C_d = 1.2$.
The flow around booster stations becomes supercritical due to the increased diameter of the booster stations, for the booster stations a drag coefficient of $C_d = 0.62$ is used.

2-2-9 Wave forces

The MSV will be sailing at open sea where it will encounter irregular waves. When a wave current profile is assumed as described by wheeler stretching (Journée and Masie, 2001) the current and inertia force induced by the waves on the motions only work on the top part of the system. Motions induced by these forces at the tip of the VTS are be assumed to be negligible. The waves do move the ship around, the gimball system can compensate pitch and heave motions, but not surge motions caused by waves. Wave influences on the MSV have been simplified to an imposed low frequency movement at the top of the VTS.

2-2-10 Vortex Induced Vibrations (VIV)

One of the effects submerged long and slender structures encounter are VIV. When asymmetric vortices form around a cylinder moving this creates a lift force. These lift forces cause the cylinder to shift in a direction perpendicular to the flow. VIV is a non-linear effect that can significantly reduce the fatigue life of a system. It also influences the overall drag on the system.

Cross-flow VIV

Cross-flow VIV are vibrations that make the cylinder move perpendicular to the flow direction. The cross-flow motions are high-frequency, small amplitude vibrations. More detailed information is found in (Blevins, 2001; Larsen).

In-line VIV

The in-line VIV is an effect is directly linked to the cross-flow VIV. Cross-flow vibrations increase the drag, an effect that is known as drag amplification. The drag coefficient amplification factor can be measured or determined and can double or triple the normal drag coefficient.
An empirical relation to describe the drag force amplification has been described by (Blevins, 2001). The amplification factor is determined based on a dimensionless parameter A/D, the cross-flow vibration amplitude over riser diameter.
(De Wilde and Huijsmans, 2004) corrects for the drag amplification by relating the drag coefficient to the speed at which the cylinder moves through the water. The Reynolds numbers from this experiment are in the subcritical regime, the same as the VTS riser sections. From this experiment it is seen that the drag coefficient decreases when the towing speed increases. The experienced drag with VIV can be up to three times higher than the drag experienced without VIV, which implies that the drag force and the resulting motions are much more extreme when VIVis included. Since VIV is a non-linear effect that is known to severely increase required computational power it is not taken into account in the approximate model.

2-2-11 Booster stations

All booster stations will be equipped with two pumping stations. If the booster stations are well designed the two pumping stations will be able to counteract each others torque. The booster stations can also counteract the force that is created by the change of direction of the slurry, so only a moment will remain as an added force. It is assumed that this moment is negligible.

2-2-12 Slurry transport

Transporting a slurry existing from seawater, nodules and sediment to the MSV is what the VTS is designed to do. The density of the slurry varies over time depending on the amount and size of nodules present at the sea floor and the speed of the SMT. On average the density of the slurry is $1200 kg/m^3$, which is larger than the average density of seawater. Since variation in density of the slurry are expected to occur slow (van Dort, 2016) it is assumed these variations have little effect on the mass of the riser. Therefore the density of the slurry is assumed constant and set at $1200 kg/m^3$.

2-2-13 Marine Growth

Over time marine growth will appear on and influence the behaviour of the riser. Marine growth is the growth of marine lifeforms on the VTS such as algeas and clams, which causes an increase in riser diameter and an increased surface roughness. The process of marine growth is a very slow process and it is assumed that the growth of marine life does not occur in the relatively short period that the system is simulated. If in the future the real world deep sea mining system is operational and operating for days or weeks in a row the model will need some mitigation strategies (for example increasing the drag coefficient C_d over time) to account for this effect.

2-2-14 Finite element method

The riser sections are modelled numerically, which means the analytical equations have to be spatially discretized. For the modelling method two techniques have been considered, either the finite element method or the finite difference method can be used. In literature a lot is written abut both the finite difference and the finite element methods. The finite element method is more appropriate in this problem because of its greater geometric flexibility and easier error analysis (Thomée, 2001).

2-3 Vertical transport system parameters

In this section all the parameters used to build the approximate model are described. The data was provided by Royal IHC, unless specified otherwise.

2-3-1 Riser sections

The riser can be divided into six main sections, where each section begins and ends at a booster station. All sections are numbered as in figure 2-5. Over the entire riser the inner diameter remains constant, but the wall thickness and thus the outer diameter of the riser varies per section.

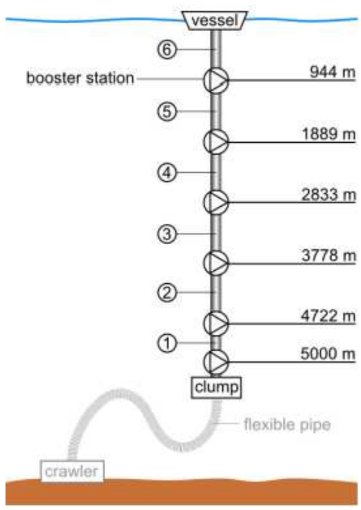

Figure 2-5: Riser sections

Per section the wall thickness remains constant and the wall thickness's of the last two sections are equal. In table 2-4 the different outside diameters of the riser sections are found. Booster stations along the length of the riser are configured differently than regular riser sections, how this is done is described in 2-3-2.

Section	**Length** $[m]$	**Wall thickness** $[mm]$	**Outer diameter** $[m]$
Section 6	944	35	455.6
Section 5	944	25.4	436.4
Section 4	944	19.1	423.8
Section 3	944	13.5	412.6
Section 2	944	12.7	411.0
Section 1	278	12.7	411.0

Table 2-4: Riser section lengths

A lot is already known from the riser, this is common data like the density of the riser material and the Young's modulus of steel. All of the sections make use of the same type of steel of which the properties are found in table 2-5.

Parameter	**Value**	**Unit**
Riser inner diameter	356	mm
Density of steel	7800	kg/m^3
Slurry density	1200	kg/m^3
Total riser length	5000	m
Young's Modulus of steel	$200 \cdot 10^9$	Pa

Table 2-5: Riser parameters

2-3-2 Booster stations

Along the length of the riser there are several pumping sections, called booster stations. Each booster station contains a pair of pumps which transport the slurry harvested from the seabed to the ship. A booster station section has a mass of $15 \cdot 10^3 kg$ and an increased diameter, which like the length of each booster station can be found in table 2-6.

Section	**Length** $[m]$	**Wall thickness** $[mm]$	**Outer diameter** $[m]$
Booster station	21.2	12.7	2.3

Table 2-6: Riser section lengths

The mass of the booster stations can be calculated, or measured by simply weighing the booster station section on hang-off. Stiffness of the booster station is harder to determine, but in time when they will have to be build this can be researched. It is assumed that the stiffness of a booster station station section is equal to five times the stiffness of a regular riser section of equal length.
The booster stations are equipped electric pumps so they receive power from the top of the ship through an umbilical. This umbilical adds mass to the system and also increases the drag force. Not much information on the umbilical is available yet. In riser simulations created by

VIVID it is assumed that the umbilical adds a weight of five percent of the total riser weight per meter to the riser. It is also assumed that the umbilical does not increase the drag force in the system. The same assumptions about the umbilical are used in this thesis.
The infrastructure advantage makes the booster station an attractive place to put the measurement equipment. At the top and at the bottom of each booster station measurement equipment will be added.

2-4 The Kalman filter

The system consists of a structural dynamics model of the VTS which is combined with data gathered from measurement points along the riser. A model can be used to simulate the behaviour of a system by using the laws of physics. Even though the laws of physics have been formulated many years ago, a model still is an approximation of the real world system. (Heemink, 1991) While creating a model many things are estimated or simplified, which creates uncertainty in the model.
The KF is a way to combine measurement data with data from the model, by using the uncertainty in the data from both. The system is described by a difference equation 2-12. In this equation $\mathbf{A}_d$ is the discrete prediction matrix which is used to calculate the new system state and $\mathbf{B}_d$ is the discrete external influence matrix. z_k are the measurements done by the sensors along the VTS. Because these measurements will be contaminated with noise, a stochastic white noise process w_k is added to the observer states y_k. Equation 2-13 can be used to model the observer, where $\mathbf{H}$ is the matrix that relates the state to the measurement.(Bishop and Welch, 2001)

$$x_k = \mathbf{A}_d \, x_{k-1} + \mathbf{B}_d \, u_{k-1} + v_k \tag{2-12}$$

$$y_k = \mathbf{H} x_k + \mathbf{D} \, u_k + w_k \tag{2-13}$$

In these equations v_k and w_k are the process and measurement noise respectively. z_k are the measurements created by the system. The process noise is added to the inputs of the approximate model to create an unknown effect in the original model, because unlike in the real world for this system the model used to create measurements would be perfectly the same as the model used to create state estimations later on. Both the process noise and measurement noise are assumed to be Gaussian white noise processes (Bishop and Welch, 2001).

$$E\{v_k\} = 0, E\{w_k\} = 0 \tag{2-14}$$

In the equation above $E\{v_k\}$ is the expected value of process noise v_k, the same goes for measurement noise w_k. Of these process noises the covariance matrices are determined where the process noise covariance matrix is defined as Q and the measurement covariance matrix is defined by R. The covariance matrix is a diagonal matrix with on its diagonal the variance of every sensor, which is equal to the squared standard deviation.
Now the KF equations can be divided into two parts, an a-priori and an a-posteriori step. $\hat{x}_k^-$ is defined as the a-priori state estimate and $\hat{x}_k$ the a-posteriori state estimate at time step k. As a first the a-priori states and a-priori error covariance are determined in equation 2-15 and equation 2-16.

$$\hat{x}_{k+1}^{-} = \mathbf{A}_d\,\hat{x}_k + \mathbf{B}_d\,\hat{u}_k \tag{2-15}$$

$$P_k^{-} = \mathbf{A}_d\,P_{k-1}\,\mathbf{A}_d^T + Q \tag{2-16}$$

These equations make up the time prediction equations. How the initial error covariance is obtained is explained later, at equation 2-22. Using the a-priori estimates of the states of the system and the a-priori error covariance matrix the measurements can be introduced. In the three following equations the measurements are combined with the state estimations in the measurement update function. First the Kalman gain, K_k, is calculated

$$K_k = \frac{P_k^{-}\mathbf{H}^T}{HP_k^{-}\mathbf{H}^T + R} \tag{2-17}$$

The Kalman gain gives a weight to the measurements and the model estimations. When a high gain is determined more weight is given to the measurement, a low gain gives more weight to the model estimations. Using the gain, the estimations and the measurement the updated states and updates error covariance are determined.

$$\hat{x}_k = \hat{x}_k^{-} + K_k\left(z_k - \mathbf{H}\hat{x}_k^{-}\right) \tag{2-18}$$

$$P_k = (I - K_k\mathbf{H})\,P_k^{-} \tag{2-19}$$

These states and error covariance are the final outputs and are used to calculate the next estimation. The full scheme for the equations is seen in figure 2-6.

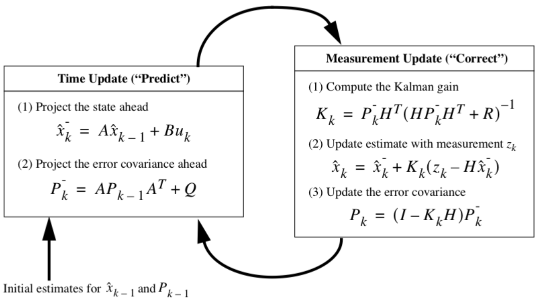

Figure 2-6: Kalman Filter block scheme. Source: (Bishop and Welch, 2001)

The error covariance and the Kalman gain go to a steady state when a linear filter without varying covariance matrices is used. Residuals are calculated as the error between the actual states of the system and the estimated states of the system.

$$e_k^{-} \equiv x_k - \hat{x}_k^{-} \tag{2-20}$$

$$e_k \equiv x_k - \hat{x}_k \tag{2-21}$$

The error covariance results from the error between the states estimated by the model and the actual system states. The a-priori error covariance is calculated as follows

$$P_k^- = E\{e_k^- e_k^{-T}\} \tag{2-22}$$

2-5 VIVID

In this section a short description on VIVID is provided. VIVID is a riser design tool, developed inhouse by Royal IHC, that is used to generate simulations that serve as measurement data to the KF. After the approximate model is build the model is compared to simulation data created by VIVID, this is done in section 3-4. This section is meant to compare and highlight the differences between the approximate model and VIVID, so differences in performance can be explained later on.

2-5-1 Finite element model

Just like the approximate model VIVID uses a finite element method to create a model of the riser. Each section of the riser and each booster station is build up using Euler-Bernoulli beam elements. A section of around 940 meters is build from 29 elements, a booster station element with a length of 21.2 meters is build using 11 elements. All of the parameters, like inner and outer diameters, material density and stiffness are the same in VIVID as well as in the approximate model.
Contrary to the approximate model VIVID generates three dimensional motions. Also VIVID is able to account for elongation, torsion and VIV.

2-5-2 Vortex induced vibrations

VIVID is able to include the effect of extra vibrations introduced by VIV. VIV is a non linear effect that created vibrations in the riser, perpendicular to the flow that excites the riser. These vibrations can result in an increased in-line drag force, described in 2-2-10. In VIVID the effect of VIV is introduced using a wake oscillator model. For the full implementation of this effect the reader is referred to the paper from (Ogink and Metrikine, 2010).

2-5-3 Effective tension

For the axial wall tension in the riser VIVID makes use of the effective tension. The effective tension in a section is different from the true tension, which is a sum of the axial forces in the riser and the slurry. Effective tension also takes the pressures inside the riser into account and is calculated as the sum of the axial forces in the riser wall and content minus the axial force in the displaced slurry. A more detailed description, including some examples is found in (Sparks, 2012). VIVID also takes the pressure increase at the booster stations and the pressure decrease with increasing height of the riser into account. These effects are all neglected in the approximate model.

2-5-4 Ordinary differential equation solver

For solving the Ordinary Differential Equation (ODE)s that make up the full system after assembly a generalized alpha ODE solver scheme is used. The generalized alpha scheme is a second-order implicit scheme, like the Newmark-beta method used to solve the ODEs for the approximate model. For a more extensive read the derivation of the method is found in books and papers, like (Erlicher et al., 2002).

2-6 Conclusion

Due to the large depth at which the system is operational and the large area in which it operates acoustical measurement techniques will not be used. Accelerometers, angle sensors and water velocity are measured at the booster stations. The approximate model is built using Euler-Bernouilli beams since it can be classified as a slender beam. To save on computational power VIV is not included in the approximate model. The riser is modelled as a two dimensional object. This can be done because none of the effects that are used in the approximate model create motions in more than two dimensions when two dimensional inputs are used.

Chapter 3

Approximate model

In this chapter the equations that make up the approximate model are derived. First a model is created using discrete Euler-Bernouilli beams. This approach is then verified by comparing the results to analytically obtained results and the sensitivity of the approximate model to a variations in time step and element size are checked. Finally the simulations generated by the approximate model and VIVID are compared.

3-1 Beam finite element model

In this section the mass and stiffness matrix are determined. The model of the Euler-Bernoulli beam is discretized so it can be solved numerically. An added advantage to this is that element lengths can be varied and booster stations and clump weight sections are easily added.

3-1-1 Discrete beam matrices

The equation of a transverse vibrating linear beam has to be discretized in time and space so it can be solved numerically. The finite element derivation of the beam is the base of the model of the free-hanging riser. In order to be able to model the behaviour of the beam the infinite dimensional partial differential equation derived in section 2-2-3 is split into segments. Creating a Finite Element Method (FEM) model is a way to approximate the solution of the beam motions by assuming a solution in the form of a polynomial. The full description of the FEM equations has been derived before, for instance in (Lienemann et al., 2004; Irvine, 2008, 2003), a description is given in this chapter.

Material stiffness

Each beam element has two nodes which can displace in the x and the z directions. These motions are given by $w(x, z)$ and $v(x, z)$ which are the motions of the beam in x direction

and z direction respectively. For the motion in the x direction assumption is made that it only depends on the x coordinate, so $w(x,z) = w(z)$. The motions in v directions are written as $v(x,z) = -x\frac{\delta w(z)}{\delta z} = -x\theta$ where $w' = \theta$.
Setting up the FEM is started by determining the energy of an element with length dL using the Lagrangian formulation, $\mathbb{L} = \mathbb{T} - \mathbb{V}$. By using the Euler-Bernoulli theory the potential energy $\mathbb{V}$ comes from bending and axial stresses. The potential energy is found as

$$\mathbb{V} = \frac{1}{2}\int_V \sigma_{zz} e_{zz} dV \tag{3-1}$$

In this equation ϵ_{zz} is the axial strain in the z-direction and σ_{zz} the stress from bending. Both of these can be written such that they can be related to motions of the beam, for the axial strain

$$\epsilon_{zz} = \frac{\delta v}{\delta z} = -x\frac{\delta^2 w}{\delta z^2} = -xw'' \tag{3-2}$$

and

$$\sigma_{xx} = E\epsilon_{zz} = -Ex\frac{d^2 w}{dz^2} = -Exw'' \tag{3-3}$$

The term w'' represents the curvature of the beam and is written as $k \approx w''$. As a final a bending moment M is defined.

$$M = \int_A -x\sigma\, dz = E\,\frac{d^2 w}{dz^2}\int_A x^2\, dA = E\, I_{yy}\, k \tag{3-4}$$

In this equation I_{zz} is the inertia with respect to the bending axis, in this case the y axis. Using these equations the internal energy of the beam can be expressed as a combination of beam motions, this is done in equation 3-5.

$$\mathbb{V} = \frac{1}{2}\int_V \sigma_{zz}\epsilon_{zz} dV = \frac{1}{2}\int_0^L M\, k\, dz = \frac{1}{2}\int_0^L E\, I\, k^2 dz = \frac{1}{2}\int_0^L w''\, E\, I\, w'' dz \tag{3-5}$$

So now the beam motions over the beam length have to be determined. Determining the beam motions is done by interpolating over the beam using the Hermitian cubic shape functions. These functions relate the deflection of the beam to a dimensionless point ξ on the beam. This point ξ is determined as $\xi = \frac{2z}{dL} - 1$. The coordinate varies from $\xi = -1$ to $\xi = 1$ which is at $x = 0$ and $x = dL$ respectively. Each node has two Degrees Of Freedom (DOFs), the deflection w and the rotation θ. The hermitian cubic shape functions relate the deflection of a point on the beam to the deflections and rotations at the nodes as follows

$$\bar{w} = \begin{bmatrix} N_{w_1} & N_{\theta_1} & N_{w_2} & N_{\theta_2} \end{bmatrix} \begin{bmatrix} w_1 \\ \theta_1 \\ w_2 \\ \theta_2 \end{bmatrix} = \mathbf{N}\,\bar{v} \tag{3-6}$$

The hermite shape functions for a beam element with length dLexpressed in general coordinates ξ are

$$N_{w_1} = \frac{1}{4}(1-\xi)^2(2+\xi) \tag{3-7}$$

$$N_{\theta_1} = \frac{1}{8}dL(1-\xi)^2(1+\xi) \tag{3-8}$$

$$N_{w_2} = \frac{1}{4}(1-\xi)^2(2-\xi) \tag{3-9}$$

$$N_{\theta_2} = -\frac{1}{8}(1-\xi)^2(1-\xi) \tag{3-10}$$

Which in terms of curvature results in

$$\frac{d^2\bar{w}}{dz^2} = \frac{d^2\mathbf{N}}{dz^2}\,\bar{v} \tag{3-11}$$

Now the potential energy for a full beam element is derived.

$$\mathbb{V} = \frac{1}{2}\bar{v}^T\mathbf{K}_m\bar{v} \tag{3-12}$$

From this equation, and by combining 3-5 and 3-11 the stiffness matrix $\mathbf{K}_m$ for an element with length dL is obtained.

$$\mathbf{K}_m = \int_0^l \mathbf{N}''^T\, E\, I\, \mathbf{N}'' dz = \frac{1}{2}\, E\, I\, dL \int_{-1}^{1} \mathbf{N}''^T\mathbf{N}'' d\xi \tag{3-13}$$

When all the term for $\mathbf{N}''$ are derived and integrated the matrix coordinates are written in terms of z coordinates again. Combining results in the following stiffness matrix for a beam element.

$$\mathbf{K}_m = \frac{EI}{dL^3}\begin{bmatrix} 12 & 6dL & -12 & 6dL \\ 6h & 4dL^2 & -6dL & 2dL^2 \\ -12 & -6dL & 12 & -6dL \\ 6dL & 2dL^2 & -6dL & 4dL^2 \end{bmatrix} \tag{3-14}$$

3-1-2 Inertia

Next the inertia matrix, also referred to as mass matrix, is derived by determining the kinetic energy of the system. The full kinetic energy of the system $\mathbb{T}$ is given by the following equation.

$$\mathbb{T} = \frac{1}{2}\int_V \rho\dot{\bar{w}}^T\,\dot{\bar{w}}dV \tag{3-15}$$

By using the same cubic hermite shape functions as used to determine the stiffness matrix the velocity $\dot{\bar{w}}$ is written in terms of nodal displacements as

$$\dot{\bar{w}}'' = \mathbf{N}''\,\dot{\bar{v}} \tag{3-16}$$

It is assumed that the mass is consistent over the entire length of the element. The mass matrix $\mathbf{M}$ is rewritten in terms of the hermite shape functions. When equations 3-15 and 3-16 are combined the following equation for the kinetic energy is found

$$\mathbb{T} = \frac{1}{2}\,\dot{\bar{v}}^T \int_V \rho\mathbf{N}^T\,\mathbf{N}\,dV\,\dot{\bar{v}} = \frac{1}{2}\,\dot{\bar{v}}^T\,\mathbf{M}\,\dot{\bar{v}} \tag{3-17}$$

So that

$$\mathbf{M} = \int_V \rho\, \mathbf{N}^T\, \mathbf{N}\, dV = \int_0^l \rho\, A\, \mathbf{N}^T\, \mathbf{N}\, dz \tag{3-18}$$

When the hermite shape functions in this equation are integrated a consistent mass matrix $\mathbf{M}$ is derived as

$$\mathbf{M} = \frac{m_c}{420}\begin{bmatrix} 156 & 22dL & 54 & -13dL \\ 22dL & 4dL^2 & 13dL & -3dL^2 \\ 54 & 13dL & 156 & -22dL \\ -13dL & -3dL^2 & -22dL & 4dL^2 \end{bmatrix} \tag{3-19}$$

In this equation $m_c = \rho\, A\, dL$ is the mass of an element. For the full system this term is expanded to include terms for added mass, slurry transported by the system and mass added at booster stations and at the clump weight. So the full term m_c is found as

$$m_c = \rho_{st}\, A\, dL + m_a + \rho_{sl}\, A_{in}\, dL + m_b + m_{cl} \tag{3-20}$$

Where m_b is the added mass of a booster station over the element length and m_{cl} is the added mass of the clump weight over an element length. When the element that in question is not a booster station or the clump weight these terms are equal to zero for that element.

Geometrical stiffness

Adding a tension term to the discrete beam is done in the same way as the stiffness and the inertia matrix are determined, by looking at its potential energy. The tension force in the system is fully created by the mass of the system, so at the bottom side of the clump weight the tension force is equal to zero. Over each element the tension force is assumed constant. In order to implement the tension force T the resulting strain from the force is expressed in terms of displacement as follows. Assume a compressive force works on the ends of the beam. This force creates a deflection in the z direction, dv. Because the beam is compressed it also deflects to the side a, so it deflects in the direction of the x axis with a deflection of dw. The strain equations for deflections, only taking into account the x-direction for deflection is

$$\epsilon_{zz} = dv + \frac{1}{2}\left(\frac{dw}{dz}\right)^2 \tag{3-21}$$

This deflection in the x-direction is assumed to be the main contribution to the total axial strain ϵ_{zz}, so $dv = 0$. Now the potential energy introduced by the tension force is found as

$$\mathbb{V} = \int_0^d LT\, \epsilon_{zz}\, dz = \frac{1}{2}\, T \int_0^d L\left(\frac{dw}{dz}\right)^2\, dz \tag{3-22}$$

The potential energy can be rewritten to include the hermite cubic shape functions. The hermite shape function are introduced by

$$\frac{d\bar{w}}{dz} = \mathbf{N}'\, \bar{v} \tag{3-23}$$

By combining equations 3-22 and 3-23 the expression for the internal energy becomes

$$\mathbb{V} = \frac{1}{2}\, T\, \bar{v} \int_0^d L\mathbf{N}'^T\, \mathbf{N}'\, dz\bar{v} \tag{3-24}$$

From this equation the geometric stiffness matrix $\mathbf{K}_p$ is derived as

$$\mathbf{K}_p = T \int_0^d L \mathbf{N}'^T \mathbf{N}' \, dz \tag{3-25}$$

When the cubic hermite shape functions are differentiated the equation is written in full matrix form as

$$\mathbf{K}_p = \frac{T}{30dL} \begin{bmatrix} 36 & 3dL & -36 & 3dL \\ 3dL & 4dL^2 & -3dL & -dL^2 \\ -36 & -3dL & 36 & -3dL \\ 3dL & -dL^2 & -3dL & 4dL^2 \end{bmatrix} \tag{3-26}$$

The material stiffness matrix and the geometrical stiffness matrix are combined as $\mathbf{K} = \mathbf{K}_m + \mathbf{K}_p$

3-1-3 Damping matrix

The damping matrix is constructed from two different principles. At first there is material damping in the system which can be modelled using Rayleigh damping. Next to this the seawater surrounding the riser will create viscous damping.

Material damping

The internal structural damping in the system is modelled using a method known as Rayleigh damping. The matrix is modelled as a combination of the mass and stiffness matrix as in equation 3-27.

$$[\mathbf{C}] = \alpha_d \, [\mathbf{K}] + \beta_d \, [\mathbf{M}] \tag{3-27}$$

The damping ratio takes the form of

$$\zeta = \frac{\alpha_d}{2 * \omega_i} + \frac{\beta_d \, \omega_i}{2} \tag{3-28}$$

For ζ the following values are used, $\zeta_1 = \zeta_2 = 0.002$ (Bachmann et al., 1995). The values for α_d and β_d are found by solving the equations

$$\alpha_d = \frac{2 * \omega_1 \, \omega_2 (\zeta_1 \, \omega_2 - \zeta_2 \, \omega_1)}{\omega_2^2 - \omega_1^2} \tag{3-29}$$

$$\beta_d = \frac{2 * (\zeta_2 \, \omega_2 - \zeta_1 \, \omega_1)}{\omega_2^2 - \omega_1^2} \tag{3-30}$$

For ω_1 and ω_2 the first and second natural frequency of the system are used.

Viscous damping

Because the riser is submerged it experiences a lot of drag. The drag force can be calculated using equation 2-10 which is the Morison equation for a body moving through water. All of the velocities are relative to the velocity of the ship, so $(u_{cu} - \dot{w}) \, |u_{cu} - \dot{w}|$ is the squared relative velocity of the water compared to the ship velocity. The part of the drag force that is considered as viscous damping is the part directly related to the speed of the riser relative to the ship, $\dot{w}$.

3-1-4 External force matrix

The external forcing matrix $F(t)$ is build up from several (in)dependent forces that act on the system. These forces have been combined and form the final building block of the FEM model.

Drag force

The drag force is calculated by the Morison equation explained in subsection 2-2-8. In order to implement the drag force in the matrices of the system the drag force is calculated per meter, which is done by equation 3-31. This is the same equation as the Morison equation described before, but without the inertia terms.

$$F_{drag} = \frac{1}{2}\rho C_d D_{out}(u-v)|u-v| \tag{3-31}$$

The drag force per meter is added to the matrix system as a point force on every node. The point force at a node is calculated as

Force from boundary conditions

The imposed movement boundary condition described in subsection 2-2-4 is implemented as one of the external forces. While the other three boundary conditions allow free movement which doesn't affect the way the FEM model is build, the imposed movement means adjustments have to be made.
A vector x_w is introduced which is the combination of the deflections in the x direction and the rotation such that $x_{w_i} = \begin{bmatrix} w_i \\ \theta_i \end{bmatrix}$ at a specified node i. The system from equation 3-36 can be written as a system with free DOFs x_w and non-free DOFs $x_{\bar{w}}$. Non-free, or imposed DOFs are the ship relative displacement $x_{\bar{w}}$, velocity $\dot{x}_{\bar{w}}$ and acceleration $\ddot{x}_{\bar{w}}$. Using this the following equation can be derived

$$\begin{bmatrix} \mathbf{M}_{\bar{w}\bar{w}} & \mathbf{M}_{\bar{w}w} \\ \mathbf{M}_{w\bar{w}} & \mathbf{M}_{ww} \end{bmatrix} \begin{bmatrix} \ddot{x}_{\bar{w}} \\ \ddot{x}_w \end{bmatrix} + \begin{bmatrix} \mathbf{C}_{\bar{w}\bar{w}} & \mathbf{C}_{\bar{w}w} \\ \mathbf{C}_{w\bar{w}} & \mathbf{C}_{ww} \end{bmatrix} \begin{bmatrix} \dot{x}_{\bar{w}} \\ \dot{x}_w \end{bmatrix} + \begin{bmatrix} \mathbf{K}_{\bar{w}\bar{w}} & \mathbf{K}_{\bar{w}w} \\ \mathbf{K}_{w\bar{w}} & \mathbf{K}_{ww} \end{bmatrix} \begin{bmatrix} x_{\bar{w}} \\ x_w \end{bmatrix} = \begin{bmatrix} R(t) \\ F(t) \end{bmatrix} \tag{3-32}$$

In which $\mathbf{M}_{\bar{w}\bar{w}}$ is a constant, $\mathbf{M}_{\bar{w}w}$ and $\mathbf{M}_{w\bar{w}}$ are vectors of size $1 \times n-1$ and $n-1 \times 1$ respectively, where n is the amount of DOFs. Following from this $\mathbf{M}_{uu}$ is a matrix with dimensions $n-1 \times n-1$. The same sizes go for $\mathbf{C}$ and $\mathbf{K}$. In the equation $R(t)$ is the reaction that works horizontally at the top of the riser and $F(t)$ is the distributed force introduced by the relative velocity between the current and the riser along the riser. The system is rewritten so that the reaction forces is excluded.

$$\begin{bmatrix} \mathbf{M}_{w\bar{w}} & \mathbf{M}_{ww} \end{bmatrix} \begin{bmatrix} \ddot{x}_{\bar{w}} \\ \ddot{x}_w \end{bmatrix} + \begin{bmatrix} \mathbf{C}_{w\bar{u}} & \mathbf{C}_{ww} \end{bmatrix} \begin{bmatrix} \dot{x}_{\bar{w}} \\ \dot{x}_w \end{bmatrix} + \begin{bmatrix} \mathbf{K}_{u\bar{w}} & \mathbf{K}_{ww} \end{bmatrix} \begin{bmatrix} x_{\bar{w}} \\ x_w \end{bmatrix} = F(t) \tag{3-33}$$

This system can be divided into at the left hand side the resulting equations of motions and at the right hand side the input forces from relative current and imposed motions.

$$\mathbf{M}_{ww}\ddot{x}_w + \mathbf{C}_{ww}\dot{x}_w + \mathbf{K}_{ww}x_w = F(t) - \mathbf{M}_{w\bar{w}}\ddot{x}_{\bar{w}} - \mathbf{C}_{w\bar{w}}\dot{x}_{\bar{w}} - \mathbf{K}_{w\bar{w}}x_{\bar{w}} \tag{3-34}$$

In order to solve the equation of motion the entire system is divided by $\mathbf{M}_{ww}$.

Combined

The drag force and the force from the boundary condition form the following term in which $F(t)$ is the non-linear drag force.

$$F_{tot} = F(t)/\mathbf{M}_{ww} - \begin{bmatrix} \mathbf{M}_{w\bar{w}}/\mathbf{M}_{ww} & \mathbf{C}_{w\bar{w}}/\mathbf{M}_{ww} & \mathbf{K}_{w\bar{w}}/\mathbf{M}_{ww} \end{bmatrix} \begin{bmatrix} \ddot{x}_{\bar{w}} \\ \dot{x}_{\bar{w}} \\ x_{\bar{w}} \end{bmatrix} \tag{3-35}$$

3-1-5 Matrix assembly

Combined the system equation of motion can be written as

$$\mathbf{M}\ddot{x}(t) + \mathbf{C}\dot{x}(t) + (\mathbf{K_m} + \mathbf{K_p})\, x(t) = F_{tot}(t) \tag{3-36}$$

3-2 Verification

The model now has to be verified. This is done by comparing steady-state solutions and the natural frequencies of various configurations of the FEM model to analytical solutions and an experimental setup.

3-2-1 Static

To verify the static behaviour of the FEM model two cases have been researched. Case one is a model of a beam, clamped at the left end free-hanging at the right, case two is a beam hinged at both ends with a varying distributed load. Both of the cases can be solved with equations found in standard mechanics textbooks like (Hibbeler, 2011), which was used in order to solve these two cases. Because solving beam equations like the two following cases is common in mechanical engineering, only the final equations and the beam characteristics are given. The background of the equations used can be found in (Hibbeler, 2011).
In both of the cases the solution for the FEM model has been found by running the model with the case specific constraints and loads. The simulation is said to have reached a steady-state when the deflection at the point where maximum deflection occurs varies with less than $1 \cdot 10^{-10}m$ per time step of $0.02s$. This size of time step is chosen based on the first natural frequencies of the systems, $0.56Hz$ for the clamped-free beam and $1.17Hz$ for the hinged-hinged beam. The chosen sampling frequency of $50Hz$ is higher than the first natural frequencies of the system, which accompanies the deflection shape of interest.

Clamped-free beam with point load

The first case consists of a hollow cylinder build up from two sections, both with the same internal diameter, but with a different external diameter. At the tip of the cylinder there is a force working downwards. A drawing of the deflected cylinder can be seen in figure 3-1. Characteristics of the cylinder can be found in table 3-1.

Parameter	**Value**	**Unit**
Cylinder outer diameter A	0.39	m
Cylinder outer diameter B	0.37	m
Cylinder inner diameter	0.35	m
Cylinder length section A	15	m
Cylinder length section B	15	m
Young's Modulus of steel	$200e9$	Pa
Density of steel	7850	kg/m^3
Constant tip force	$10e3$	N

Table 3-1: Clamped-free cylinder and load characteristics

The deflection of a clamped-free cylinder with a point-load at the tip, where the deflection is largest, is given by equation 3-37.

$$w_{max} = \frac{F_{tip}}{3EI_A} * \left\langle \left(1 - \frac{I_A}{I_B}\right) * l^3 - L^3 \right\rangle \tag{3-37}$$

In equation 3-37 the point along the cylinder where the outer diameter changes is given by l, which is equal to the length of cylinder section A. The total length of the cylinder is given by L. I_A is the inertia of the left part of the cylinder, blue in figure 3-1, I_B is the inertia of the right part of the cylinder, red in figure 3-1. The inertia is calculated by equation 3-38.

$$I = \frac{\pi}{64} * \left(D_o^4 - D_{in}^4\right) \tag{3-38}$$

When the values from table 3-1 are used in equation 3-37 a tip deflection of $1.256m$ is found, which is equal to the steady-state deflection of the tip of the FEM model.

Hinged-hinged beam with distributed load

The second case consists of a hinged-hinged hollow cylinder. The cylinder has a uniform inner and outer diameter, mass and inertia. It is loaded by a distributed load, which is constant over the length of the beam and is equal to the load of a current flowing at $0.5m/s$. Current force is calculated by the Morison equation explained in subsection 2-2-8. Characteristics of the cylinder and the distributed load can be found in table 3-2.

Just like in the previous case the equation for the maximum deflection of a hinged-hinged beam can be easily found in textbooks like (Hibbeler, 2011). Therefore only the formula for the maximum deflection of the beam is explained. The maximum deflection of the cylinder is given by equation 3-39.

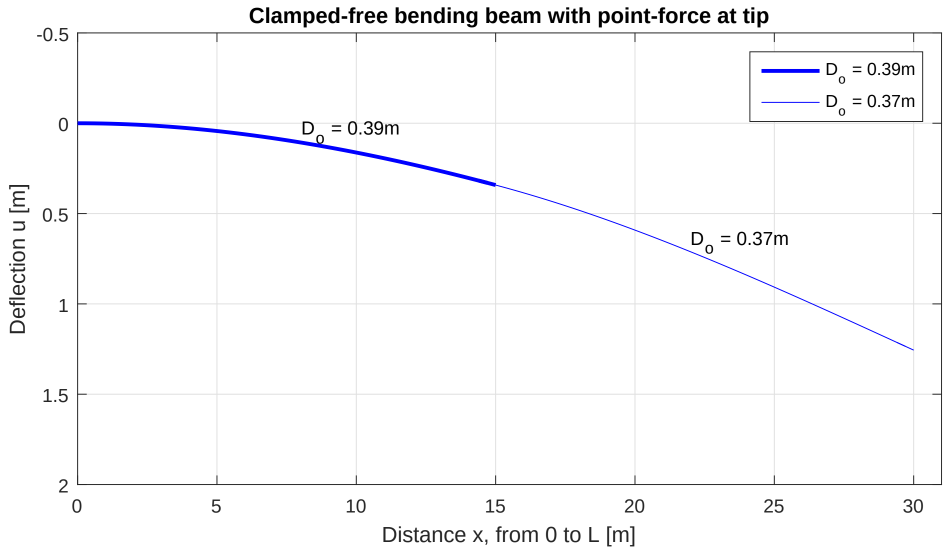

Figure 3-1: Clamped-free Euler-Bernoulli beam

Parameter	Value	Unit
Cylinder outer diameter	0.39	m
Cylinder inner diameter	0.35	m
Cylinder length	30	m
Young's Modulus of steel	$200e9$	Pa
Density of steel	7850	kg/m^3
Distributed load	119.93	N/m

Table 3-2: Hinged-hinged cylinder and load characteristics

$$u_{max} = \frac{5 * F_{distrb} * L^4}{384 * E * I} \tag{3-39}$$

In this equation F_{distrb} is the distributed load, L the total cylinder length, E the young's modulus of steel and I the inertia as calculated by 3-38. When the FEM model has reached a steady state its deflection is plotted as figure 3-2. At the center of the cylinder is the largest deflection occurs, which is calculated to be $0.015m$ by the FEM model. The analytical solution, equation 3-39, leads to the same result.

3-2-2 Dynamic

Next to the static solutions also the dynamics of the system have to be checked. This has been done partially by the static analysis in the previous subsection, where the FEM model reached a steady-state equal to the analytical solutions. To expand the verification the natural frequencies of the system are checked for two cases.

For the first case the natural frequencies of a clamped-free beam are extracted from the FEM model and compared to an analytical solution. The results are found in appendix B. In the second case the natural frequencies of a tensioned hinged-free beam are compared to

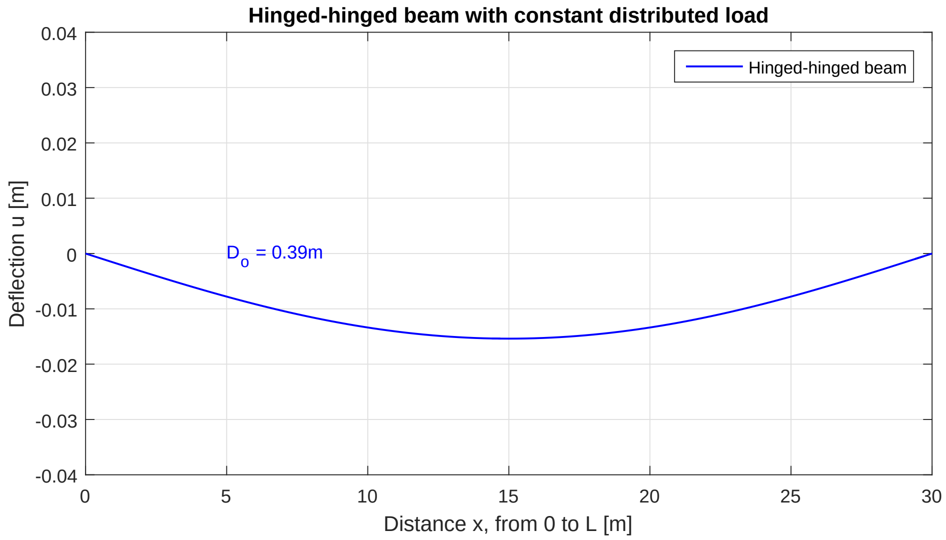

Figure 3-2: Hinged-hinged Euler-Bernoulli beam

an analytical solution. The analytical solution from the second case has been validated by experiments which found in (Currie and Cleghorn, 1988).

Natural frequencies of a clamped-clamped tensioned beam with concentrated mass

In this last case the FEM model will be compared to a study done by (Currie and Cleghorn, 1988). In this paper a beam that is clamped at both ends is exited in order to measure its first natural frequency. At the center of the beam there is a concentrated mass. The first natural frequency was calculated analytically. It is interesting to compare the FEM model to this case, because its calculated results have been validated by experiments.
To calculate the first natural frequency the symmetry of the beam has been used. This way a beam can be modelled that is half the length of the beam of the experiment and is clamped at one end and free at the other end. At the free end of the beam is the concentrated mass. The full derivation of the analytical solution can be found in (Currie and Cleghorn, 1988). Calculating the natural frequencies of the tensioned beam is quite comparable to those of the non-tensioned beam from the previous case. The tensioned beam has been used, the same as equation 2-8, in which the distributed load $q(z,t)$ was set to zero. At the clamped left-hand side the boundary conditions from equation B-2 applies. The boundary equation at the right hand side, at $z = L$, with the concentrated mass is given by equations 3-40 and 3-41.

$$\left.\frac{dw}{dz}\right|_{z=L} = 0 \tag{3-40}$$

$$2\,EI\left.\frac{d^3w}{dz^3}\right|_{z=L} + M\omega^2 z(L) = 0 \tag{3-41}$$

In this equation M is the non-dimensionalized mass variable. The general solution (Currie and Cleghorn, 1988) can now be written as

$$W(z) = A\,\sinh(\alpha\,z) + B\,\cosh(\alpha\,z) + C\,\sin(\beta\,z) + D\,\cos(\beta\,z) \tag{3-42}$$

And α and β are solved to be

$$\alpha = \sqrt{\sqrt{T^2 + {\omega_d}^2} + T} \tag{3-43}$$

$$\beta = \sqrt{\sqrt{T^2 + {\omega_d}^2} - T} \tag{3-44}$$

In these equations T and ω are the non-dimensionalized tension and frequency terms. Using the general solution 3-42 and the boundary conditions B-2 and 3-40, B, C and D can be calculated. When B, C and D are then substituted into boundary equation 3-41 the following equation can be found.

$$\begin{aligned}&\left(\alpha^2 + \beta^2\right)\alpha\,\beta\,\left(\alpha\,\sinh(\alpha)\cos(\beta) + \beta\,\cosh(\alpha)\sin(\beta)\right)\\&\quad - M{\omega_d}^2[2\,\alpha\,\beta\,(1 - \cos(\alpha)\cos(\beta)) + \left(\alpha^2 - \beta^2\right)\sinh(\alpha)\sin(\beta)] = 0\end{aligned} \tag{3-45}$$

Using equation 3-45 the system can be iteratively solved to find the dimensionless value for ω_d, which can then be used to find the natural frequencies of the system. Solving is done by guessing a value for ω_d, using this guess and the dimensionless tension new values for α and β can be calculated which can then be used in equation 3-45. When plotting this equation and a line at $y = 0$ is can be seen that there are an infinite amount of solutions, which means there are an infinite number of natural frequencies which is to be expected in a continuous system.

Figure 3-3: Visualisation of equation 3-45

Like in (Currie and Cleghorn, 1988) the FEM model has been build up as a clamped-clamped beam with a point mass in the center. This is the setup on which the analytical solution is based and of which the validity is proven in the paper.
Unlike in the paper, in this case multiple natural frequencies have been compared of one same system, where the first natural frequency is determined in multiple configurations. This has been done in order to check the validity of the model in higher modes.
When comparing this way it has to be kept in mind that extra modes will appear in the FEM model. From the modeshapes of the beam in figure 3-4 and figure 3-5 it can be seen that the first three modeshapes of the clamped-free beam take the same shape as modeshape one, three and five of the clamped-clamped beam. This is because in the FEM model the concentrated mass is able to rotate, which has been constrained in the analytical solution. While checking the results of this particular case this has to be kept in mind.

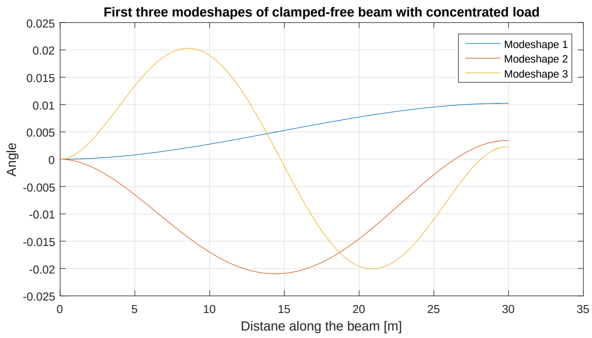

Figure 3-4: Modeshapes of a clamped-free beam with concentrated load

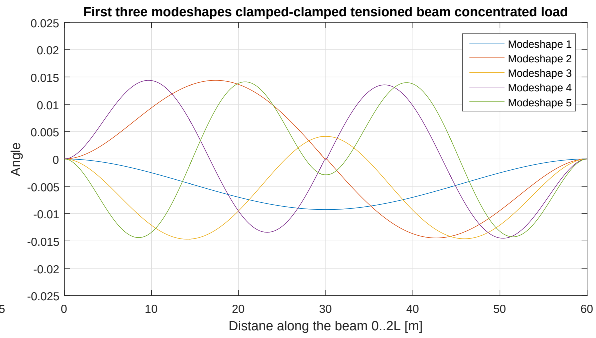

Figure 3-5: Modeshapes of a clamped-clamped beam with concentrated load

The natural frequencies of the FEM model for a tensioned beam can be calculated the same way as for the first case with the beam without tension, by calculating the determinant of equation B-17.
A comparison of the analytically derived natural frequencies and the natural frequencies derived from the FEM model can be found in table 3-3. In this particular case the same beam has been used as in the previous cases of which characteristics can be found in table 3-2, without the distributed load. A concentrated mass of $750kg$ and a constant tension of $73.6kN$ was used. The beam was split into elements with $3m$ length, except for the clump weight which was given a length of $0.1m$. As explained before in this section, only the uneven modes of the FEM model can be compared to the analytical solution.

From table B-1 it can be seen that, just like in the case of the clamped-free beam without a concentrated mass, the difference between the analytical model and the FEM model increases when the investigated mode increases. The difference stays relatively small and because the lowest modes contribute the most to the movements of the system the higher modes of the system are of less importance. It has to be kept in mind that simulating the full system becomes less accurate with increasing modes.

Mode	Analytic [ω]	Mode	FEM [ω]	Difference [%]
1	2.61	1	2.61	0.15
2	18.43	3	18.46	0.17
3	48.03	5	48.12	0.19
4	92.31	7	92.55	0.27
5	151.25	9	151.90	0.43
6	224.89	11	226.55	0.74
7	313.23	13	317.10	1.23

Table 3-3: Natural frequencies of a tensioned beam with concentrated mass solved both analytically and numerically

3-3 Approximate model sensitivities

After the approximate model setup is validated in the previous section, its sensitivity to different time steps and element sizes is checked.

3-3-1 Time step

As found in appendix A, a simulation frequency is suitable when it is higher than the highest natural frequency of interest. The low frequency natural frequencies of the Vertical Transport System (VTS) are of interest since these make up the large amplitude motions of the system. For the free-hanging riser it is now assumed that up to the sixth modeshape motions are created that add significantly to the total motions of the riser. The sixth modeshape is a modeshape with 5 nodes, and it is assumed that each booster station functions as a node. The sixth mode of the system has a natural frequency of $0.04Hz$ which allows for a large sampling time.
When determining a sampling time also the frequency of the input to the system should be determined. This can only be done by trial, since the input force is dependent on the velocity of the riser. In order to do this a sampling frequency of $100Hz$ is used. With the system sampled at $100Hz$ the output force is observed in the frequency domain by taking a fast fourier transform of the signal using the 'fft' function in Matlab. The largest exiting frequency introduced by the force lies at $1.2Hz$, so a sampling frequency larger than that should be used.
In table 3-4 the tip deflection after a simulation time of $3000s$ is shown. The duration of this simulation is chosen because at this point the system comes close to a steady-state, a state in which the tip of the system is at a standstill. A full standstill is not reached because the system is still exited by waves, but the average speed of the tip of the VTS is below $0.01m/s$. This state is not reached at exactly $3000s$ but a few hundred seconds before, the choice for $3000s$ is just the effect of rounding off the exact time to a later point in time.

It is seen that varying the sampling frequency has a negligible effect, therefore a sampling frequency of $20Hz$ is used throughout this thesis.

Sampling frequency	Maximum offset $[m]$
$10Hz$	122.4347
$20Hz$	124.4348
$50Hz$	122.4348

Table 3-4: Total tip deflection with varying time step size

3-3-2 Element size

The size of the elements, dL in this chapter, that make up the riser can be varied for the entire riser. Using shorter elements, and thus more elements to build up the model creates a more accurate model. While choosing the element size it has to be kept in mind that the Euler-Bernouilli beam theory is meant for thin beams, with a beam length larger than the beam thickness. As a rule of thumb a beam is categorized as slim when it has a length over thickness ratio of at least 20. It will take more time to use this model in a simulation since increasing the amount of elements increases the amount of nodes, or DOFs, and with that the size of the model. For each section a maximum element size is set which determines the actual size of the element, since each section has a predefined length. Each booster station is modelled as one element, since these are shorter and more stiff than the riser section elements and are therefore expected to add less deflection to the total system.
In order to test the effect of the element length of the beam on the total deflection the element sizes which make up the riser sections are varied. The shortest element used has a length of $24.6m$ which easily fulfils the beam length over beam thickness ratio of 20. In table 3-5 the tip deflection after a simulation time of $3000s$ is shown.

Average element size	DOFs	Maximum offset $[m]$
$24.6m$	408	120.8
$49.1m$	216	121.4
$93.3m$	120	122.4
$186.7m$	68	124.7
$466.7m$	36	132.1

Table 3-5: Total tip deflection while varying element lengths per section

At $3000s$ a difference of several metres is found when comparing offsets, with increasing offsets when element lengths increase. The offset of the approximate model varies with the amount of elements that is used per section. It is expected that a model using element lengths up to $100m$ is suitable for use.

3-4 Comparison to VIVID

Now the approximate model is verified and its sensitivity to time step and element size variations have been tested it is compared to VIVID. Comparing the systems was done by running a simulation exited by a constant current of $0.5m/s$, for $3000s$. This type of simulation was again chosen because for the major part of the time the Mining Support Vessel (MSV) will be sailing at a constant speed. In this section the overall shape, the deflection and the speed at the tip are compared to a simulation created by VIVID where one simulations is with Vortex Induced Vibrations (VIV) and the other without VIV. At last the total tension in the system and the natural frequencies of the systems are compared.

3-4-1 Setup

To create simulation data a continuous model is used, build up as described in this chapter. Each riser section is divided into elements with a maximum length of $100m$ and the booster stations are modelled using one element. This way a system with 60 nodes is created, with 2 DOFs per node. A time step of $0.05s$ is used and the continuous model equations are solved using a Newmark-beta method, described in appendix A.

3-4-2 Deflections

As a first the deflections at every node at steady-state, using the term steady-state described in the previous section, are compared in figure 3-6. The 'jumps' in the deflection are caused by the booster stations, which have a smaller length than the rest of the elements.

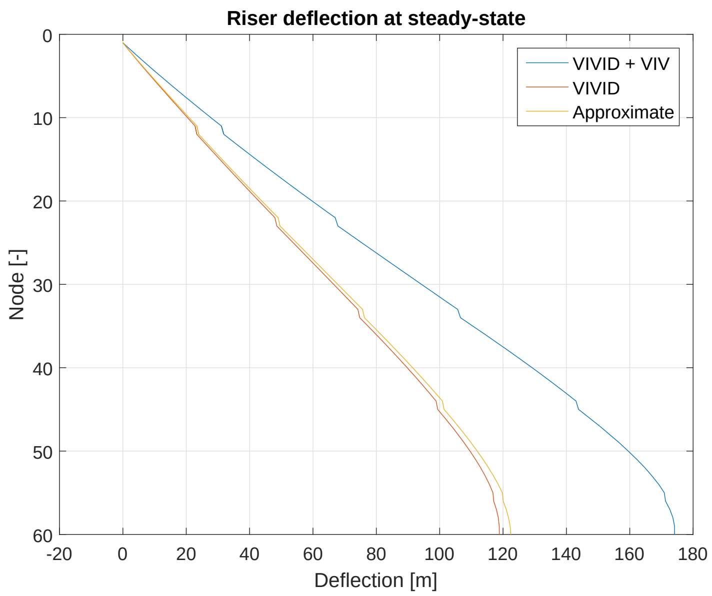

Figure 3-6: Riser deflection per node at $t = 3000s$

The approximate model and the VIVID model without VIV are close when it comes to total deflection. The VIVID simulation that does include the effect of VIV has a total deflection that is much bigger. This is explained by the in-line effect of the VIV which causes an increased drag force. All three simulations take a same shape, where the influence of the clump weight at the tip of the riser is clear.

From figures 3-7 and 3-7 it is again seen that the models show similar behaviour. Both simulations generated by VIVID obtain a larger velocity at start-up, in all three it is seen that the velocity of the tip increases in a short when the ship velocity is set to $0.5m/s$ and settles again. For the approximate model and the VIVID simulation without VIV an offset

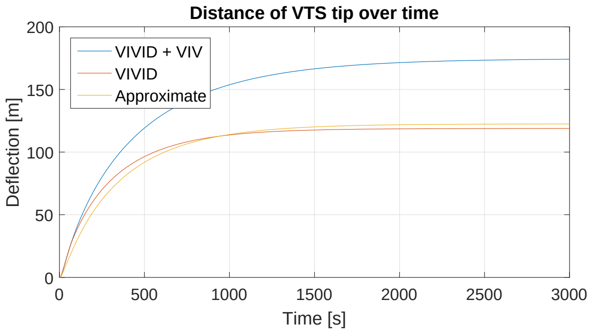

Figure 3-7: VTS tip deflection over time

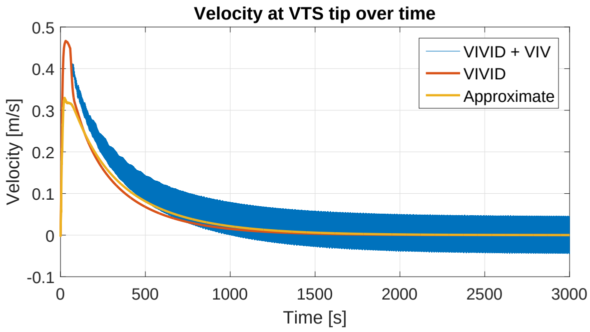

Figure 3-8: VTS tip speed over time

of 3.6m which is 3.0% of the total offset of simulation done by VIVID. In a previous section it is shown that this offset is be decreased when more elements are used to set up the system. The effect of the VIV is clearly visible in both the tip deflection as well as the tip velocity. At the tip the deflection with VIV increases to 174.1m, which is an increase of 55.3m or 46.5% compared to the simulation without VIV. The velocity at the tip of the system does not converge, but varies with an amplitude of about 0.1m/s. It can be seen that the amplitude of this motion increases when the velocity of the tip decreases, which is when the relative flow velocity increases.

3-4-3 Tension

The tension in the VTS is visualized in figure 3-9. It is seen that a large part of the tension is created by the clump weight at the last node. The angle of the tension force line is larger at the top of the system, this is because the riser wall thickness is larger at the ship. The approximate model uses a larger value for the tension force than VIVID.

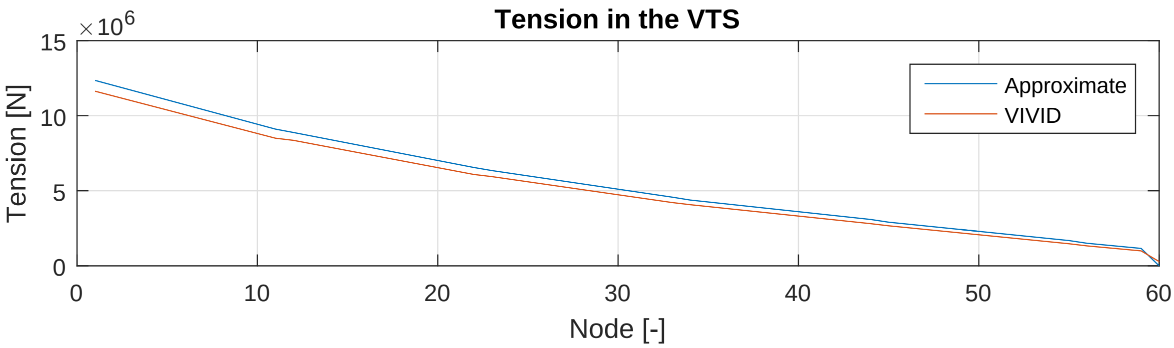

Figure 3-9: Tension in VIVID and approximate model

The error between the tension forces appears to start at the clump weight and slowly increases with the length of the riser. At the top of the system the error has increased and has reached a value of almost 720kN. Compared to the total tension force in the top of the VIVID model this is 6.19% of the total force.

3-4-4 Natural Frequencies

At last the natural frequencies in both systems are compared. VIV does not influence the natural frequencies of the model, since this is an external effect and not a property of the system. The natural frequencies of the approximate model and the VIVID model are found in table 3-6.

Mode	**VIVID** $[rad/s]$	**Approximate model** $[rad/s]$	**Difference** $[\%]$
1	0.034	0.031	9.52
2	0.081	0.074	8.73
3	0.131	0.121	7.38
4	0.183	0.172	5.92
5	0.235	0.214	9.00
6	0.287	0.257	10.33
7	0.342	0.323	5.50

Table 3-6: Natural frequencies from VIVID compared to approximate model natural frequencies

The natural frequencies of the systems are in the same order of magnitude and they are all in the same order of magnitude, with large natural periods. Differences in the natural frequencies vary around 9%. Differences in the natural frequencies can be explained by the difference in tension in the system. The tension creates an addition to the stiffness matrix and the natural frequencies of the system are derived from the mass and the stiffness matrix of the system.

3-5 Conclusions

Conclusions on the approximate model verification and how it compares to VIVID are found over here.

Verification

For the verification is can be seen that the FEM model is accurate for the static case. In the dynamic parts of the verification the model also performs well. It is seen that there are errors and they increase with increasing modes, but since lower modes are of most interest this should not be a problem. The model is not designed to be perfect, but to be an approximate model and the verification shows that it can approximate the analytical solutions. If the approximation is good enough for the Kalman Filter (KF), described in section 2-4, to work properly will be investigated in the next chapter.

Comparison to VIVID

The model behaviour is comparable to the simulations run by the design tool. The difference in tension force is explained because VIVID makes use of the effective tension, which was described in section 2-5-3. Whether this effect fully explains the differences between the

tension forces cannot be checked, it is recommended to do this in the future.
The natural frequencies differ as well which indicates that there are differences between the stiffness matrix and the mass matrix. Since there is a difference in tension, this can be explained because tension is added geometric stiffness. The natural frequencies of a system depend on the full stiffness matrix and the mass matrix, therefore the difference in the natural frequencies can at least partly be explained by the offset tension.
Since the approximate model results are verified it is assumed this model is correct. Differences in results from the approximate model and VIVID are because VIVID contains effects that are assumed negligible in the approximate model. The fact that the two models differ is seen as an opportunity, because in a real world situation it is very likely that there are differences between the simulated system and the measured system as well.

Chapter 4

Implementation of Kalman Filter

This chapter shows how the Kalman Filter (KF) is combined with the Finite Element Method (FEM) model derived in the previous chapter. The system is written to a steady-state form, discretized and expanded to include force as a system state and the observability, controllability and detectability of the system are checked. At last the obtained filtering equations are validated by comparing them to verified results.

4-1 Kalman filter states

In this section it is described how the filter is implemented and combined with the approximate model described in chapter 3. For the regular filter to work the equations of motion that make up the FEM model are rewritten to state-space and then discretized. When a discrete state-space model is obtained the KF is implemented as described in chapter 2.

4-1-1 State-space representation

To implement the KF, the system from equation 3-36 is rewritten in a state-space representation (Åström and Murray, 2008). This way the system is build up from only first-order differential equations which makes it possible to discretize the system later on. In this equation the matrices are the used that were derived in chapter 3.

$$\ddot{x}_w = -\mathbf{C}/\mathbf{M}\dot{x}_w - \mathbf{K}/\mathbf{M}x_w + \mathbf{F}/\mathbf{M} \tag{4-1}$$

The system obtained is written to state-space by using the following equations where $\bar{x}$ is the state-space representation of the deflections and rotations in x-direction.

$$\bar{x} = \begin{bmatrix} x_1 \\ x_2 \end{bmatrix} = \begin{bmatrix} x_w \\ \dot{x}_w \end{bmatrix} \tag{4-2}$$

The equation of motion, equation 4-1, is then written to state space after which a continuous time-invariant system is found. An observer is introduced and written in state-space as well. The observer transform the states from the continuous system to the angles and accelerations of the system as an output. The system is written as.

$$[\dot{\bar{x}}] = \begin{bmatrix} 0 & \mathbf{I} \\ -\mathbf{K}/\mathbf{M} & -\mathbf{C}/\mathbf{M} \end{bmatrix} [\bar{x}] + \mathbf{B} \begin{bmatrix} \bar{u} \end{bmatrix} + \begin{bmatrix} v_k \end{bmatrix} \tag{4-3}$$

$$\hat{y} = \begin{bmatrix} \mathbf{I} & 0 \\ -\mathbf{K}/\mathbf{M} & -\mathbf{C}/\mathbf{M} \end{bmatrix} [\bar{x}] + \mathbf{D} \begin{bmatrix} \bar{u} \end{bmatrix} + \begin{bmatrix} w_k \end{bmatrix} \tag{4-4}$$

In this system $\mathbf{I}$ is the identity matrix. In accordance with the KF equations used in chapter 2, the resulting observer update matrix is written as $\mathbf{H}$. The system update matrix is written as $\mathbf{A}$.

4-1-2 Discrete state-space representation

Contrary to the KF described in section 2-4, in this section a continuous system is described. To implement this system in the KF equations the system has to rewritten to a discrete system. Discretizing the system is done by using the Matlab function 'c2d', which rewrites the system to

$$\begin{bmatrix} \hat{x}_{k+1} \\ \dot{\hat{x}}_{k+1} \end{bmatrix} = \begin{bmatrix} \mathbf{\Phi} \end{bmatrix} \begin{bmatrix} \hat{x}_k \\ \dot{\hat{x}}_k \end{bmatrix} + \mathbf{\Psi} \begin{bmatrix} u_k \end{bmatrix} + \begin{bmatrix} v_k \end{bmatrix} \tag{4-5}$$

In this equation $\mathbf{\Phi}$ and $\mathbf{\Psi}$ are the discrete state-space update matrices. The observer relates the states of the system to the measurement states and therefore no alterations need to be made to the observer. With discrete inputs the observer is written as

$$y_k = \begin{bmatrix} \mathbf{H} \end{bmatrix} \begin{bmatrix} \hat{x}_k \\ \dot{\hat{x}}_k \end{bmatrix} + \mathbf{D} \begin{bmatrix} \bar{u}_k \end{bmatrix} + \begin{bmatrix} w_k \end{bmatrix} \tag{4-6}$$

Time step sensitivity

After the system is discretized the effect of the discretization step size on the system accuracy is observed. The discrete system is run for a simulation time of $3000s$ and compared to the continuous system which is build up using 59 elements and simulated at a timestep of $0.05s$. Three different time steps are used for the discrete system, being $0.1s$, $0.05s$ and $0.02s$. Comparing the systems at an equal time step of $0.05s$ gives insight in the effect of the discretization on the system. Discretizing the system at a smaller and larger time step shows the effect of the time step size on the system.

A comparison between the first five second and last five second of the simulations of the systems is seen in figure 4-1. Only the first and last five seconds are displayed. The first five seconds are interesting to observe because in this timespan the largest variations in motions

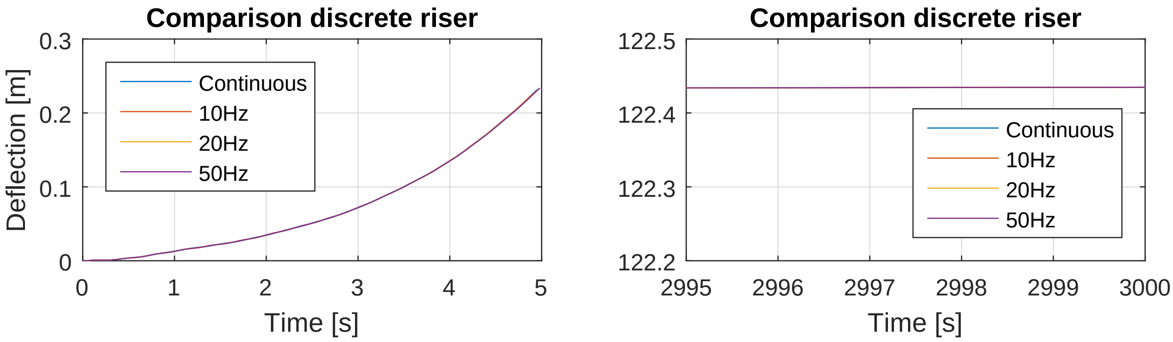

Figure 4-1: Discrete system at varying time step

are seen. In the last five second the behaviour at steady state is observed. In the first five seconds hardly no offset is seen and in the last five seconds offset is impossible to distinguish as well. Over the entire simulation the offset remains very small, the maximum offset values are found in table 4-1. In this table also the Root Mean Square Error (RMSE) is calculated of each discrete system compared to the continuous system. The squared error used in the RMSE is calculated at each point in time where the continuous system and the compared discretized system have an equal time step.

Discrete system	**RMSE** $[mm]$	**Maximum offset** $[mm]$
$10Hz$	0.03	-0.6
$20Hz$	1.62	8.8
$50Hz$	2.58	14.0

Table 4-1: RMSE of dicrete system compared to continuous system sampled at $20Hz$

Overall it is seen that using a larger time step, or a lower sampling rate causes the discrete system to underestimate the deflections which also results in a negative maximum offset. Increasing the sampling frequency increases the offset, but still the offset is negligible compared to the total deflection of the system.

4-2 Force adaptive filtering

Because the force over the riser can only be measured at a few points, it is unknown over the largest part of the riser. This creates an uncertainty in the calculations that are done to obtain the input force. In order to account for this uncertainty the input force is added to the system as an extra state (Verhaegen and Verdult, 2007).
The force matrix is split into two parts. The first part comes from the imposed displacements which are not part of the left hand side of the equations of motion, as derived in subsection 3-1-4. This part of the force is well known since the shipmotions can be measured accurately. Therefore no uncertainty is added to this part and the force is added by the input matrix $\mathbf{B}$. The second part of the force is the drag force. The drag force is a non-linear force and therefore it has to be linearized before it can be added to the linear KF equations. In order to avoid this linearization, which would make calculating the drag force less accurate, it is assumed that the drag force is constant in time. The drag force can now only be added to

the equations as an initial condition that does not vary afterwards, as is done in equation 4-7. An extra column is added containing the term $\mathbf{I}/\mathbf{M}$, that adds the force to the accelerations.

$$\begin{bmatrix} \dot{x}_w \\ \ddot{x}_w \\ \dot{F} \end{bmatrix} = \begin{bmatrix} 0 & \mathbf{I} & 0 \\ -\mathbf{K}/\mathbf{M} & -\mathbf{C}/\mathbf{M} & \mathbf{I}/\mathbf{M} \\ 0 & 0 & 0 \end{bmatrix} \begin{bmatrix} x_w \\ \dot{x}_w \\ F \end{bmatrix} + \mathbf{B} \begin{bmatrix} 0 \\ u \\ F \end{bmatrix} + \begin{bmatrix} v_k \end{bmatrix} \tag{4-7}$$

Now the drag force in the approximate model no longer varies, which is not a very realistic assumption. By adding the force to the states, combining the approximate model with the KF make it possible to observe and update the force through the KF equations. This means the force is still updated, but through the relative velocity measurements. The relative velocity measurements are squared and multiplied by $\frac{1}{2} C_d \, \rho_{sea} \, D$ to obtain force measurements. The observer is now written as

$$y = \begin{bmatrix} \mathbf{H} & \mathbf{I} \end{bmatrix} \begin{bmatrix} \bar{x} \\ F \end{bmatrix} + \mathbf{D} \begin{bmatrix} \bar{u} \\ 0 \end{bmatrix} + \begin{bmatrix} w_k \end{bmatrix} \tag{4-8}$$

Discretization of the force adaptive system gives

$$\begin{bmatrix} \bar{x}_{k+1} \\ F_{k+1} \end{bmatrix} = \begin{bmatrix} \mathbf{\Phi} \end{bmatrix} \begin{bmatrix} \bar{x}_k \\ F_k \end{bmatrix} + \begin{bmatrix} \mathbf{\Psi} \end{bmatrix} \begin{bmatrix} \bar{u}_k \\ 0 \end{bmatrix} + \begin{bmatrix} v_k \end{bmatrix} \tag{4-9}$$

$$y_k = \begin{bmatrix} \mathbf{H} & \mathbf{I} \end{bmatrix} \begin{bmatrix} \bar{x}_k \\ F_k \end{bmatrix} + \mathbf{D} \begin{bmatrix} \bar{u}_k \\ 0 \end{bmatrix} + \begin{bmatrix} w_k \end{bmatrix} \tag{4-10}$$

Adding a extra states to the system means the process covariance matrix Q has to be expanded, so it can include the force covariance. The measurement covariance matrix R is expanded as well.

4-2-1 Force matrix reduction

In the system only thirteen forces are measured and updated. The forces on the other nodes of the system vary only very little because they are assumed constant in the approximate model. To increase the effectiveness of the method the amount of Degrees Of Freedom (DOFs) is reduced. This is done by only adding the forces at the top and the bottom of the booster stations, and at the Mining Support Vessel (MSV) as states. These are the nodes that coincide with the measurement point, so at these nodes the forces are updated. The forces are then linearly distributed over the riser as seen in figure 4-2.

On the left the yellow arrow indicates a force that is measured at the bottom of a booster station. This force is linearly distributed over the riser section until it reached zero at the top of the booster station below. The top force of the booster station below, shown in blue, is linearly distributed over the riser section upward until it reaches zero at the booster station above. By summing these forces a linearly distributed load is found, seen on the right as the green line. Because the booster stations are modelled as two nodes, no linear distribution is made over the booster stations. The linear distributed load that is obtained is seen at the right of figure 4-2.
The force adaptive KF is tested in appendix D.

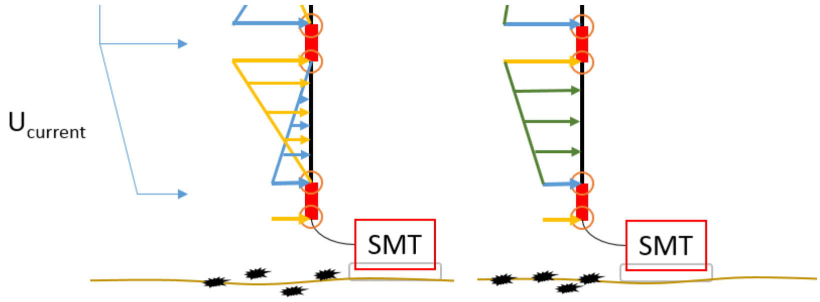

Figure 4-2: Distributed force over the riser

4-3 Observability and controllability

In the next subsections the observability, controllability and detectability of the system have been determined. These characteristics of the observer are useful when it comes to determining the stability and controllability of the system and its observer. The observability, detectability and controllability have been determined for a continuous system with 147 DOFs.

4-3-1 Observability

Determining the observability of the system is important when designing a KF. The observability of a system is a way to define the ability to determine a previous state of a system using the available measurements. A continuous system is said to be fully observable if one of the two following conditions is met: (Gelb et al., 1974)

- A system is observable if the state at t_0 can be fully determined by observing only the outputs $y(t_1)$
- A n^{th} order system is fully observable if its observability matrix, given by 4-11, is of rank n.

The observability matrix is created by using the following equation

$$\mathbf{O} = \begin{bmatrix} \mathbf{H} \\ \mathbf{H\,A} \\ . \\ . \\ \mathbf{H\,A}^{n-1} \end{bmatrix} \tag{4-11}$$

In this equation $\mathbf{A}$ is the state-space matrix of the system and $\mathbf{C}$ is the observer matrix. The observability matrix $\mathbf{O}$ is of full rank when the rank of the matrix is equal to n.
The rank is determined by observing the amount of eigenvalues extracted using a singular value decomposition. All of the singular values are plotted in figure 4-3. In this figure the Vertical Transport System (VTS) is modelled in its standard configuration, element lengths of $200m$ have been used which creates a system with 147 DOFs. When shorter elements are used this results in a larger amount of DOFs which makes the technique explained in this subsection unusable due values that are too large for Matlab to process obtained through the

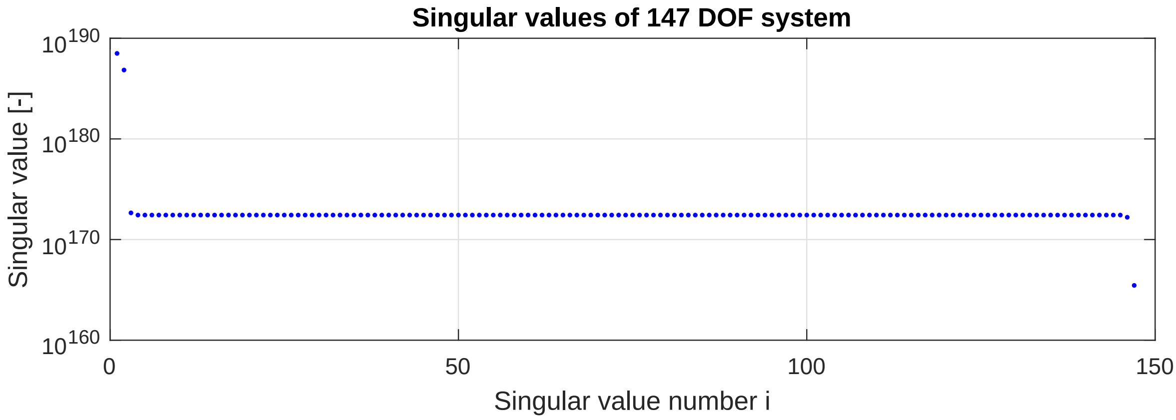

Figure 4-3: Plot of singular values

$\mathbf{A}^{n-1}$ term.
From the plot in figure 4-3 it can be seen that the system shows unexpected behaviour. All of the singular values are large and most of them are in the order of 5.5^{171}. Two of the singular values are must larger than the others and a few are much lower. By using the Matlab function 'rank()', the observability matrix is determined to be of rank 2 for a system of 147 DOFs. This might be due to the two largest singular values which are much larger than the rest of the singular values. A rank of two means the system is not fully observable.

4-3-2 Detectability

Detectability is a weaker version of the previously treated property of observability. If a system is not fully observable it does not have to be unstable. When the unobservable states of the system are stable the system is said to be detectable. (Ray, 1981)
The system is detectable when the matrix determined in equation 4-12 is of full rank. (Remsing, 2006)

$$\mathbf{D_t} = \begin{bmatrix} \lambda\mathbf{I} - \mathbf{A} \\ \mathbf{C} \end{bmatrix} \tag{4-12}$$

In this equation $\mathbf{A}$ is the assembled state-space system of the system and $\mathbf{C}$ is the observer matrix. λ are the eigenvalues of the assembled system $\mathbf{A}$. When the rank of the matrix $\mathbf{D_t}$ is determined, where $\mathbf{D_t}$ is created using the same system used in the previous subsection, $\mathbf{D_t}$ is found to be of full rank. This means the system is stable.

4-3-3 Controllability

A system is said to be controllable if an external input can move the states of a system to a target final state in a finite time. The controllability matrix is constructed in a similar way as the observability matrix, it is constructed using equation 4-13.

$$\mathbf{C_o} = \begin{bmatrix} \mathbf{B} \\ \mathbf{B\,A} \\ . \\ . \\ \mathbf{B\,A}^{n-1} \end{bmatrix} \tag{4-13}$$

In this equation $\mathbf{A}$ again is the state-space matrix of the system, $\mathbf{B}$ is the varying force input matrix as derived in equation 4-7. Using the 'rank()' function in Matlab once more the controllability matrix is determined to be of rank 2. This low rank means the system is not fully controllable.

4-4 Verification

In order to verify whether the KF is implemented correct a comparison is made between the KF functions implemented in Matlab and the equations as used in this thesis.

4-4-1 Model setup

To keep the comparison simple and to avoid long computation times for the verification the same system is used as in A. This system is seen in figure A-1, it has three DOFs and uses the same parameters (table A-1) and input force as this system. Rewriting the system to state-space creates a system with six states, three position states and three velocity states. For the initial conditions the first mass is offset by 2 metres, the third mass has an initial velocity of $5m/s$. All other initial offsets and velocities are set to zero. A time step of $0.05s$ is used to create measurement data.

4-4-2 KF setup

The KF is setup as seen in the block scheme in 4-4. Noise v_k is added to the input u which creates an output to which noise w_k is added to create measurements. The same input u is used in the model that creates the state estimate and the observer output. These outputs are added and combined in the KF. For implementation in the KF the system is first written to state-space and discretized as described in this chapter. The discretized state-space system is used in both the KF build from Matlab functions as for the KF build using the KF equations.

For the filtered model the initial conditions are different than for the model used to create the measurements of which the initial conditions are described in the subsection above. In the filtered model the masses start at $\bar{x} = 0$ and the third mass has an initial velocity of $3m/s$. Initial velocities of the other masses are equal to zero. To avoid having to resample the measurement data the KF uses a time step of $0.05s$.
At the start value for the initial covariance P_0 has to be determined. This initial covariance is a guess which is set as $P_0^- = Q$. For a stable observable system the error covariance matrix converges to a steady state. The better the initial guess, the faster the covariance converges. This can be an important factor in systems with little measurement time, but in the case of the VTS there is enough time for the error covariance matrix to converge.

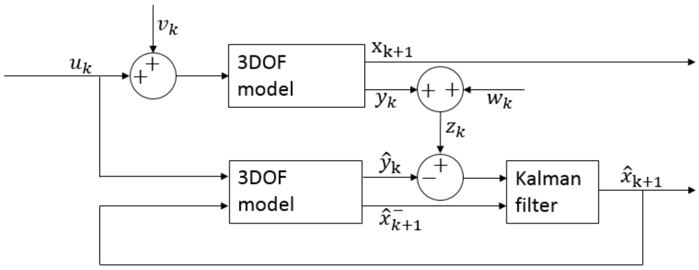

Figure 4-4: Kalman block scheme

4-4-3 Results

The results of the filtering process can be observed both visually and numerically. If the Kalman equations are implemented correctly the filtered state should be able to track the system states. A difference between the KF implemented using Matlab functions and the implemented KF equations is that the Matlab functions first solves the riccati equations that can be used to calculate a steady-state gain and error covariance. This results in shorter start-up behaviour for the KF system implemented using Matlab functions.

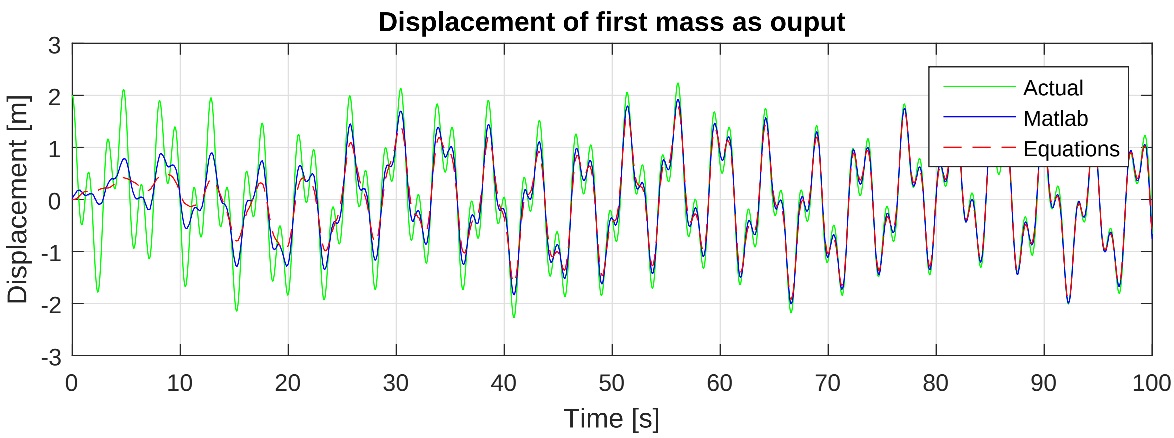

Figure 4-5: Kalman filter comparison

Figure 4-5 confirms this behaviour and during start-up a clear difference is seen between the Matlab functions, depicted as 'Matlab' in the plot. The original state is shown as 'original'. The system implemented using the KF equations is seen to perform less during start-up, but is shown to perform equal over time. This is when the Kalman gain and error covariance matrices have converged to a steady-state. Convergence of the Kalman gain matrix entries is shown in figure 4-6. The converged Kalman gain matrix is numerically compared to the Kalman gain matrix calculated by Matlab functions in table 4-2.

In order to verify this the system that is implemented using the KF equations is run using the steady-state Kalman gain and error covariance as initial conditions for the Kalman gain and error covariance. As a results these matrices do not need to converge and the KF set up using the KF equations should perform equal to the system set up using Matlab functions.

This is confirmed by figure 4-7 and table 4-2. In this figure it is seen that both during and after

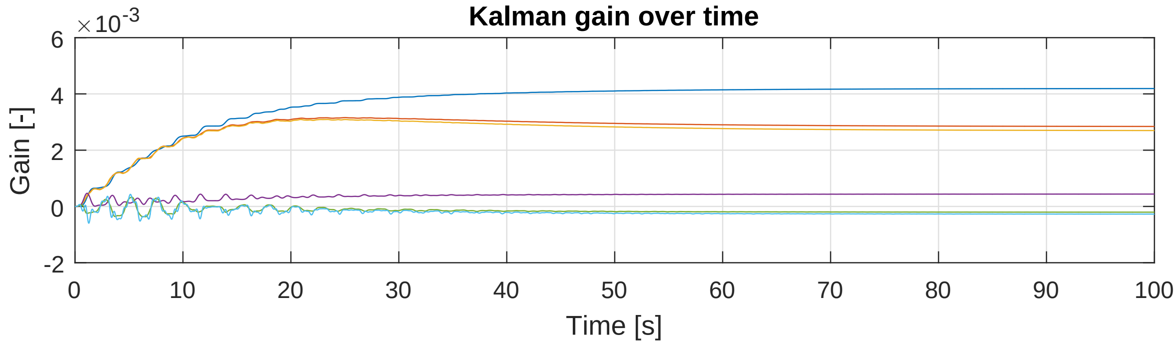

Figure 4-6: Kalman gain convergence

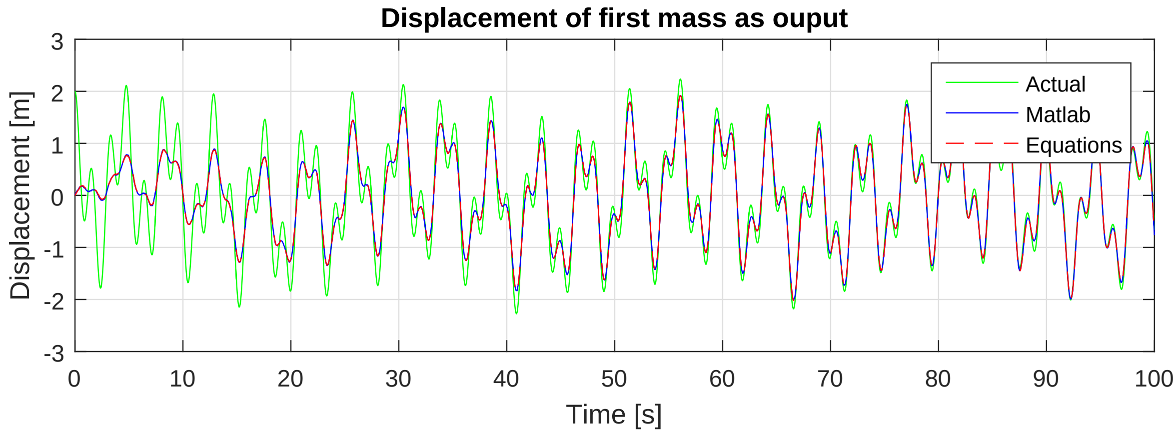

Figure 4-7: Kalman filter with optimal gain

start-up the filters perform the same. The RMSE is calculated in table 4-2 as the difference between the filtered system and the original system. In the simulation where the Kalman gain and error covariance matrices have to converge a clear difference is seen in the RMSE values, this is because at start-up there is a clear difference between the KF setup using Matlab functions and using the Kalman equations. When the steady-state Kalman gain and error covariance are used as initial conditions in the KF setup using the Kalman these matrices do not have to converge and the systems perform almost equal, confirmed by the RMSE values for both systems.

4-5 Conclusion

Conclusions about the discretization results, the system observability and the Kalman filter verification are found in this section.

4-5-1 System discretization

Discretizing the system has no significant influence on the system performance. The maximum offset and the RMSE are low compared to the total offsets and are hardly influenced by varying

Parameter	Matlab functions	Kalman equations
Gain state 1	$4.19 \cdot 10^{-3}$	$4.19 \cdot 10^{-3}$
Gain state 2	$2.84 \cdot 10^{-3}$	$2.84 \cdot 10^{-3}$
Gain state 3	$2.70 \cdot 10^{-3}$	$2.69 \cdot 10^{-3}$
Gain state 4	$0.44 \cdot 10^{-3}$	$0.44 \cdot 10^{-3}$
Gain state 5	$-0.20 \cdot 10^{-3}$	$-0.20 \cdot 10^{-3}$
Gain state 6	$-0.27 \cdot 10^{-3}$	$-0.27 \cdot 10^{-3}$
RMSE converging	$0.348m$	$0.466m$
RMSE converged	$0.348m$	$0.350m$

Table 4-2: Kalman gain and RMSE calculated via Matlab functions and KF equations after converging

the sampling step.

4-5-2 Observability

Whether the rank of the system really is equal to two is up for discussion because all of the singular values are far above zero. A low estimation by the Matlab function can be explained by numerical errors introduced by the large number of DOFs in the system. The same goes for the controllability of the system.
That the system is not fully controllable is not of much importance in this case since the goal of this thesis is to be able to observe the VTS. No active control (other than the motions of the ship) can be used to control the motions of the riser.
The system does appear to be fully detectable. This is shown in subsection 4-3-2 and this is confirmed by the convergence of the observations shown is appendix D.

4-5-3 Verification

The KF equations are verified by comparing the results to a setup created by Matlab. It is seen that the error covariance converges to a steady-state and the same error covariance is obtained through iterations as through solving the Riccati equation.

Chapter 5

System sensitivities

In this chapter the sensitivities of the force adaptive Kalman Filter (KF) are tested. The first sensitivity that is checked is varying the process covariance noise. After this check an optimal process covariance noise is chosen. Using this covariance noise setting the influence of the amount of measurement per second, and thus the amount of filtering steps per second, is determined. Finally the influence of a bias in the sensors is checked.

Cases

In total three sensitivity cases are distinguished.
First the influence of the noise covariance matrix on the system is observed. The process noise covariance is used to give a weight to the uncertainty of the approximate model. Varying the process covariance is done for two simulations created by VIVID. In the first simulation the riser is exited by a constant current and Vortex Induced Vibrations (VIV) are taken into account. For the second simulation the riser is exited by a varying current, in this simulation VIV do not effect the riser. The process covariance for which the system is found to perform best is used as process covariance in the following cases.
Second the influence of varying the measurement frequency is observed. Because the drag force is not calculated by the model, but updated through the KF equations it is expected that using a high update frequency a smooth force profile can be obtained. Since the drag force is the main influence on the motions of the riser this can improve the results.
Third the system is tested with biased sensors. A bias in the sensors can create a disruption in the ability of the observer to monitor the system motions.

5-1 Loading measurement data

The data from VIVID needs to be altered so it can represent measurement data. In this section it is described which data is selected and how measurement noise is added.

5-1-1 Node distributions

For each section the top and lower nodes are equal to the top and lower nodes of the VIVID simulation. For the booster stations the top node is the same node as that of the top node of the booster station in the VIVID simulation, and the bottom nodes also are equal. All nodes between are left out, this way the only measurements come from to top and bottom of the booster stations.
If in the VIVID simulation a larger time step is used compared to the amount of measurements done by the KF all data is interpolated linear in time. When a smaller time step is used data between measurement points is discarded.

5-1-2 Measurement noise

Noise is added to the data obtained at the measurement points at the tops and bottoms of the booster stations. The noise for the angle and acceleration measurements is added by multiplying the standard deviation of each sensor, found in section 2-1 with a normal distributed random generated noise.
To add noise to the force measurements, the standard deviation of the relative flow sensor is first added to the relative flow measurements. These relative flow measurements are then used in the drag equation to create noisy force measurements which are measured in Newtons.

5-2 Process noise sensitivity

Multiple runs have been done with a varying process noise because this is of a large influence on the KF performance (Jwo and Cho, 2007). The observer performance is checked visually for each simulation and also the Root Mean Square Error (RMSE) and the Variance Accounted For (VAF) are calculated. The RMSE is determined as the root of the mean squared error between the data created by VIVID and the observation from the Kalman filtered system. A low RMSE corresponds to a low error, which is desired. The VAF is calculated by taking the variance of the difference between the original signal and the signal created by the observer divided by the variance of the original signal. When two signals perfectly overlap a fit percentage of 100% is found. Formulas to calculate the RMSE and VAF are found in appendix B.

5-2-1 Process noise and covariance

In the first case the process noise is varied, which is used to create the process covariance matrix Q. The process noise is used to account for behaviour of the VIVID model that is not present in the approximate model. In earlier chapters unknown behaviour was created by introducing the process noise, with a known standard deviation, to the system as v_k. Now that VIVID is used to create the data the process noise is present in the model. A block scheme of the system is seen in figure 5-1.

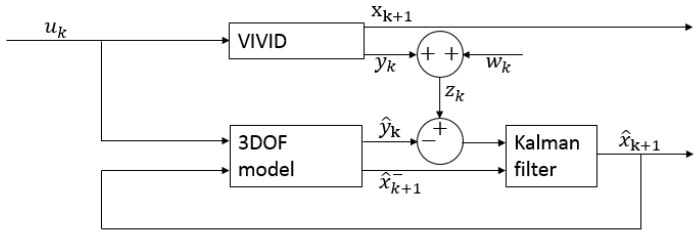

Figure 5-1: Block scheme of the Kalman filtered system with simulation data generated by VIVID

Process noise

Contrary to the previous tests of the KF, where a known process noise was added to the outputs of the model to create uncertainties, this time a standard deviation of the process noise has to be estimated. For each of the measured states a different amount of noise has been assumed in order to check which amount of process noise works best for this system. Because the KF calculates a weighted gain based on the ratio between the measurement covariance and the process covariance the amount of process noise is varied around the amount of sensor noise. This way for each test the KF puts more weight to either the approximate model or the measurements. Since only the sensitivity of the KF to the amount of process noise is observed and no optimization is attempted, the amount of process noise is created by either multiplying the measurement noise by a factor of $1 \cdot 10^1$ or $1 \cdot 10^{-1}$. Creating process noise by multiplying the measurement noise with a factor $1 \cdot 10^1$ creates an observation where the process noise is larger than the measurement noise, so more weight is given to the estimates from the sensors. Creating process noise by multiplying the measurement noise with a factor $1 \cdot 10^{-1}$ results in a larger weight to the estimations from the approximate model. The measurement noise varies for all three sensors, these variations are used for the three different states, this results in a different amount of process noise per state. Multiplying the measurement noise with a factor of $1 \cdot 10^1$ is referred to as a 'high' noise case, multiplying with a factor $1 \cdot 10^{-1}$ is referred to as a 'low' noise case.
When the observer is run with the 'low' and a 'high' noise cases this results in eight simulations for every case mentioned below. Every case is given a different simulation number where the location of the number corresponds to the state of the noise. The value of the number indicates a 'low' or a 'high' process noise for this state. All eight cases are found in table 5-1. Multiplication factors of $1 \cdot 10^1$ and $1 \cdot 10^{-1}$ are chosen since these are found to create a clear variation for each case.

In each of the cases the results of the accuracy at the tip of the system is compared, since this is the point of interest. The noise case which yields the most accurate results is later on used for further sensitivity analysis.

Covariance

The process covariance matrix is directly related to the process noise. Values used to create the process covariance matrix are equal to the squared values used to create the process noise.

Noise distribution	Noise on x_k	Noise on $\dot{x}_k$	Noise on F_k
low low low	$1 \cdot 10^{-1}$	$1 \cdot 10^{-1}$	$1 \cdot 10^{-1}$
low low high	$1 \cdot 10^{-1}$	$1 \cdot 10^{-1}$	$1 \cdot 10^{1}$
low high low	$1 \cdot 10^{-1}$	$1 \cdot 10^{-1}$	$1 \cdot 10^{-1}$
low high high	$1 \cdot 10^{-1}$	$1 \cdot 10^{1}$	$1 \cdot 10^{1}$
high low low	$1 \cdot 10^{1}$	$1 \cdot 10^{-1}$	$1 \cdot 10^{-1}$
high low high	$1 \cdot 10^{1}$	$1 \cdot 10^{-1}$	$1 \cdot 10^{1}$
high high low	$1 \cdot 10^{1}$	$1 \cdot 10^{1}$	$1 \cdot 10^{-1}$
high high high	$1 \cdot 10^{1}$	$1 \cdot 10^{1}$	$1 \cdot 10^{1}$

Table 5-1: Multiplication factors for the process noise related to that of the sensor noise

Because the process noise is assumed to be uncorrelated, all off diagonal entries of the process covariance matrix are equal to zero.

5-2-2 Observer

The system that creates the estimated state updates is build up the same way as was done in chapter 4. Each riser section is divided into 10 elements, the booster stations are not divided and are simulated as one beam element each. Section one, the section attached to the clump weight is shorter than the other sections and is divided into three elements. This way a system with 60 nodes is created, with 2 Degrees Of Freedom (DOFs) per node.
The observer is build up exactly the same as the system used to create the estimated states, but then with a reduced amount of states, equal to the amount of measurements made.

5-2-3 Simulation results

The results of the simulations with varying process noise are found below. Two simulations are tested in this chapter, as third simulation in which the Vertical Transport System (VTS) is only exited by waves is found in appendix E. First in this chapter a case with a relative flow current is tested. When a constant current is introduced the system approximates a steady state as found in simulations from chapters before. In the data generated as measurements is created by a simulation in which VIV is present. In appendix E a simulation t steady state without VIV is introduced. The results from the system with a KF are compared to the results of the approximate model without a KF. A final simulation is done in which the approximate model is exited by a varying current. This way not only the steady state of the system, but also its ability to track variations in the deflections is observed. In this case the measurement data is created by a system where VIV was not introduced.
In each of the simulations the same wave excitations have been used. The waves have been simulated as a random imposed motion at the top of the system with a zero mean.

Constant relative flow and vortex induced vibrations

In the first case the ability to observe the system as it converges to a steady-state is checked. For this case the same simulation as in 3-4 is used. For the simulation data created by VIVID a time step of 0.05 seconds has been used. VIV is present in the system which results in a VIVID simulation with a large deflection compared to the approximate model.

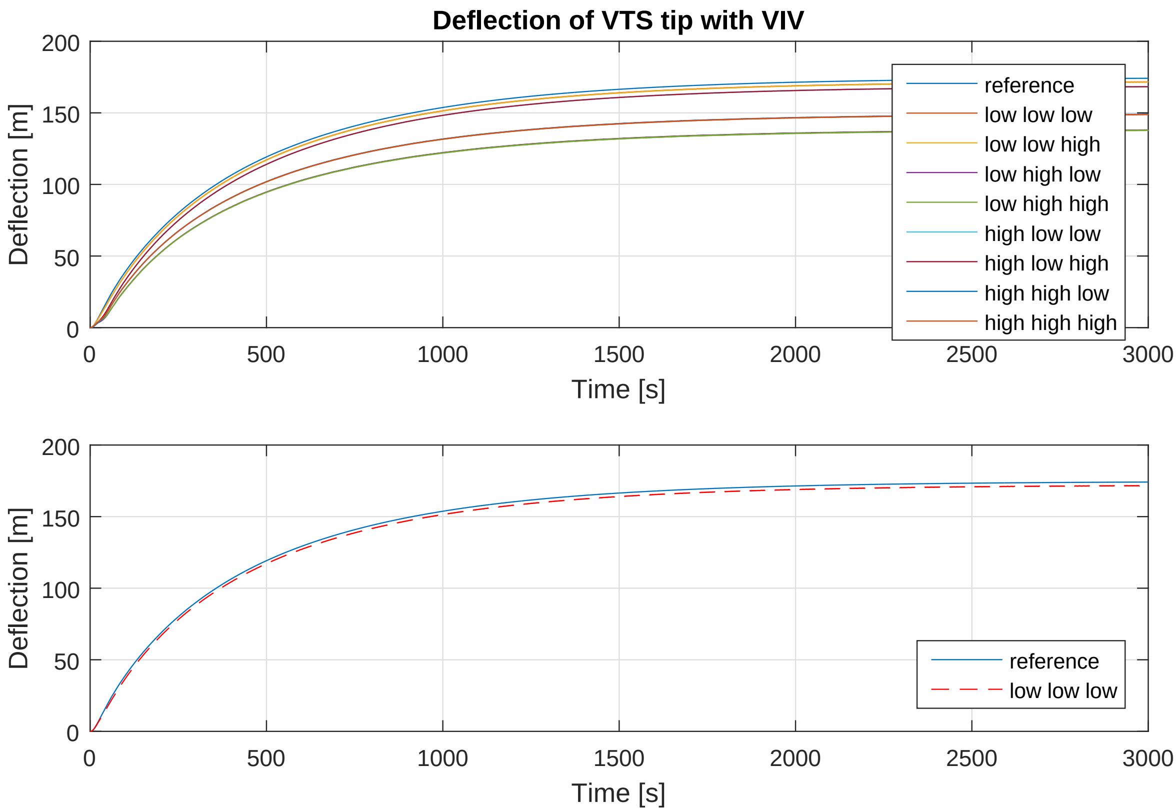

Figure 5-2: Deflection of tip of VTS multiple simulations

The deflection of the tip of the system is seen in figure 5-2. In the upper plot the spread of the observations is seen, in the lower plot only the best result is plotted. All of the observations obtain smaller deflections than was simulated by VIVID. This is a logical result since the simulation from VIVID includes VIV which results in an increased drag. Although none of the observations manages to achieve a 100% fit compared to the VIVID simulation, it is seen that the system performs better than was the case in section 3-4. Although the KF performs well, it is seen that in each case a steady offset is left over that is not filtered out. This can be explained by the type of measurements that are being done. In appendix D, it is seen that the measurements, like the rest of the system converge to a steady state quickly. When riser goes to a steady state the acceleration measurements approach zero which causes the riser to come to a standstill. The constant offset between the observer and the VIVID simulation is not filtered out because the acceleration measurements are observed well so no further motion is created.

In table 5-2 for every simulation the RMSE and VAF are calculated, this way the closeness of the fit of the filtered results is determined. It is found that simulations with a low noise on the angles perform best. This means that the KF gives a larger weight to the estimations made by the approximate model than made by the accelerometers. Assuming a low process noise

Simulation noise	RMSE $[m]$	VAF $[\%]$
low low low	2.364	99.99
low low high	2.506	99.99
low high low	31.760	96.42
low high high	31.004	96.38
high low low	5.533	99.98
high low high	5.640	99.98
high high low	22.166	98.37
high high high	22.341	98.35

Table 5-2: RMSE and VAF for $3000s$ simulations, including VIV

for the angle sensors results in a better as well. For the force process noise it is also found that a low amount of process noise creates the best results. This is remarkable since the model itself does not include any force updating and receives its inputs from the measurements. It is probably due to the converging of the simulation that this results is obtained. Since the model goes to a steady state the force becomes constant as well, when a force is obtained the model used in the approximate model does not vary this force. This means that a more stable result is obtained by putting more weight on the approximate model, which results in a more stable force estimation and in the end a better overall result.

Varying current

In this case the current on the riser has been varied to simulate a ship sailing at a varying velocity, which is the case when the full Deep Sea Mining (DSM) system is build. The current profile at each time step is constant across the entire length of the riser.

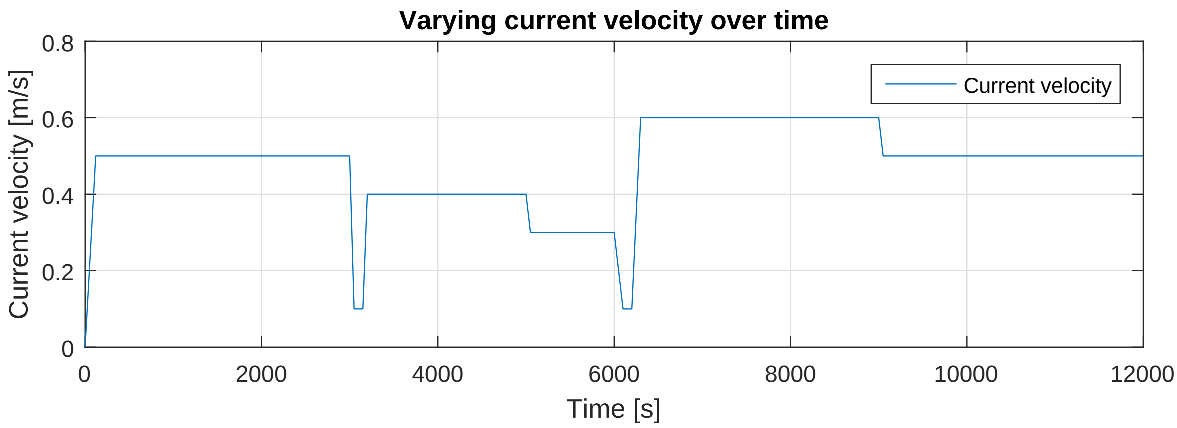

Figure 5-3: Variation of the current imposed on the riser

Variations in the ship velocity, implemented as a varying current are visualized in figure 5-3. For the simulation data created by VIVID a time step of 0.1 seconds is used. VIV is not present in the system. In figure 5-4 the deflections of the tip of the VTS are seen. The upper plot again shows the spread of the deflections, the lower plot shows the result with the smallest RMSE and the highest VAF.

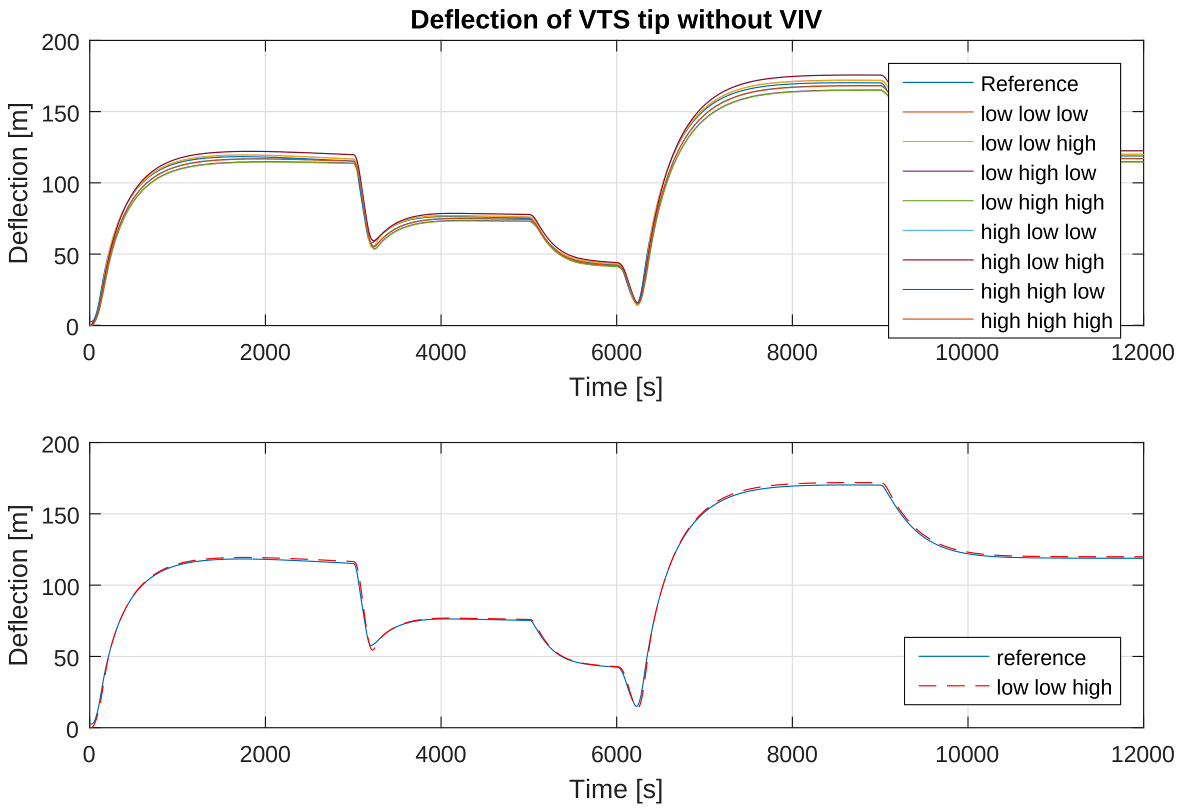

Figure 5-4: Deflections of riser tip with varying current

Contrary to the simulations with VIV from the previous section this time the simulations after filtering obtain both larger and smaller deflections than VIVID. It is seen that the simulations that use a high process noise for the accelerations tend to underestimate the deflections, cases in which a low process noise is used for the accelerations overestimate the deflections. This is a logical result since it was seen in section 3-4 that the approximate model tends to overestimate the riser deflections. When more weight is given to the approximate model estimation this causes the filtered result to overshoot. Angles in the VIVID simulation and approximate model are comparable and as a result the system performs better with low angle process noise.
Another difference between the results of this case and the previous simulation is that the system performs best with a high process noise. This can be explained because the force varies due to the varying imposed current. By giving more weight to the measured force, variations in the force are picked up quicker which creates a better result.

In table 5-3 it is confirmed that the simulation that uses a low factor for the process noise on angles and accelerations and a high process noise for the force state shows the best performance.

Simulation noise	RMSE $[m]$	VAF $[\%]$
low low low	1.468	99.93
low low high	1.364	99.93
low high low	4.410	99.71
low high high	4.634	99.71
high low low	3.891	99.72
high low high	3.798	99.72
high high low	2.377	99.84
high high high	2.514	99.84

Table 5-3: RMSE and VAF for $12000s$ simulations

5-3 Varying measurement frequency

In the beginning it was stated that the model had to be able to run in real time. This is hard to check, since the amount of computational power available and the software used to write the program in has a big influence on the time needed for the computations. It is possible to check the effect of the amount of measurements per second versus a set benchmark time. For the benchmark measurement frequency of $20Hz$ is used, the same as was used in the previous tests. The process noise from the simulation described as *low low high* is used. Three simulations are compared with sampling frequencies of $10Hz$, $20Hz$ and $50Hz$.

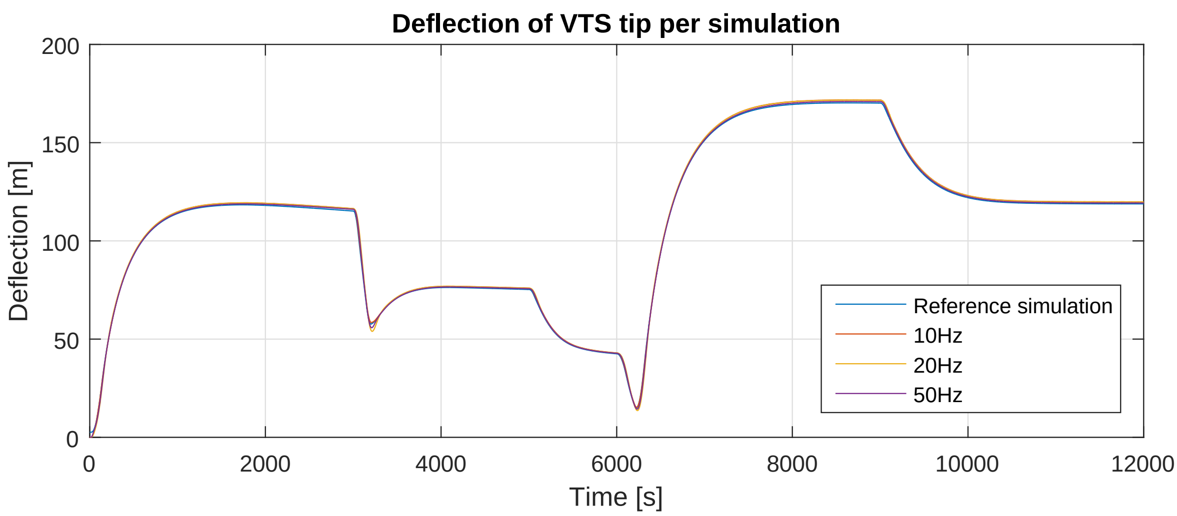

Figure 5-5: Variation of the amount of measurements per second

The results of the simulations can be found in figure 5-5, which shows the tip deflection for each case, against a reference simulation. From the figure it is seen that varying the measurement frequency does not have a visible effect on the amount of deflections.

From the calculations of the RMSE and the VAF in table 5-4 an unexpected result is seen. Both simulations run using a different time step perform better than the simulation with an update frequency of $20Hz$. The observer that is run using 10 measurements per second, decreases the RMSE and increases the VAF. The best result is obtained using a measurement frequency of $50Hz$. This can be explained by the way the force is updated. The measured

Frequency $[Hz]$	**RMSE** $[m]$	**VAF** $[\%]$
10	1.031	99.98
20	1.364	99.93
50	0.644	99.98

Table 5-4: RMSE and VAF for the $12000s$ simulations at varying measurement frequencies

force is combined with an estimate, but the estimate is equal to the force from the previous state, so a larger measurement frequency can create a smoother force profile. This explanation is contradicted by the results obtained from measuring at $10Hz$.
Improving the results by increasing the measurement frequency increases the required simulation time, the time used to observe a 12000 second simulation at varying frequencies is compared to the $20Hz$ case in table 5-5.

Simulation	**10Hz**	**20Hz**	**50Hz**
Dimensionless time	0.76	1.00	2.88

Table 5-5: Dimensionless time per simulation

In this table it is seen that is takes 2.88 times as long to run a simulation with 2.5 times as many time steps.
For the rest of the thesis a measurement frequency of $20Hz$ is used, because this leads to comparable results.

5-4 Sensor bias

For the final case a bias is introduced in the sensors. Biased sensors are a realistic scenario since a bias is quickly introduced, when sensors are not optimally calibrated or when temperature fluctuations occur that are not accounted for.
It is expected that a bias in the sensors has a big effect on the performance of the observer. This is because the steady state shows an error that cannot be filtered out. Creating an offset in the measurements can greatly increase this error. The values for the bias per sensor can be found in section 2-1. For the angular sensor the bias is set equal to an angular random walk value of one hour.
The bias is introduced at one type of sensor at the time, this is done to avoid interference from the other sensors and this way the influence of a bias per sensor type can be observer more easily. The biasses are introduces randomly to the sensors and are multiplied with -1, 0 or 1. So the sensors is either fully biased in a positive or negative way or not biased at all. For the process noise the process noised used in the optimal simulation with low angular and acceleration process noise and high force process noise, from subsection 5-2-3 is used. In figure 5-6 the results of the biased sensor reading is found.

From the figure it is seen that hardly any differences occur between the bias per sensor type. This is confirmed by table 5-6. The small influence of the bias can be explained in three ways.
As a first the bias may have been small relative to the noise influenced overall measured values. This can have caused the bias to only have a small effect. For the force sensors this

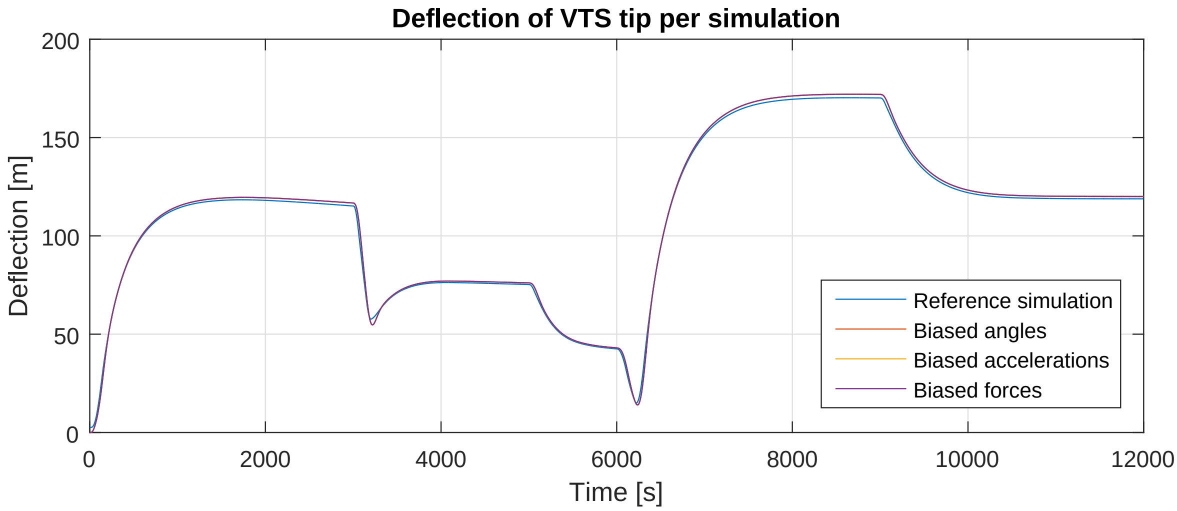

Figure 5-6: Observer performance with biased sensors

is a likely scenario, but it is countered by the results from biased acceleration sensors. The bias on the acceleration sensor is high compared to the amount of noise that influenced the sensor and still the observer performance was hardly influenced.
A second explanation is that the bias was not applied to all sensors and the sensors it was applied to were given the full bias, with either a positive or negative sign. This may have caused the biases to counter each other and helped the observer obtain a good fit.
The most influence probably comes from the way the bias is introduced. In order to check bias disturbances apart from each other the sensor biases were introduced per type of sensor. A result from this is that the other two sensor types are able to compensate for the inaccurate measurements from the biased sensors.

Biased sensors	**RMSE** $[m]$	**VAF** $[\%]$
Angular	1.452	99.93
Accelerometer	1.452	99.93
Relative flow	1.452	99.93

Table 5-6: RMSE and VAF for the $12000s$ simulations with biased sensors

From the RMSE and the VAF it is seen that the bias enlarges the RMSE compared to the value calculated for optimal process noise simulation *low low high* by 0.25%.

5-5 Conclusions

In this section conclusions are found for each of the observed cases.

5-5-1 Varying noise

With the riser excited by a constant current and VIV the observer performed well. The fit that is achieved is close and in steady state the error between the observer deflection and original system deflection is small compared to the total deflections. In the steady state is can be seen that an offset remains between the VIVID simulation and the observer that is not filtered out by the observer.
When the VTS is exited by a varying current comparable results are achieved as was the case with a constant current. This time no VIV is introduced to the system which improves the performance of the observer since the response of the approximate model is now more like VIVID. The best performance is reached when low angular and acceleration process noise is used and high force noise is used.

5-5-2 Varying measurement frequency

In theory lower measurements frequencies can be used since the natural frequencies that are of interest are all below $1Hz$. To avoid aliasing the sampling frequency of the sensors has to be at least twice the frequency of the lowest observed frequency, which means accurate results should still be possible when a sampling frequency of $2Hz$ is used.
It can be concluded that a high update frequency can improve the results, but no definitive conclusion can be drawn about using lowering the measurement frequency. More research should be done on varying the measurement frequency.

5-5-3 Biased sensors

The bias in the sensors had less influence on the system performance than was anticipated for. It is still believed that biased sensors can have a negative influence on the performance of the observer. Running more checks is advised, be it with a different way of varying the bias per sensor.

Chapter 6

Filtered performance and improvement

In the previous chapter the sensitivities of the Kalman Filter (KF) were checked. It was found that by using a low amount of process noise on the angles and accelerations and a high amount of process noise on the forces the best results was obtained. In this chapter this results is compared to the results of the approximate model, without the KF.
After the results are compared, a system with a different setup is tested and it is checked whether this setup improves the results.

6-1 Filtered performance

To check the results of the improvement the KF makes to the approximate model the Kalman filtered system is compared to the approximate model and the VIVID simulations. For the comparison the simulations that gave the best in the previous chapter is used. It was seen that this was the case when low angle and acceleration process noise and high force process noise was used. The results for the KF system exited by constant current and Vortex Induced Vibrations (VIV) and the results for the system exited by varying current are compared to the results of the approximate model in this section. In the simulations of the approximate model no noise is added to the input force. Having an input not at all disturbed by noise is not realistic, but this way the performance of the approximate model can be checked without unknown influence. It is expected that adding noise decreases the performance of the approximate model.

6-1-1 Constant current and vortex induced vibrations

The first results is that of the Vertical Transport System (VTS) exited by a constant current. In figure 6-1 the deflection of the tip of the system calculated by VIVID, the approximate Kalman filtered system and the approximate model is seen.

In this simulation the improvement made by the KF is large. The approximate model does not include VIV and therefore it is not influenced by the in-line increased drag effect created

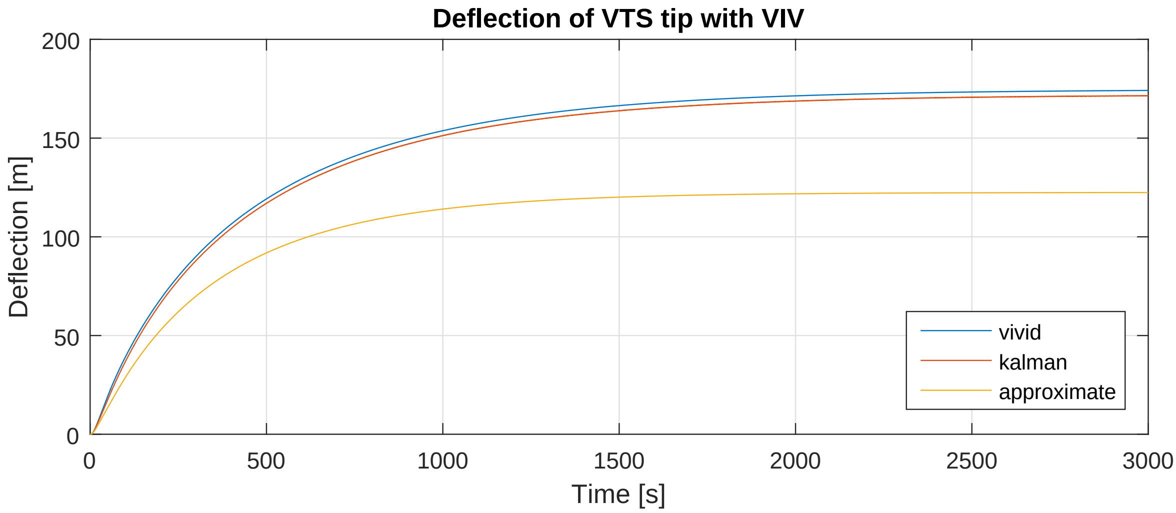

Figure 6-1: Constant current result

by VIV. This results in a simulation with a final deflection of 122.43m, which is 51.70m less than the final deflection of the VIVID simulation. The KF system compensates for this behaviour and obtains a final deflection of 171.44m which reduces the final offset between the model and the VIVID simulation by 49.01m and leaves an offset of only 2.69m.
This observation is important because it shows that the KF is able to compensate for effects that are not included in the approximate model and that occur over the entire length of the riser, while measurements are only performed at a few sections along the riser.

6-1-2 Varying current

The second result checked in this section are the deflections of the tip of the riser with a varying current, without VIV. In figure 6-2 the deflections of the simulation from VIVID, the deflections generated by the approximate model without a KF and the deflections of the system with a KF are compared.

In this figure improvement is seen as well. A first improvement that is visually confirmed is that the offsets of the KF system compared to the VIVID simulation are smaller than the offsets of the VIVID simulation compared to the approximate model. This is confirmed by the mean error calculated at three time intervals where the deflections vary slowly. These are important time intervals since the full system will be travelling at a constant speed for most of the time. Interval one ranges from 2000s to 3000s, interval two ranges from 4000s to 5000s and interval three ranges from 7500s to 9000s. The mean error is calculated by taking the difference between the observer signal and the reference signal, summing all of the differences and dividing by the amount of samples, results are found in table 6-1.

Interval time	2000s - 3000s	4000s - 5000s	7500s - 9000s
Kalman	1.259	0.646	1.566
Approximate	1.530	0.858	1.698

Table 6-1: Mean offset at three time intervals

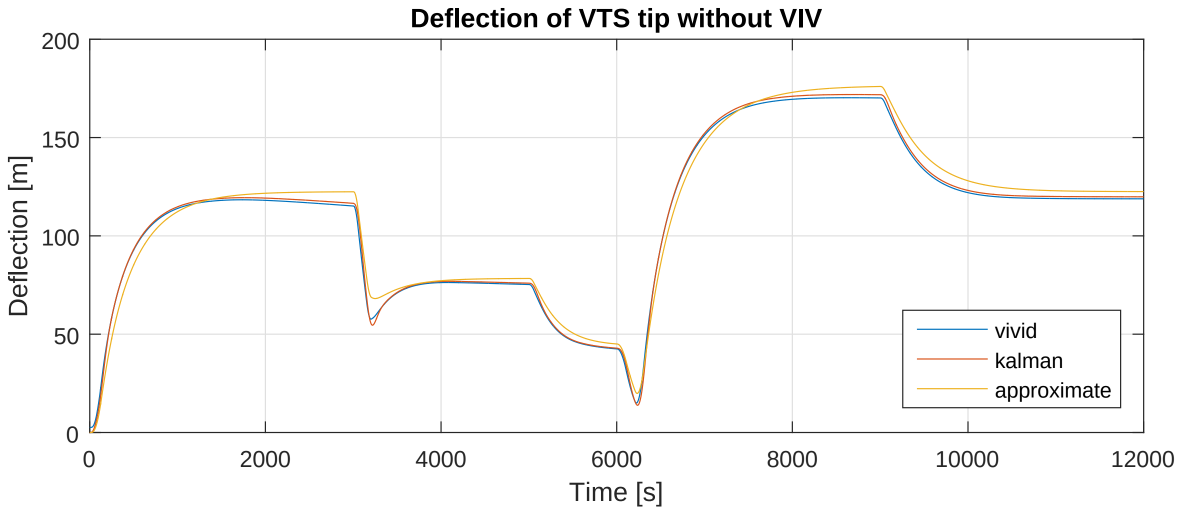

Figure 6-2: Varying current result

Next to the decreased steady state offset one of the most important improvements that is seen is the change in behaviour of the system with a KF. After almost 3000 seconds it can be seen that the simulation generated by VIVID is slowly decreasing in deflection, but the approximate model does not vary in total deflection at this point. This creates an offset in tip deflection that increases slowly. When combined with a KF the model is able to track the positions of the VTS created by VIVID with a constant offset, which is an important improvement.

6-2 Improvement

As seen in previously obtained results steady state error occurs which cannot be filtered out. In order to improve on this behaviour, a compromise is made between costs and the effectiveness of the model. As explained before position measurements done from the Mining Support Vessel (MSV) are inaccurate and it is too expensive to constantly add position measurements using beacons on the sea floor, because this way a lot of beacons are required. The compromise is that beacons are used at the seabed at a few fixed locations, so that the position of the tip of the VTS can be measured when close to these locations. When harvesting nodules the Seafloor Mining Tool (SMT) and the MSV create parallel lanes that have a small width but are tens of kilometres long. Positions measurements are added at the end of each lane, where the MSV and the SMT turn around. The goal of these added measurements is to create a state which in which the static offset is minimized. Since in the previous chapter is was found that after the observations reach a steady state the remaining motions were minimal, it is expected that the observations deviate little from the steady state reached with added position measurements. This should result in better observations over a longer period.

6-2-1 Varying observations

In order to include the position references the observer is expanded and four extra measurements are added. Two position measurements at the top and bottom of the clump weight, and two position measurements at the top and bottom of the first booster station above the clump weight. When the position measurements are added to the observations, this increases the amount of states used in the observations. There are two ways this problem can be mitigated.
The first way is by always including the position measurements in the observer. This creates a problems when the position measurements stop, because then the measurement vector z_k either is filled with zeros for the position measurements, or with the last position measured. This creates a large offset when the relative flow velocity changes and can lead to an increased error when the position is not measured. A way to solve this problem is to alter the process covariance matrix Q and introduce a large position covariance when the positions are not measured. This results in a decreased measurement dependency which is desired when the measurements are absent. An unwanted effect is that this also leads to an increasing error covariance in the error covariance matrix, which can become unstable. (Liu and Goldsmith, 2004)
A second way to add the position measurements to the system is again to add the extra states to the observer, but this time also introduce an extra term d_i. This term is introduced in (McLauchlan and Murray, 1993) and it simply varies between 0 and 1, $d_i = 1$ if the state is observed and $d_i = 0$ is the state is not observed. The state is not observed when there are no measurements. Using this technique the process covariance is not altered to extreme values which results in a more stable system.
The error covariance matrix P_0 was set equal to Q in the previous chapters and this resulted in a converging system. It is assumed the error covariance matrix will converge again. The error covariance matrix is not altered at the switching moments when states are excluded or included.

6-2-2 Noise and covariance

Noise is added to the position measurements. This added noise also causes a variation in the process noise used in the observer and the process covariance matrix.

Noise

The noise values used to create the noisy measurements for the observer is found in table 6-2. Just like in the previous chapter the noise introduced in the measurements is also used to observe the influence of process noise. Position noise is, just like the noise introduced in the angles, added to the states included in the $\hat{x}_k$ vector. In the previous chapter noise for every state in the $\hat{x}_k$ vector was the same, but in this case noise varies for the angles and positions.

The values used to vary the noise are found in table 6-2. Just like in the previous chapter each case gets its name from the amount of process noise per case. In order to determine the sensitivity of the KF to the process noise the amount of process noise the noise is varied. An extra check is added in simulation 4 which is explained in the following subsubsection.

Simulation case	Position noise $[m]$
low pos.	$0.2 \cdot 10^{-1}$
equal pos.	$0.2 \cdot 10^{0}$
high pos.	$0.2 \cdot 10^{1}$

Table 6-2: Noise variations for added position simulations

Covariance

The process covariance is varied along with the noise just like in the previous chapter. So the only the diagonal of the process covariance matrix has non-zero entries that are equal to the squared values used for the noise. Other than in the previous chapter, in this case two separate covariance matrices have been used. A switch is made between the covariance matrices depending on whether positions are measured or not.
When position measurements are added all diagonal position variances, part of state $\hat{x}_k$, are equal to the squared amount of noise of which the values are found in table 6-2. After position tracking is lost, the position calculating states in the observer are set to zero and the process covariance matrix diagonal entries for state $\hat{x}_k$ are all equal to the angle noise variance values again.

6-2-3 Results

All four simulations are now run using the model and observer as described in **??**. Positions measurements are added to the system twice. The first position measurements are added from start up and they are added for 1000 seconds, after this timespan position measurements are removed from the system. They are added again at 5800 seconds and again are added for 1000 seconds. A timespan of 1000 seconds is chosen because in this timespan a large part of the start up behaviour occurs, but a steady state is not fully reached. This creates a case where it is checked if the steady state can be observed more accurately when part of the start up behaviour is observed with greater accuracy.
The results of the variation of the tip deflection are plotted in the following figure, figure 6-3.

It is clearly visible when position measurements are present. The observations that start after 5800 second cause a jump in the deflection of the tip of the VTS. Between different amounts of noise no variations are seen from this figure. The Root Mean Square Error (RMSE) and the Variance Accounted For (VAF) are compared in the following table, table 6-3.

Simulation case	RMSE $[m]$	VAF $[\%]$
low pos.	1.3334	99.96
equal pos.	1.3332	99.96
high pos.	1.3328	99.96

Table 6-3: RMSE and VAF for $12000s$ simulations with added position measurements

Increasing the amount of process noise does seem to have a positive effect on performance of the observer. The overall RMSE of the observations compared to the original signal decreases when compared to the RMSE of the system without added position measurements.

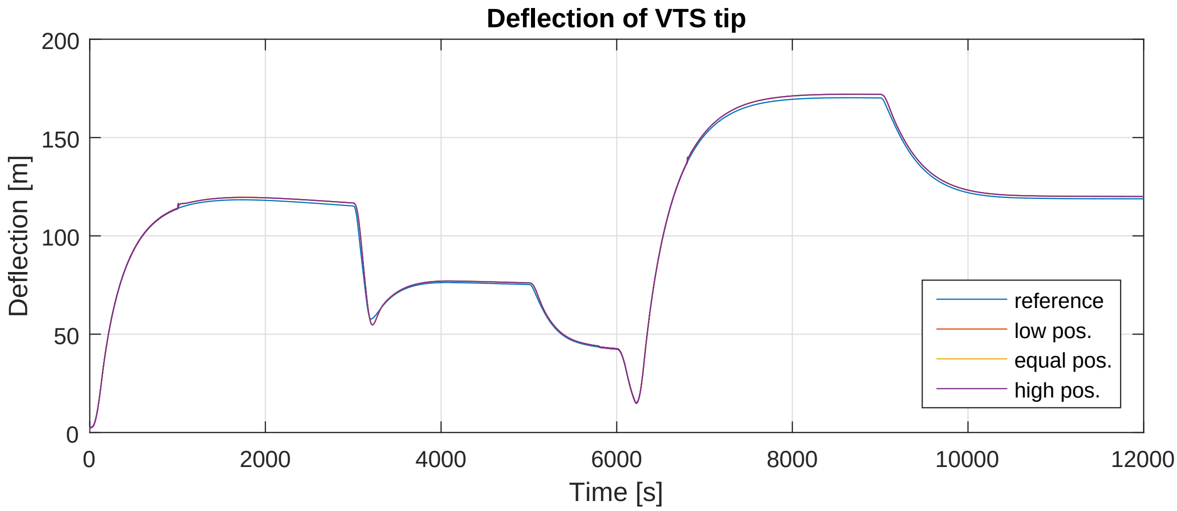

Figure 6-3: Riser simulation 12000s including positions

This decrease is partly explained by the decreased offset when the position measurements are added, but it is interesting to see if the decreased RMSE offset is also decreased in the steady state situations. If the error at the steady state is reduced by temporarily adding measurements this means that temporary positions measurements has an positive effect on the entire simulations. The best observation is made when the process noise covariance is set to a high value. For this simulation the mean error at steady state is calculated.

Simulation case	$2000s$ - $3000s$	$4000s$ - $5000s$	$7500s$ - $9000s$
low low high	1.259	0.646	1.566
high pos.	1.419	0.805	1.726

Table 6-4: Mean offset at three intervals for simulations with added position measurements

The mean values for both time intervals are found in table 6-4. Contrary to what was expected adding position measurements does not decrease the mean offset at a steady state. An explanation for this behaviour can be that positions measurements on the riser are only added at four point, while the positions are calculated at almost sixty points. Adding some position data can force these points to move, but it does not influence the rest of the riser behaviour, which still wants to obtain the same shape as it took without the position measurements. When the position measurements are removed the observed positions are swung back to where the approximate model estimates where they should be without position measurements. The increased offset at steady state can be explained as an effect introduced by the rapid motions that are observed shortly after the position measurements are removed.

6-3 Conclusion

In this section conclusions are drawn about results of the approximate model combined with the KF and about the improvements made to the observer.

6-3-1 Filtered performance

From the comparison of the deflection obtained it is seen that using the KF combined with the approximate model improves the result from the approximate model. The increased deflection caused by VIV can almost be filtered out completely. From the comparison with a varying current is it seen that the KF improves the behaviour of the approximate model. An offset is kept that is not filtered out, but the addition of the KF reduces the offset and it keeps the offset stable.

6-3-2 Improvement

When position measurements are added a clear improvement in the tracking capability of the system is seen. This improvement is only temporary and the system falls back in the same shape as was the case with the simulations without added position measurements. In the steady state it is observed that the system provides less accurate results compared to a system without added position measurements. The observations remain stable when a switch is made between a system with position measurements and without position measurements.

Chapter 7

Conclusions

The goal of this thesis was to create a system that can observe the motions of the tip of the Vertical Transport System (VTS) using limited measurements. Also the system should be able to run in real time. A two dimensional representation of the system was made and combined with a Kalman Filter (KF) so measurements and model estimates can be combined. In this chapter conclusions are summarized and discussed.

7-1 Conclusions about the approximate model

From the validations done in chapter 3 the approximate model appears to work as expected. The static cases coincide with well known analytical solutions The dynamic behaviour is verified by comparing with (Currie and Cleghorn, 1988), from with results from were validated by experiments. It is seen that there are some errors and they increase with increasing modes, but since lower modes are of most interest this does not create problems.

Overall the model performs like would be expected. The clump weight at the end of the riser tensions the model and its increased mass combined with a diameter equal to that of the rest of the booster stations make that is moves slower than the rest of the riser. This also goes for the rest of the booster stations, who all lag behind when current is introduced from standstill as seen in appendix F. The riser takes on a shape is logical, with a maximum deflection around $120m$ and a top angle lower than one degree.
The natural frequencies differ from the riser design tool, compared in section 3-4, which indicates that there are differences in the stiffness and inertia matrices of the model. Since there is a difference in tension, this is explained because tension is modelled as added geometric stiffness. The difference in tension force is explained because VIVID makes use of the effective tension, which was described in section 2-5-3. Whether this effect fully explains the differences between the tension forces is not checked.

The systems runs in more than real time. Observing 12000 seconds of simulation data takes around 2.1 hours. This is done on a laptop that is over 7 years old, with 2 cores which both run at $2.8GHz$. Only one core is used to perform the Matlab calculations. Matlab is known to be a programming language that is not optimal when runtime has to be minimized so a different programming language can speed up the observer significantly. Also using better hardware will lower the calculation time.

7-2 Conclusions about the Kalman filter

The KF is introduced so the approximate model can be combined with measurements. This is done to reduce the offset of the approximate model compared to VIVID. From the results in section 6-1 it is seen that the KF performs well. The average offset is reduced and the model behaviour is gets adjusted so the system behaves more like the simulation results from VIVID. The lack of Vortex Induced Vibrations (VIV) in the approximate model is for a large part mitigated by the KF. After combining the approximate model with the measurements in the KF it was seen a big portion of this error was filtered out and the offset in steady state is reduced by 49.01m which is almost 29% of the total deflection.

In section 4-3 it was seen that the system is not fully observable. This means that the system is not able to recreate its initial states through its outputs. Whether the rank of observability matrix of the system really is equal to two is up for discussion because all of the singular values are far above zero. A low estimation by the Matlab function can be explained by numerical errors introduced by the large number of Degrees Of Freedom (DOFs) in the system. The system does appear to be fully detectable. This is shown in subsection 4-3-2 and this is confirmed by the convergence of the observations is section D-1 and also by the long term simulations from chapter 5.

That the system is not observable can also be seen from the steady state results. In steady state is can be seen that an offset remains between the VIVID simulation and the observer that is not filtered out by the observer. This can be explained by the type of measurements that are being done. As was seen in subsection D-1-1, the measurements are observed well and stable. When riser goes to a steady state the acceleration measurements approach zero which causes the riser to come to a standstill.

The force adaptive KF appears to works well. From the test cases in chapter 5 it is seen that the KF works best when a large process covariance is used for the force. The force used in the system is fully dependent on the performance of the KF, so when the force process covariance is chosen lower than the force measurement covariance constant the force varies little. This is not desired when variations in current are present that introduce large force fluctuations.

7-3 Sensitivities

With the riser excited by a constant current and VIV the observer performed well. The fit that is achieved is close and in steady-state the error between the observer deflection and original system deflection is small compared to the total deflections.

When the VTS is exited by a varying current similar results are achieved as was the case with a constant current. This time no VIV are introduced to the system which improves the performance of the observer since the approximate model is now more like VIVID. This increased performance is seen in the calculated Root Mean Square Error (RMSE) and Variance Accounted For (VAF). Large differences are seen when the process noise is varied but the optimal performance is reached when the observer setting are comparable to the settings used in the constant relative flow case.

It is found that the system performs best when low process noise is used on the accelerations. Jumpy force observations from appendix D did not results in noisy tip motions in the observer. This is because the variations of the force measured at the tip are relatively small compared to the total value of the force.

Increasing the amount of measurements per second processed by the KF did not have a consequent effect. Like expected, the accuracy of the observation increased when the measurement frequency was increased, but unexpected is also did when the measurement frequency was decreased. More research should be done to explain this effect.

Adding a bias to the measurements did not influence the behaviour of the observer much. This is most likely explained by the way that the tests were done, in which the rest of the sensors does not have a bias. Overall adding a bias to any of the sensor types did have a negative effect. It is still believed that biased sensors can have a very negative influence on the performance of the observer when al sensors types become biased.

7-4 Improvement

Adding position measurements to obtain a lower steady state error was counter productive. Through the added position measurements improvement are made when the observation are added, but this improvement disappears when the added measurements are removed. It is seen that the observer remains stable when a switch is made between a system with position measurements and without position measurements.

7-5 Discussion

At the start of the thesis a set of research questions was proposed. It is now discussed whether these have been answered to full satisfaction.

How can the position of the clump-weight of the VTS be monitored using limited observation points?
In monitoring the position of the clump weight of the riser a trade off has been made. When all the possibilities are compared it is found that a lot of conventional methods are not accurate enough. The most accurate method to track the position of the clump weight would be using an array of beacons placed at the seabed, but this is where a decision has to be made between accuracy and cost. Since such an array would require a large amount of beacons that often need to change position this solution is not desirable. By creating a model and combining this with measurement data a solution is found that can more cost effective. Because the solution offered in this thesis is less accurate bigger error margins have to be used which results in a less effective mining pattern.
Strictly speaking this thesis does not offer a full solution since not all of the states of the system are observable. By using an approximate model and an observer that is detectable but not fully observable the positions can only be approached and not fully observed. Whether this observation is good enough to result in a more profitable system compared to an extensive seabed array solution should be studied.

What can be measured at the booster stations?
At the booster stations angles, accelerations and relative velocities are measured. In monitoring applications another sensor that is commonly used is the strain sensor. In this thesis the strain sensor has not been used for two reasons. Reason number one is that strains can only be measured at the booster stations and it is expected that the strains directly at the top and bottom of the booster stations show large fluctuations because the booster stations have much higher masses and inertia than the rest of the sections and are therefore not representative for the stresses and strains in the rest of the system. The second reason is that when the riser reaches a steady state a constant strain is measured and from this measurements, much like the acceleration measurements, no more information can be achieved. By measuring the strain on both sides of the booster station the curvature of the riser at that point can be determined, but this will also approach zero at most points in the system in steady state, as seen in appendix D.
The quality of the measurements is up for discussion. From papers and specification sheets provided by manufacturers it was found that nowadays highly accurate sensors can be produced that deliver accurate data with low noise levels. It is not sure if this high accuracy can actually be reached in the deep sea mining system, none of the sensors have been tested by IHC and specifications delivered by manufacturers are probably created in laboratory environments with highly stable input signals.

How accurate is an approximate model compared to real data?
Since no real world data is of riser behaviour in a deep sea mining system is available the approximate model was compared to a design riser tool which gave good results. Also verification of the approximate model gave good results, for both the static and dynamic cases. Analytical formulas used in the static validations have been tested and validated many times, the results from (Currie and Cleghorn, 1988) are confirmed by experiments. It has to be kept in mind that the tensioned system that is being tested in the paper is smaller than the VTS which the approximate model is designed for and that the lowest natural frequency measured in the paper is a factor $1 \cdot 10^5$ larger than the lowest natural frequency of the VTS. That

being said the approximate model in an altered setup was able to recreate the low natural frequencies for all of the cases described in the paper.

How accurate can an approximate model combined with a Kalman filter track the position of the tip of the riser?
The simulations generated by VIVID can be tracked within meters but a steady state offset is not filtered out. This result is dependent on the accuracy of the approximate model. The steady state error that cannot be filtered out is expected to decrease when the model that is used to create estimations and observations is more alike the system that generates the measurements. Even when the models are more alike it is expected that an offset remains since the system in its current setup is not fully observable. This is caused by the type of measurements that are performed.

Chapter 8

Recommendations

This chapter contains recommendations for future work, both for the TU and the sponsor Royal IHC.

8-1 Future research

What is recommended for future research.

8-1-1 Improve approximate model

Improving the accuracy of the approximate model creates more accurate results. From chapter 5 it is seen that the Kalman Filter (KF) can improve the position estimation, but when a steady state is reached an offset of more than a metre is not filtered out. This is because the filter is not observable, so it cannot reproduce all of the states of the system. When the approximate model is more like the system it observes this constant error can be minimized. A trade-off still has to be made between approximate model accuracy and the computational power required for the model to run in real time. Combining the approximate model with a KF is still be necessary to account for unknown external influences.

8-1-2 Alternative filters

There are different forms of the KF and only the linear KF is used in this thesis. Although this led to acceptable results the results might improve further when an alternative KF is used. Some examples of alternative filters are the Extended Kalman Filter (EKF), the Unscented Kalman Filter (UKF) and the Ensemble Kalman Filter (EnKF). The EKF and the UKF are Kalman filters that are designed to handle non-linear problems. Using one of these filters can make it possible to calculate the external drag force in the KF model as well, instead of just obtaining it from measurements. This could improve the response time of the observer.

Another case where an alternative Kalman filter can be of use is in the system with added positions measurements. It is now seen that the position observations quickly lose the improved results when the added positions observations stop. This is because the rest of the riser is still very much dependent on the approximate model. After the position observations stop the system quickly goes back to the same state it also took when no position measurement were added at all. If a KF variant is implemented that can edit system parameters, this can be used to alter the behaviour of the approximate model, for example by lowering or increasing the modelled stiffness. This way the behaviour of the entire system is altered creating better results when the position measurements end.

8-1-3 Model validation

Validating the performance of the system by comparing it to real world measurement data is also recommended. The model should be expanded to include at least the motions in three dimensions, x, y and z. Alternatively a test setup can be created that constraints the motions to only so that the observed model only moves in two dimensions. It is recommended to use a system that moves with very low natural frequencies, like a thin rod or a lightly tensioned string. A system like this is more likely to a shape similar to that of the riser.

8-1-4 Increase dimensions

The approximate model should be expanded to include motions in all dimensions so axial movement, torsion and movement in the y-direction can be observed. Additional dimensions make the system larger and will make it run slower. Adding these dimensions is important though since the twisting and turning of the riser will have an influence on the measurements. When one of the booster stations is twisted by 90° an accelerometer that is supposed to perform measurements in the x-direction is useless. By adding dimensions to the approximate model rotations in the riser can be observed in the same way as positions are observed using a KF. If the orientation of the sensors are known inaccuracies caused by torsion can be mitigated.

8-1-5 Sensor accuracy

One of the biggest influences on the performance of the system in a real world test setting will be the accuracy that can be obtained by the sensors. All of the sensor specifications are now either obtained from manufacturer specification sheets or based on information from manufacturer specification sheets. It is likely that the specifications for the sensors are derived in ideal conditions for the sensors. Testing sensor performance can be done in a normal, but slowly varying environment. It is not necessary to test the sensors at a large depth since a sensor can be encased in a pressure and water resistant housing when attached to the riser.

8-1-6 Sensor distribution

Capturing as much data as possible with limited amounts of sensors can be a challenge. In (Natarajan et al., 2006) a study is done on how sensors along a deep sea riser can be placed optimally in order to capture as much information as possible on Vortex Induced Vibrations (VIV). It was found that by creating a few clusters of sensors good results could be achieved. A same study should be done for this case in order to determine optimal positions for the sensors. During this thesis the locations where sensors can be placed is restricted to the booster stations, but more accurate results might be obtained by using sensors in different locations. The additional costs of adding sensors away from the booster stations can be compared to the additional profit that results from increased accuracy. This study can be easily validated by varying the measurement location inputs to the system with a KF created in this thesis.

8-1-7 Process noise covariance

As found in chapter 5 varying the process noise influences the accuracy of the fit of the approximate model combined with a KF compared to the VIVID results. For now only the effect of varying the process noise has been researched. It is recommended to optimize process noise covariance by performing more iterations. Also the effect of varying the off-diagonal entries in the process covariance matrix should be researched. The process noise non-diagonals link different states to each other. Connections between the different states, for example force and accelerations, do influence each other and this can be included in the process covariance matrix.

8-1-8 Influence of waves

The effect of the waves at the top of the ship has been simplified. Motions at the top of the ship are assumed to create an imposed motion at the top of the Vertical Transport System (VTS). When the full system is studied the effect of the VTS should on the motions of the ship be taken into account as well. Rough seas will create added current and inertia forces at the top of the VTS, which might excite the riser much more than has been assumed so far. Also the effect of heave should be studied. In this thesis it is assumed heave can be fully mitigated by the gimball al the top of the system. As soon as this is no longer the case, for example in extreme waves, the ship can pull or push on the riser and increase or decrease the tension effect created by the clump weight. Variations in the tension create a variation in the stiffness of the system which directly effect the total deflection of the system.

8-2 Royal IHC

What is recommended for the sponsor of this thesis, Royal IHC.

8-2-1 Cost effectiveness

For Royal IHC an important recommendation is to observe the maximum allowable error of the system. The accuracy that can now be achieved at steady state varies around 1.5 meters and when a safety factor is used this inaccuray becomes larger. If a mining pattern is used that creates long stretches it should be avoided that these stretches overlap since all nodules are harvested in one sweep. So in order to avoid overlapping mining activities a margin is necessary. This margin creates an area that is not mined and results in an inefficient mining operation. Whether the observations are accurate enough to result in a profitable system should be economically studied.

Appendix A

Newmark beta numerical solver

To solve the dynamic response of the system a discrete time solver is used, the derivation and verification of the method is done in this chapter.

A-1 Newmark-beta numerical solver

To solve the Ordinary Differential Equation (ODE)s that form the structural dynamic system that makes up the approximate model a solver is implemented. Matlab contains multiple functions which are commonly used to solve ODEs. All of the standard solvers in Matlab use a variable time step which can result in a large computational time. This high computational time is caused by high frequency components in the system which require a small time step in order to solve them accurately. In this thesis the high frequency motions are of little interest since they do not contribute to the large motions of the Vertical Transport System (VTS). Therefore, in order to speed up computations, a Newmark-beta method is implemented that is run using a fixed time step.

A-1-1 Derivation

The Newmark-beta method (Newmark, 1959) used in this thesis is implicit, which means a solution at $t = t + \Delta t$ is obtained by solving a set of linear equations. If $\beta = 1/4$ and $\gamma = 1/2$ are used the accelerations over time step dt is assumed constant and the method is stable for any chosen time step dt. While the time step does not influence the stability of the solution, it does influence the accuracy of the solution. A large time step reduces computational time but is not able to capture high frequency vibrations accurately. Setting on a time step is done in the next subsection. The finite difference equations for the Newmark-beta method are

$$x_{i+1} \approx x_i + dt\dot{x}_i + dt^2 \left[\left(\frac{1}{2} - \beta \right) \ddot{x}_i + \beta \ddot{x}_{i+1} \right] \tag{A-1}$$

and

$$\dot{x}_{i+1} \approx \dot{x}_i + dt\left[(1-\gamma)\,\ddot{x}_i + \gamma\ddot{x}_{i+1}\right] \tag{A-2}$$

At $t = 0$, x, $\dot{x}$ and $\ddot{x}$ are the initial conditions conditions of the system. The finite difference relationships in terms of the increments of displacement

$$\delta\ddot{x}_i = \frac{1}{\beta dt^2}\delta x_i - \frac{1}{\beta dt}\dot{x}_i - \frac{1}{2\beta}\ddot{x}_i \tag{A-3}$$

$$\delta\dot{x}_i = \frac{\gamma}{\beta dt}\delta x_i - \frac{\gamma}{\beta}\dot{x}_i + dt\left(1 - \frac{\gamma}{2\beta}\ddot{x}_i\right) \tag{A-4}$$

In these equations δx_i is the only unknown. The incremental equilibrium for the system over time step dt is written as

$$M\delta\ddot{x}_i + C\delta\dot{x}_i + K\delta x_i = \delta f_i^e \tag{A-5}$$

In this equation δf_i^e is the variation of the external force over a time step dt. By substituting equations A-3 and A-4 into equation A-5 an expression for δx is found. This result is used in equation A-3 to calculate $\ddot{x}_i$. The acceleration at step $i+1$ is calculated by $\ddot{x}_{i+1} = \ddot{x}_i + \delta\ddot{x}_i$. Using the acceleration at $i+1$ in the finite difference equations A-1 and A-2 x_{i+1} and $\dot{x}_{i+1}$ can be determined. This method can be implemented for both Single Degree Of Freedom (SDOF) as well as Multiple Degrees Of Freedom (MDOF) systems, in the case of an MDOF system constants M, C and K become matrices of size $n \times n$ and x becomes a vector $\bar{x}$ sized $n \times 1$.

A-1-2 Verification

To verify the equations as they are used in the Matlab code a system with three Degrees Of Freedom (DOFs) is set up. Because the system contains only a few DOFs it can be easily implemented and solved by using a standard Matlab ODE solver, the ODE45 function. The system that is tested is a mass-spring-damper system of which the parameters are found in table **??**. A simple representation of the system is seen in figure A-1. Results generated by the build in Matlab ODE45 function are compared to that of the Newmark-beta solver.

Node	**M** $[kg]$	**C** $[Ns/m]$	**K** $[N/m]$
1	8	0.02	30
2	4	0.02	40
3	0.5	0.02	50

Table A-1: Parameters mass-spring-damper system

The parameters from table A-1 are chosen so that a range of natural frequencies is obtained. Natural frequencies are found to be $0.23Hz$, $0.62Hz$ and $1.70Hz$. An excitation force is introduced as a sine function, given as $F(t) = 10 * sin(2\,\pi\,t/25)$, which has a period of 25 seconds, so it can be easily distinguished from the natural system vibrations. This force is places on the second mass, the other two masses are excited by the motions of the second

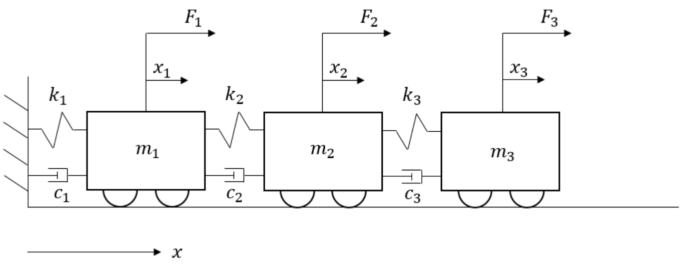

Figure A-1: 3 DOF mass-spring-damper system

mass. The total system is run for four times the excitation force time period, 100 seconds. The time step dt is varied in the following subsections. In order to obtain an accurate solution of the system, the time step should be chosen to be higher than the largest frequency that needs to be accurately simulated. All masses start at $\bar{x} = 0$, masses one and two start stationary, mass three has an initial velocity of $\dot{x}_3 = 5m/s$ For all time steps the system should converge.

Sampling at varying frequencies

Sampling is done at three different frequencies, $50Hz$ and $1Hz$. The sampling at $50Hz$ is a lot higher than the highest natural frequency and should create accurate results for every DOF. It is expected that the excitation force can be distinguished in both cases since the frequency of this force is much lower than the lowest sampling frequency.
The ODE solver function, 'ODE45', from Matlab is used as a comparison and its output sampling frequency is set at $50Hz$ to guarantee a smooth plot.

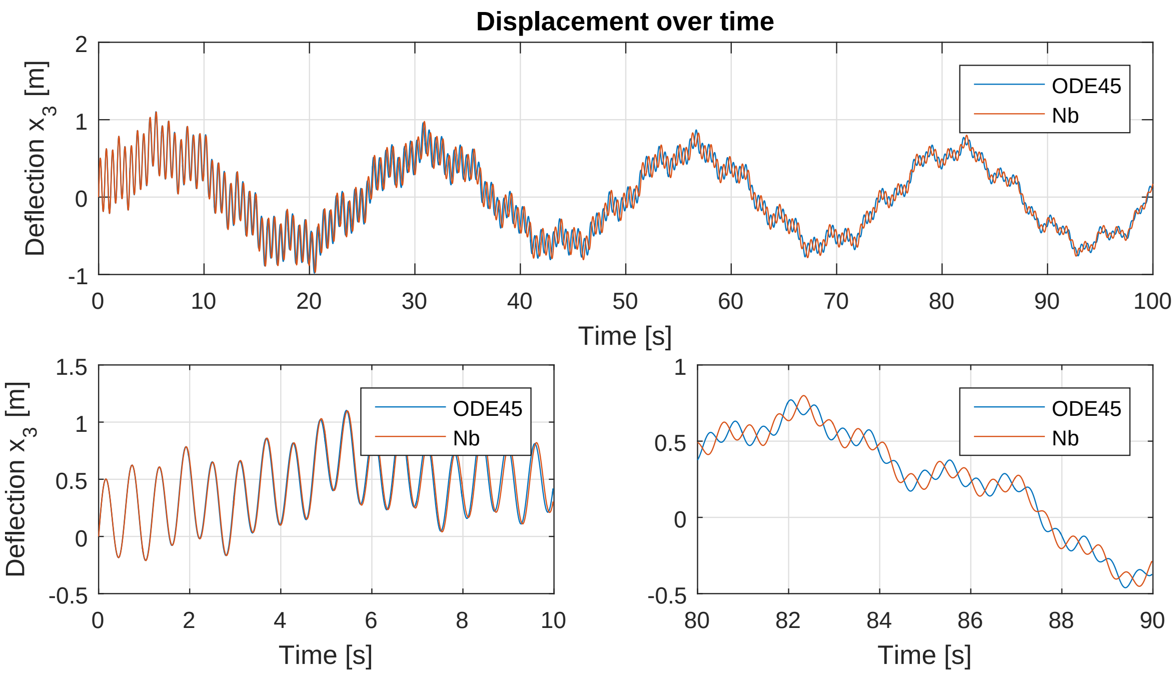

Figure A-2: Third DOF at $50Hz$ NB sampling

In A-2 the system is sampled at $50Hz$. The Newmark-beta solution produces the same results as the ODE45 function for the low frequency motions, but for the high frequency motions it is seen that a lag occurs and a phase error accumulates. This error is can be contributed to the assumption that accelerations are constant over every time step. To determine the influence of the lag is run without damping, so the motions do not decay over time, if damping is present the motions decay over time and the offset becomes smaller due to the decrease in total motions. Without damping figure A-4 is obtained in which the solution obtained with the Nb solution is subtracted from the ODE solution. It is seen that the offset does not increase and that it goes down after a maximum phase lag of 180 degrees is reached, indicating that the phase lag further increases. To check the assumption that the phase error is caused by the assumption of constant accelerations the system is also run with a sample frequency of $100Hz$. The phase error created using this sampling frequency is also plotted in figure A-4 and is seen to increase much slower. This is a logical result since the error created by assuming constant accelerations per time step becomes smaller when the time step becomes smaller.

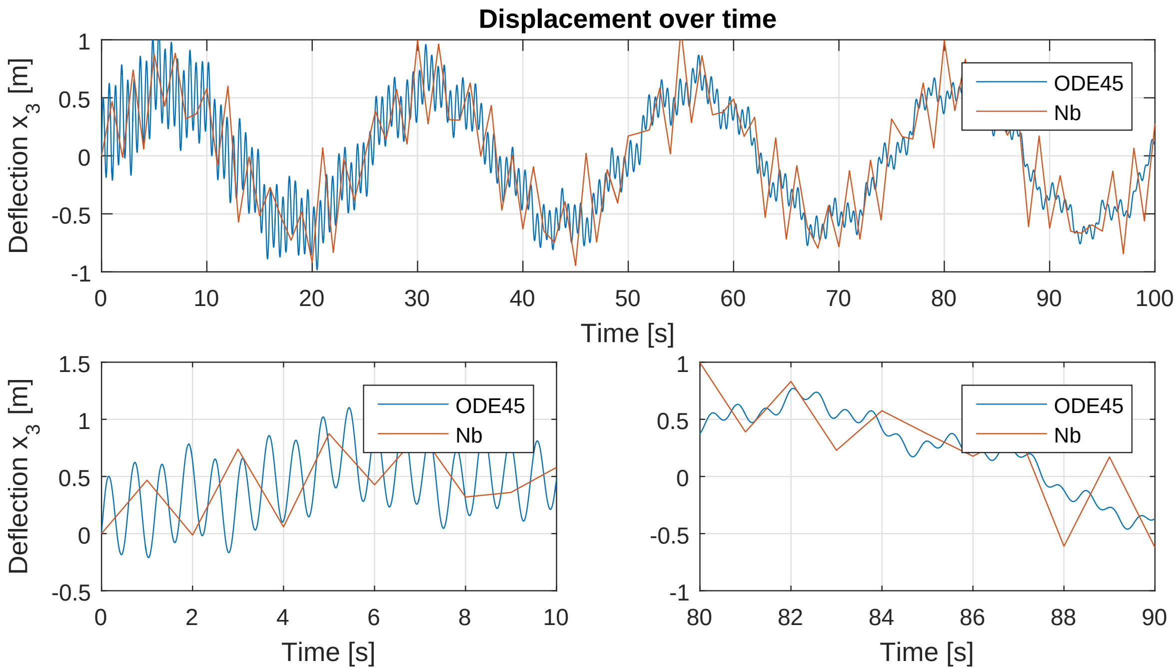

Figure A-3: Third DOF at $1Hz$ NB sampling

In figure A-3 a much larger time step of $1Hz$ is used. This causes large differences in the results because the system is no longer able to calculate motions of the highest natural frequency, which is under sampled. Also the motions of the other DOFs are not accurately tracked. Low frequency motions created by the varying force can still be clearly distinguished.
In all of the cases it is seen that the solver used to simulate the systems converges, as is to be expected of the Newmark-beta method as implemented. The solver works for both high and low frequencies, but it is observed that an error accumulates when the sampling frequency gets close to the natural frequency of a DOF of the system. It is found that even with a sampling frequency 30 times higher than the natural frequency of a DOF a 180 degrees phase lag is obtained after 75 seconds, which is within 120 cycles of the DOF with the highest natural

frequency. Even though the system lags, the amplitude of the motions does not increase as seen in figure A-4. It is also seen that when a sampling frequency is chosen close to or larger than a system natural frequency the motions of the system at that natural frequency cannot be obtained, but motions of the same system at a lower frequency are still accurately obtained. Based on the results from the simulations and the comparison with the ODE45 results from Matlab the Newmark beta method is assumed capable of solving structural dynamic systems. The time step used for the calculations has to be chosen low compared to the frequencies of interest so accurate results are obtained.

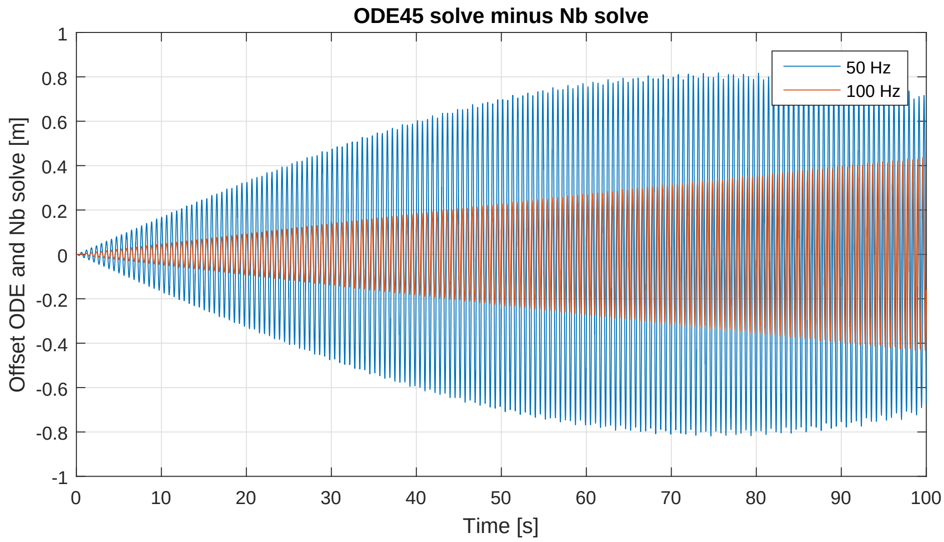

Figure A-4: Offset between NB solution and ODE solution at the third node when sampling at $50Hz$ and $H100z$

Appendix B

Approximate model verification

In this case the natural frequencies of a clamped-free beam will be extracted from the Finite Element Method (FEM) model and compared to an analytical solution, which can be found in books like (Thomson and Dahleh, 1998).

Natural frequencies of a clamped-free beam

The first case consists of the same hollow cylinder used in the hinged-hinged static case. For the Euler-Bernoulli beam equation 2-5 can be used. Distributed load $q(z,t)$ is set to zero so the following equation results.

$$EI\frac{\delta^4 w}{\delta z^4} + \rho A\frac{\delta^2 w}{\delta t^2} = 0 \tag{B-1}$$

The four boundary conditions of a clamped-free beam are now determined (Thomson and Dahleh, 1998). On the left hand side at the beam, at $z = 0$, the beam is clamped. This means the beam cannot move or rotate

$$w\left(z\right) = 0 \quad \left.\frac{dw}{dz}\right|_{z=0} = 0 \tag{B-2}$$

At the right hand side, at $z = L$, the beam is free. This means the beam can move and rotate, but the moment and shear force at $z = L$ are equal to zero

$$\left.\frac{d^2 w}{dz^2}\right|_{z=L} = 0 \quad \left.\frac{d^3 w}{dz^3}\right|_{z=L} = 0 \tag{B-3}$$

The general solution to equation B-1 is given by equation B-4 (Thomson and Dahleh, 1998).

$$W(z) = A\,\cosh(\beta\,z) + B\,\sinh(\beta\,z) + C\,\cos(\beta\,z) + D\,\sin(\beta\,z) \tag{B-4}$$

When the general solution is substituted into the boundary conditions, from equations B-2 it is easily found that

$$A + C = 0 \tag{B-5}$$

$$B\,\beta + D\,\beta = 0 \tag{B-6}$$

and from the right hand boundary conditions, with substitution of the solved left-hand boundary conditions

$$A\,\beta^2 \cosh(\beta\,L) + B\,\beta^2 \sinh(\beta\,L) + A\,\beta^2 \cos(\beta\,L) + B\,\beta^2 \sin(\beta\,L) = 0 \tag{B-7}$$

$$\beta^3\left(A1\;\sinh(\beta\,L) - A1\;\sin(\beta\,L) + B1\;\cosh(\beta\,L) + B1\;\cos(\beta\,L)\right) = 0 \tag{B-8}$$

When equation B-7 and B-8 are set equal to each other, the terms β^2 and β^3 can be excluded because β can not be equal to zero. After some rewriting it is found that

$$\cosh(\beta\,L)\cos(\beta\,L) + 1 = 0 \tag{B-9}$$

which can be written like

$$\cos(\beta\,L) = -\frac{1}{\cosh(\beta\,L)} \tag{B-10}$$

Equation B-10 can now be solved to find the values for $\beta\,L$. As can be seen from figure B-1 the amount of intersections is infinite, this is to be expected because a continuous system always has an infinite number of natural frequencies. In this thesis the focus will be on the lower natural frequencies, because those are the frequencies that are expected to contribute the most to the motions of Vertical Transport System (VTS). With the calculated values for $\beta\,L$, equation B-14 can be used to find the natural frequencies of the clamped-free beam. A solution is assumed in the following form

$$w(z,t) = W(z)e^{\omega t} \tag{B-11}$$

Using this solution a fourth order differential equation is obtained which can be written as

$$\frac{d^4y}{dx^4} - \beta^4 y = 0 \tag{B-12}$$

In this equation β is defined as

$$\beta^4 = \rho A\frac{\omega^2}{EI} \tag{B-13}$$

The natural frequencies of the beam can be found from B-13 when it is rewritten like

$$\omega_n = {\beta_n}^2\sqrt{\frac{EI}{\rho\,A}} = {\beta_n}^2 L^2\sqrt{\frac{EI}{\rho\,AL^4}} \tag{B-14}$$

The first few resulting natural frequencies can be found in table B-1, where the analytically found natural frequencies are compared to the frequencies found from the FEM model.

Finding the natural frequencies of the FEM model is done by taking an undamped system without any external forces. This way the system can be written like a Multiple Degrees Of Freedom (MDOF) system.

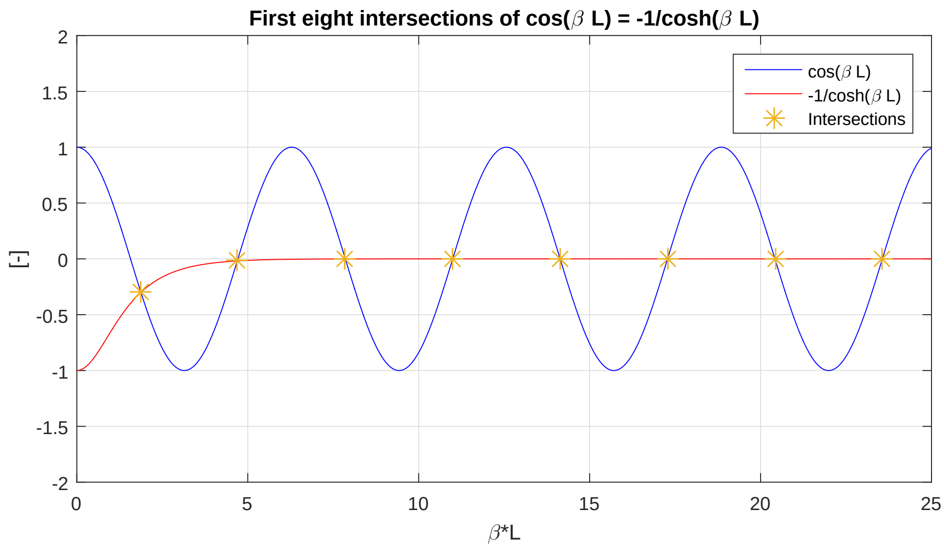

Figure B-1: Visualisation of equation B-10

$$\mathbf{M}\ddot{w}(z,t) + \mathbf{K}w(z,t) = 0 \tag{B-15}$$

The real part of the general solution to this equation is found as

$$w(t) = \sum_{i=1}^{N} \hat{X}_i \sin\left(\omega_i t + \phi_i\right) \tag{B-16}$$

In this equation N is the amount of Degrees Of Freedom (DOFs), ω_i are the natural frequencies. $\hat{X}_i$ are the eigenvectors multiplied with some unknown constant that depends on the initial conditions of the system and ϕ_i are phase angles that depend on the initial conditions of the system. Equation B-16 can be rewritten as a system of N linear equations

$$\left(-\omega_i^2 \mathbf{M} + \mathbf{K}\right) \hat{X}_i = 0 \tag{B-17}$$

From equation B-17 the natural frequencies can be derived by taking the determinant of $\left(-\omega_i^2 \mathbf{M} + \mathbf{K}\right) = 0$. The natural frequencies are found as the positive roots of this equation. In this case the natural frequencies have been derived using the Matlab function 'eig(K,M)'. This functions return the squared natural frequencies and the eigenvectors of the system. The first six natural frequencies of the clamped-free beam have been determined using a beam modelled as a hollow cylinder with the same specifications as the hollow cylinder used in the second case treated in subsection 3-2-1. Specifications of the beam used in this case can be found in table 3-2. For this case the beam in the FEM model has been divided into $3m$ long elements. The difference in natural frequency per node has been calculated by equation B-18.

$$difference = 100\% * \frac{\omega_{analytical} - \omega_{FEM}}{\omega_{analytical}} \tag{B-18}$$

Results have been summarized in the following table.

Mode	Analytic [ω]	FEM [ω]	Difference [%]
1	2.62	2.62	0.00
2	16.43	16.43	0.01
3	46.01	46.02	0.03
4	90.15	90.24	0.10
5	149.03	149.40	0.25
6	222.62	223.83	0.54
7	310.9	314.038	1.00

Table B-1: Natural frequencies of a 30m clamped-free beam solved both analytically and numerically

From table B-1 it can be seen that the analytically calculated natural frequencies come very close to the natural frequencies calculated from the FEM model. When the mode increases and the natural frequencies get larger the difference between the analytically and numerically found natural frequencies starts to increase rapidly.
The increasing difference in the calculated could be decreased by improving the accuracy of the FEM model. This can be done by increasing the amount of elements by decreasing the length per element. In this thesis it has been assumed that the natural frequencies from the lowest nodes will have the biggest influence on the results, therefore it is assumed that found difference will have very little influence on the end result. The accuracy of the model, influenced by the length of the chosen elements will have to be kept in mind in further simulations.
From the same table it can also be seen that all of the natural frequencies are positive and real which means the system is stable.

Appendix C

Signal fit

Calculation methods to compare the fit of signals.

C-1 Root Mean Square (RMS)

The RMS of a signal is a way to calculate the mean of the square root of a signal. It is calculated by equation C-1

$$x_{rms} = \sqrt{\frac{1}{n}\left(x_1^2 + x_2^2 + ... + x_n^2\right)} \tag{C-1}$$

The Root Mean Square Error (RMSE) is a way to compare two datasets, for example a dataset predicted by a model and the actual data. The RMSE can be calculated by equation C-2. Because the RMSE has the same units as the analysed data it can be easily interpreted.

$$x_{rmse} = \sqrt{\frac{1}{n}\left(\hat{x}_t^2 - x_t^2\right)} \tag{C-2}$$

In this equation $\hat{x}$ is the observed data and x is the original input data without noise contamination.

C-2 Variance Accounted For (VAF)

Another way to calculate the fit between an observer and the original data is to calculate the VAF. The VAF is used to determine the correctness of an observer by comparing the real output with the observer output and is calculated by equation C-3. (**?**) The VAF is calculated by taking the variance of the difference between the original signal and the signal created by the observer divided by the variance of the original signal. When two signals have a perfect fit the VAF will be 100%.

$$vaf = \left(1 - \frac{var\left(x - \hat{x}\right)}{var\left(x\right)}\right) \tag{C-3}$$

In the formula x is the original data without noise contamination and $\hat{x}$ is the observer data.

Appendix D

Force adaptive Kalman filter

In this chapter the ability of the Kalman Filter (KF) to observe measured angles, accelerations and forces is checked.

D-1 Validation

In this section the performance of the discrete system as well as the performance of the KF is tested. A comparison is made between the continuous and discrete state-space system in order to confirm that discretizing the system does not extremely influence its behaviour. Also it is checked whether the KF is stable and converges.

D-1-1 Force adaptive Kalman filter

To check whether the KF that is designed is stable, a simulation of the Vertical Transport System (VTS) is observed using the filter described in this section. The model used to generate the data is the same model that is used to build the observer. The initial conditions of the system that is being observer are the same as the initial conditions of the observer.

Creating measurement data

To create measurement data the non-linear approximate model from chapter 3 is run for $3000s$, which is roughly equal to fifteen times the period of the lowest natural frequency. At this point in time the speed at which the tip of the system moves varies very slowly and the system is assumed to have reached a steady-state, as explained in section 3-4. The model was run with a constant current of $0.5m/s$. Each section is divided into 10 elements, the booster stations are not divided and are simulated as one beam element each. This creates a system with 60 nodes and twice that amount of Degrees Of Freedom (DOFs). The inputs of the system used to generate the measurement data are contaminated with process noise. After creating the simulation data, the angles, accelerations and relative flow velocities are extracted at the top and bottom of each booster station. This simulation data are the measurements used in this section. The standard deviations of the sensor noise mentioned in subsection 2-1 are multiplied with a normally distributed white noise and are added to the measurements to create noisy measurements. The relative flow velocities velocities are put into the Morison equation to create force measurements influenced by noise.

Kalman filter setup

The observer is linearised and discretized as described in this chapter. All elements lengths, masses and stiffnesses are equal to that of the system used to generate the simulation data. In this section it is only validated that the KF converges and it is able to observe the measurement data. Standard deviations for the measurements can be found in section 2-1, standard deviations used in the process noise are found in the table below, table D-1.

Parameter	**Value**	**Unit**
Standard deviation model angles	$1 \cdot 10^{-4}$	rad
Standard deviation model accelerations	$1 \cdot 10^{-5}$	m/s^2
Standard deviation model forces	10	N

Table D-1: Standard deviation model

The standard deviations of the process noise are chosen by hand to be close to the standard deviation of the sensor noise.

Angles

The system is checked when starts with the same initial conditions as those that are used as an input to the KF. At the tip of the VTS, at the clump weight the angle is being measured. The variation of the angle over time can be seen in figure D-1.

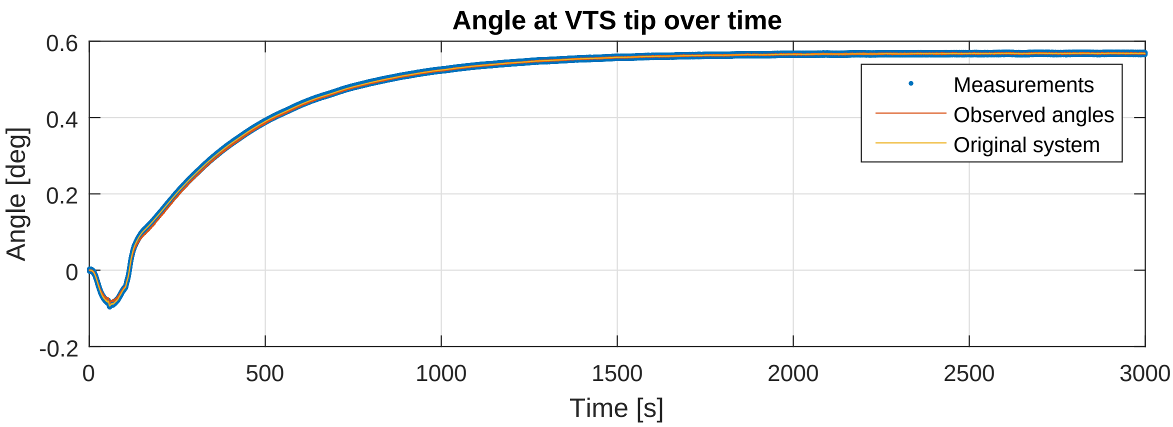

Figure D-1: Plot of angles

It is seen that the measurements, the observer angle and the actual angle from the original system only deviate very little. A closer look is taken in figures D-2 and D-3.

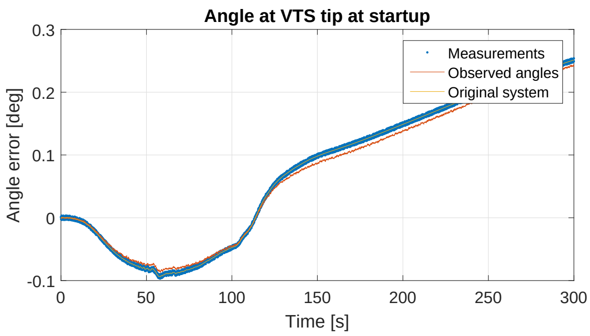

Figure D-2: Startup angles

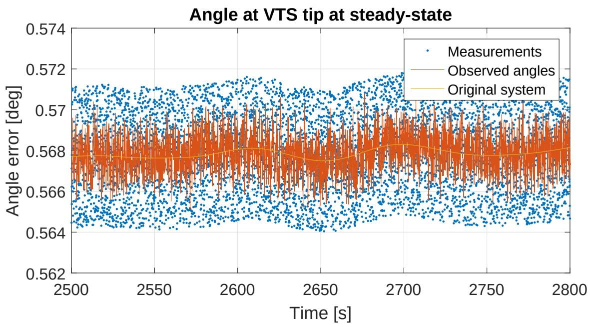

Figure D-3: Steady state angles

From figures these it can be seen that the filtered angles follow the measurements closely. At the start there is an offset between the original angles and the observed angles. This offset is confirmed by the simulation done in subsection 4-1-2 and is caused by the discretizing of the system. The discretizing causes the system to lag behind the original simulation. Using the current covariances the KF is not able to mitigate this offset until a steady-state is reached as seen in figure D-3.

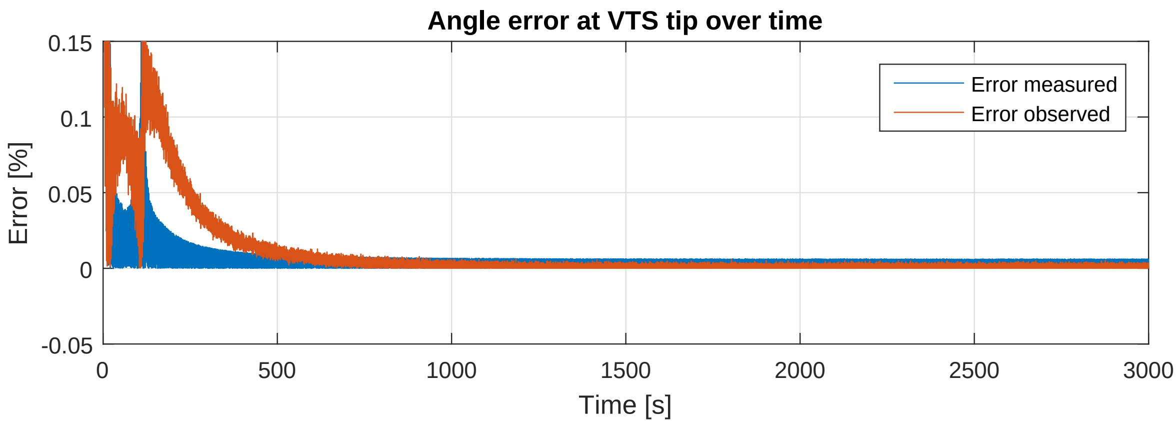

Figure D-4: Plot of angles

The error percentage, plotted in figure D-4, is calculating by taking the absolute value of the error between the original system and the observer system and dividing this over the absolute original angle. For the measured error the same approach is used, but using the absolute error between the measured (noise contaminated) error and the original angle. When the angle goes through zero during start up this results in some peak values. Looking at the figure it is confirmed that the offset error that occurs during start up is disappears and from 1500s the observations are more accurate than the measurements. This is confirmed by calculating the Root Mean Square Error (RMSE) from 1500s to 3000s. The RMSE of the measured angles and the original angles equals 0.002 deg, the RMSE of the observed angles and the original angles is $8.5 \cdot 10^{-4}$ deg.

Accelerations

Also the accelerations are checked at the tip of the system. The accelerations of the system first show some variations but then quickly approach zero as can be seen in figure D-8.

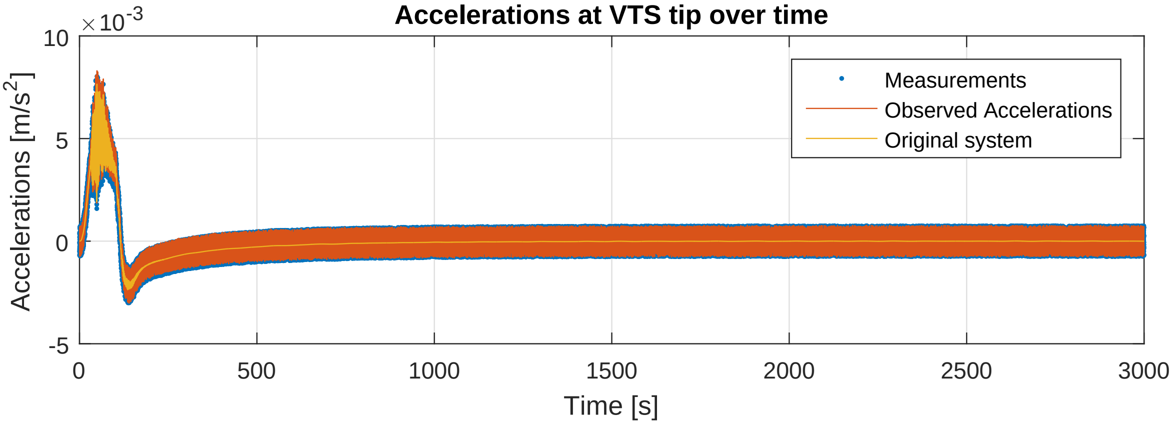

Figure D-5: Plot of accelerations

After the first second the accelerations rapidly vary for some time before they stabilize. In figure D-6 the start up behaviour is looked at more closely.

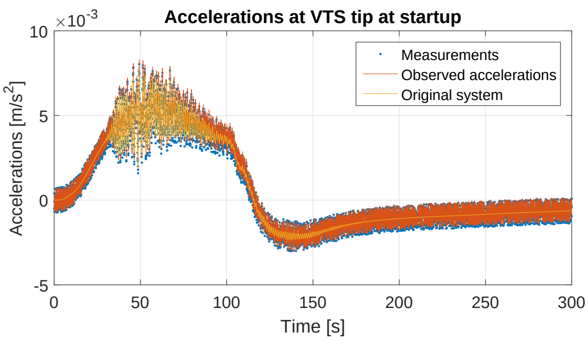

Figure D-6: Startup accelerations

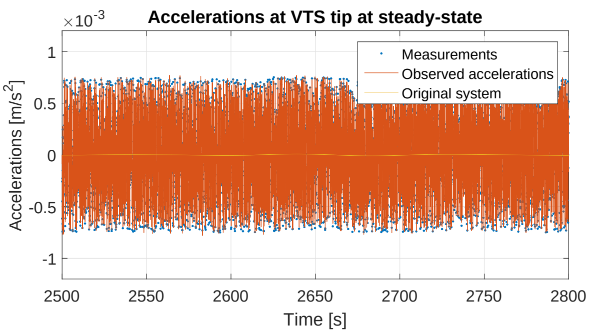

Figure D-7: Steady state accelerations

From this figure it is seen that with an amount of 20 measurements per second the accelerations vary very fast. This start up behaviour makes it hard for the KF to observe the system and it causes the observations to fully follow the measurements, since the measurement noise is small compared to the actual accelerations. In figure D-7 it can be seen that the filtered accelerations in the steady-state phase are still equal to the measurements.

Because the accelerations quickly approach zero the acceleration error, shown in figure D-8 shows very little information. The acceleration error is calculated the same way as the angle error from the previous subsection.
The accelerations reach a steady state after $1000s$ of simulating. Calculating the RMSE of both the original signal and the measurements and the original signal and the observed signal starting from $1000s$ emphasizes the bad fit. The RMSE of the original signal and the measurement signal is found to be $4.30 \cdot 10^{-4} m/s^2$. For the RMSE of the original signal and the observed signal a value of $4.27 \cdot 10^{-4} m/s^2$ is calculated, which makes the observed signal

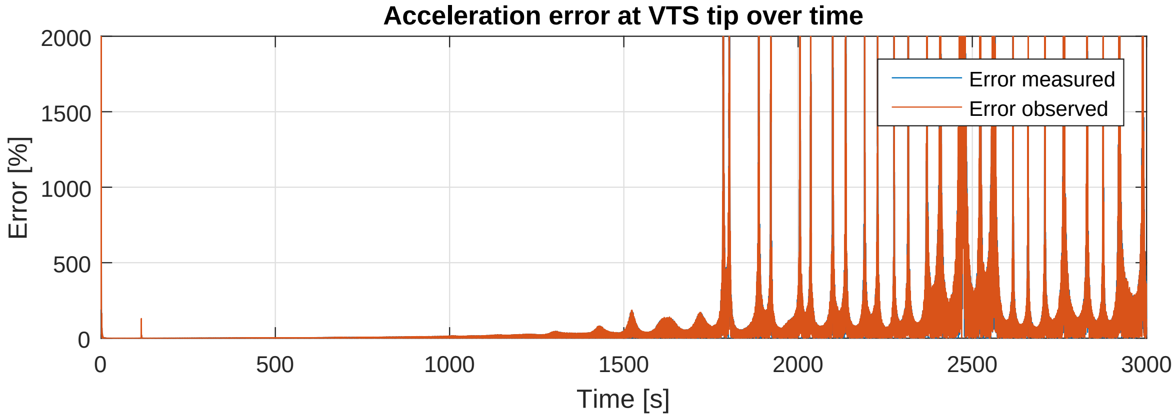

Figure D-8: Error in filtered angles compared to true values

compared to the original signal only slightly better than the measurement signal compared to the original signal.

Forces

The forces measured at the booster stations converge to a steady state in a way similar to the angles. From figure D-9 it is seen that, just like was the case with the angles, the force varies little after 1500s.

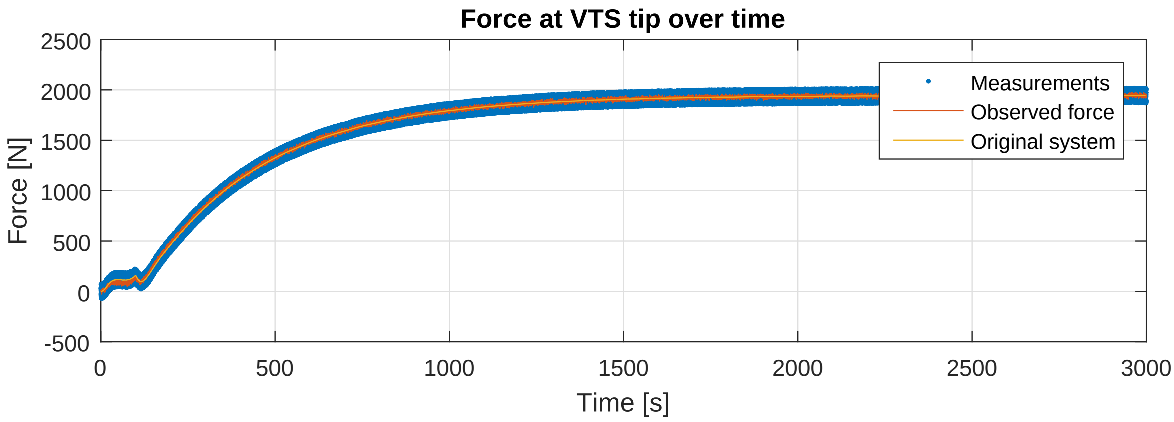

Figure D-9: Plot of force

When the start up and steady-state behaviour is observed more closely it can be seen that in the start up phase the observed force is offset from the original system. The closer observations are found in figures D-10 and D-11.

Even though during start up the observed force deviates from the original system, in steady state the force is observed well. From these figures the performance of the covariance values of the KF is also well demonstrated. The error covariance in the observer of the force is high compared to that of the observer covariance of the angles. But because the performance of the KF depends on the relation of the covariance of the measurements compared to the

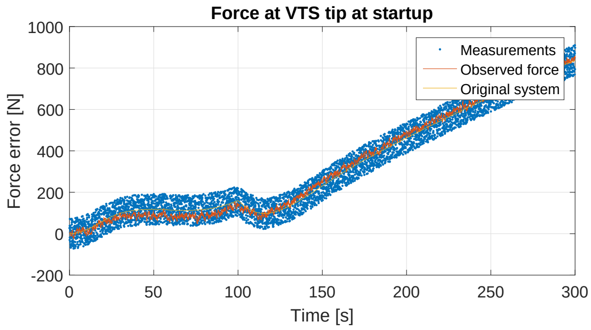

Figure D-10: Startup force

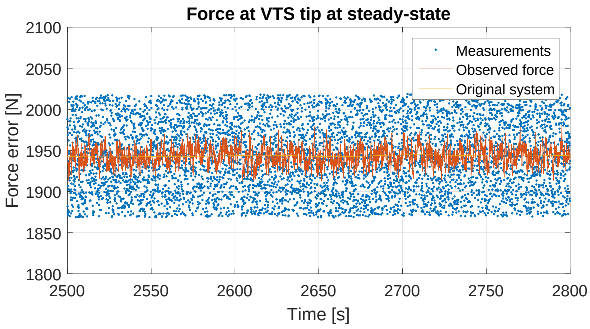

Figure D-11: Steady state force

covariance of the observer it is seen that the observed force is stable and of low error. The error between the measured signal and the original signal and the measured signal and the observed signal is shown in figure D-12.

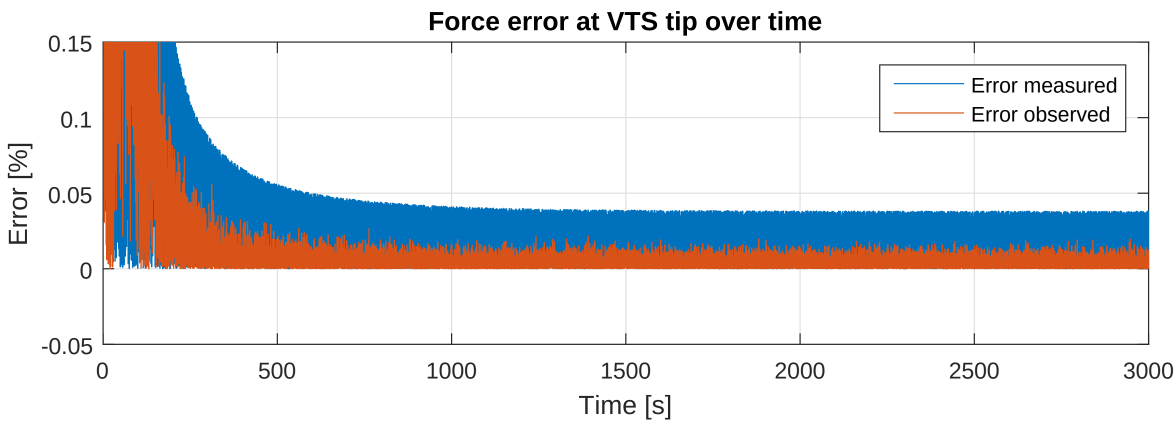

Figure D-12: Force errors

The error is calculated in the same way as it was calculated in subsection D-1-1. The error at start up is large, but after the force observations converge the error drops below the error percentage of the measurements. This is confirmed by calculations of the RMSE of the measured signal and the original signal and the RMSE of the observed signal and the original signal. Calculations of the RMSE are done from $1000s$ to $3000s$. The RMSE of the original signal and the measurement signal is found to be $42.8N$. For the RMSE of the original signal and the observed signal a value of $12.6N$ is found, which is an improvement of a factor 3.4.

D-1-2 Force adaptive Kalman filter

The force adaptive KF appears to work well. In this case the model used to generate data and the observer model are equal, which can create a result much better than would be the case if the model used to create measurements is a (partially) unknown data generation model.
The force used in the system will fully depend on the performance of the KF, so when the force process covariance constant is chosen to be much lower than the force measurement covariance constant. The most important observation that is made from these observations is

that the force adaptive KF works in a stable way and is able to combine measurements and observer estimations.

Appendix E

Additional simulation results

First the case of a simulation generated by VIVID is written. As a second an extra simulation of the riser going to steady-state with a constant current and with waves. Contrary to the case in subsubsection 5-2-3, no Vortex Induced Vibrations (VIV) are present, so no damping amplification factor has been used.

E-1 Constant current without vortex induced vibrations

In this extra case the ability to observe the system without VIV as it converges to a steady-state is checked. For this case the same simulation as in 3-4 is used. For the simulation data created by VIVID a time step of 0.1 seconds has been used.

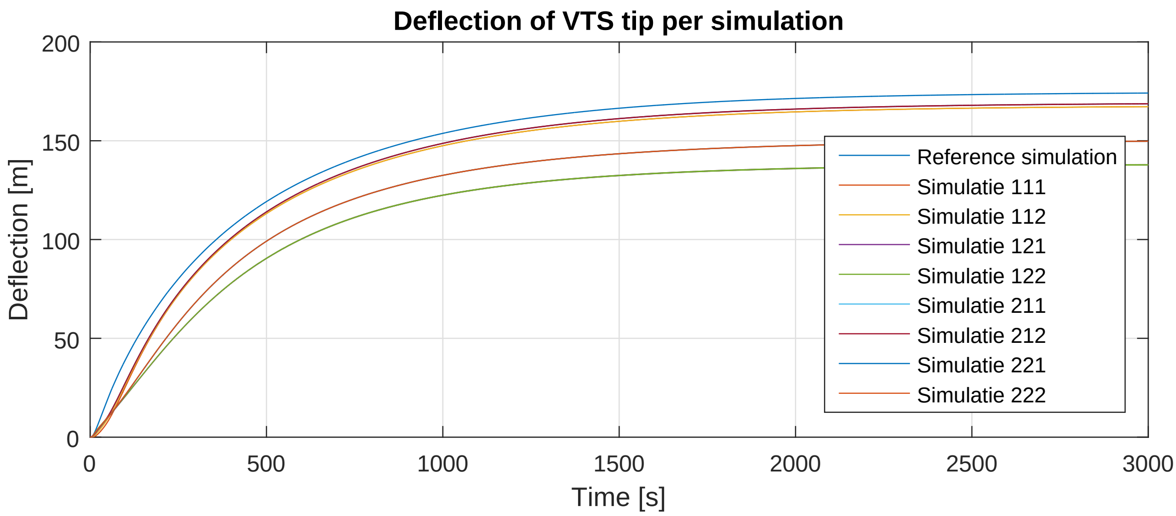

Figure E-1: Deflection of tip of VTS multiple simulations

The deflection of the tip of the system is seen in figure E-1. It can be seen that none of the observations manages to achieve a 100% fit compared to the original simulation. The observer approaches the original simulation but does not reach the same deflection.

Simulation noise	**Root Mean Square Error (RMSE)** $[m]$	**Variance Accounted For (VAF)** [%
low low low	1.805	99.5
low low high	1.553	99.6
low high low	4.466	99.7
low high high	4.703	99.7
high low low	3.358	99.2
high low high	3.263	99.2
high high low	2.443	99.7
high high high	2.594	99.7

Table E-1: RMSE and VAF for $3000s$ simulations

Appendix F

Full riser deflections

Simulation of the full length riser made by the approximate model at different time steps.

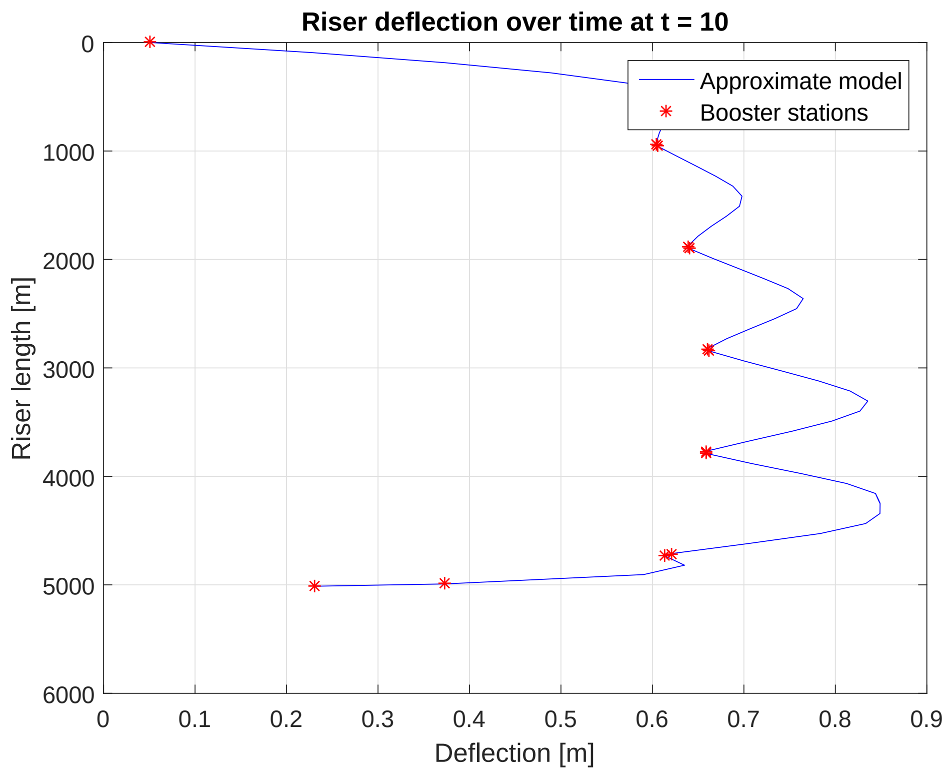

Figure F-1: Riser simulation at $t = 10s$

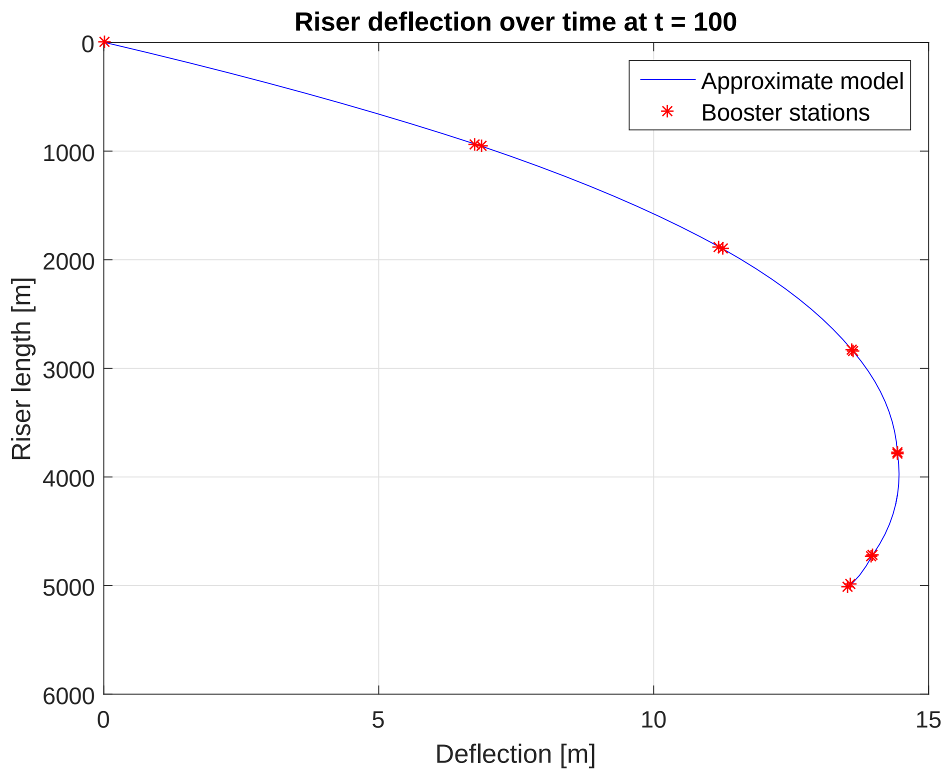

Figure F-2: Riser simulation at $t = 100s$

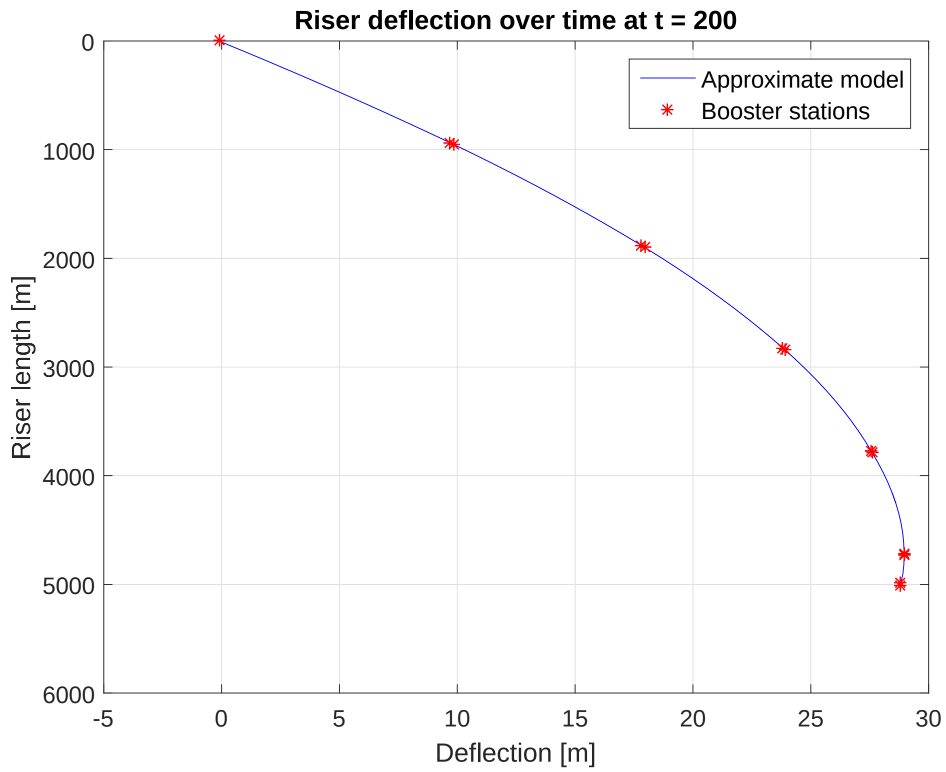

Figure F-3: Riser simulation at $t = 200s$

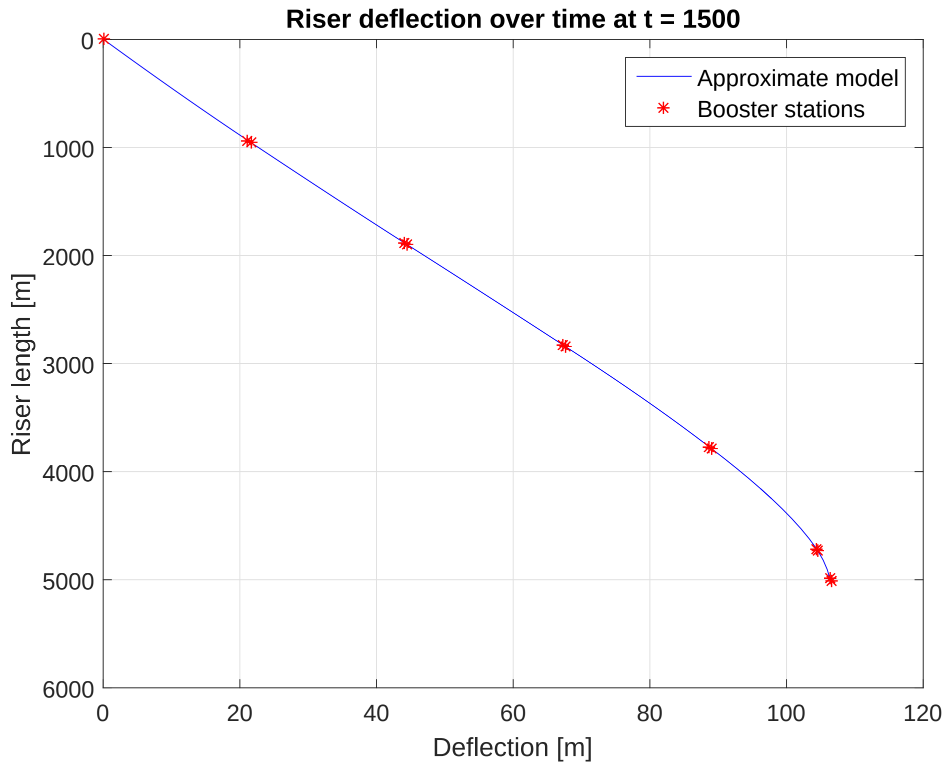

Figure F-4: Riser simulation at $t = 1500s$

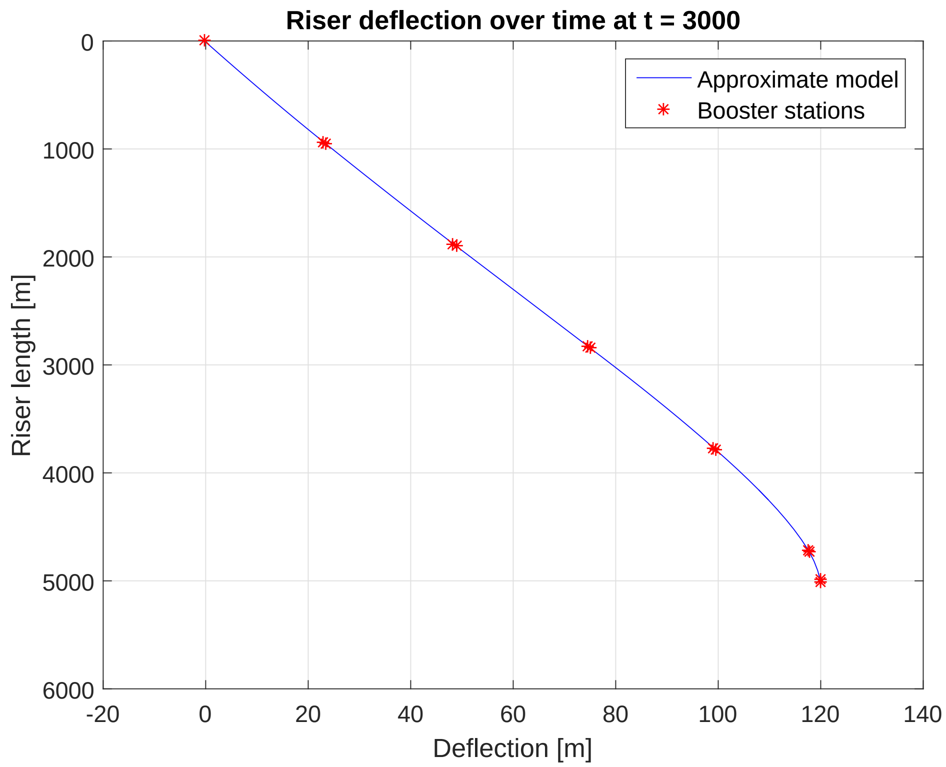

Figure F-5: Riser simulation at $t = 3000s$

Appendix G

Integrated accelerations

In this appendix the accuracy of an accelerometer without a model is tested. Accelerometer data is generated by the approximate model, run at a time step of $0.05s$ and with each section divided into elements with a maximum length of $100m$. The model is run for $3000s$ with a constant current of $0.5m/s$ evenly spread along the riser.
The accelerations are obtained at the tip of the system, the point of which the position needs to be monitored. The accelerations are integrated twice by calculating the area under the acceleration data after every time step to obtain the velocity and then the same is done to calculate the positions. It is assumed that the accelerations are linearly distributed over each time step.

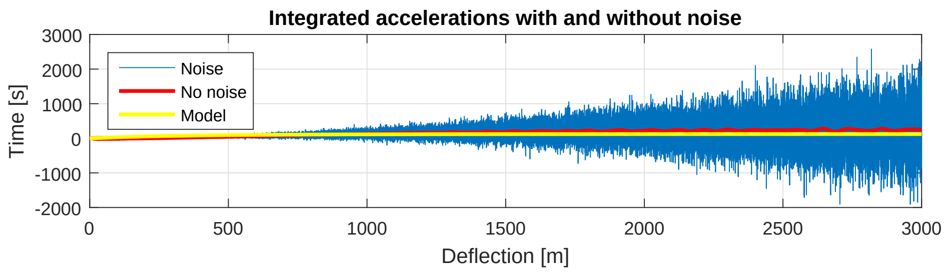

Figure G-1: Obtained positions after integration over $3000s$

In figure G-1 the resulting positions are seen, as well as the actual position of the system, shown as 'model'. When no noise at all is added to the accelerations, shown in the figure as 'no noise', the resulting offset is about two times the size of the actual offset of the model. This result can only be achieved by using data generated by the model, since measurement data is always contaminated with noise.
Measurement data is generated adding a random generated normal distributed signal, multiplied with the accelerometer standard deviation from 2-1, to the acceleration signal. When the measurement data is integrated to obtain the positions it is clear that no useful data can be obtained this way. It must be noted that the acceleration drift is lower than predicted in (Zwahlen et al., 2010), this can be explained by the low accelerations in the system. At

the start a peak, with an amplitude of $0.2m/s^2$, in accelerations is seen when the current is introduced. This peak decays and after about 50 seconds a deceleration with an amplitude of $1mm/s^2$ is left which goes to zero. Since all of the accelerations are very small, the drift is mainly created by sensor noise.

Bibliography

K. J. Åström and R. M. Murray. *Feedback Systems: An Introduction for Scientists and Engineers*, volume 36. 2008. ISBN 0691135762. doi: 10.1086/596297. URL http://caltechbook.library.caltech.edu/226/.

Australian Drilling Industry Training Committee Limited. *The drilling manual*. Fifth edition, 2015.

H. Bachmann, W. J. Ammann, F. Deischl, J. Eisenmann, I. Floegl, G. H. Hirsch, G. K. Klein, G. J. Lande, O. Mahrenholtz, H. G. Natke, H. Nussbaumer, A. J. Pretlove, J. H. Rainer, E.-U. Saemann, and L. Steinbeisser. *Vibration Problems in Structures*. Birkhäuser Basel, Basel, 1995. ISBN 978-3-0348-9955-0. doi: 10.1007/978-3-0348-9231-5. URL http://link.springer.com/10.1007/978-3-0348-9231-5.

G. Bishop and G. Welch. An introduction to the kalman filter. pages 1–16, 2001. ISSN 10069313. doi: 10.1.1.117.6808. URL http://old.shahed.ac.ir/references/kalman{_}filter{_}notes.pdf.

R. Blevins. Flow-induced vibration, 2001.

Blue Mining. Breakthrough Solutions for Mineral Extraction and Processing in Extreme Environments, 2013.

D. V. Brower, E. Field, A. Ave, and N. Prescott. Real Time Subsea Monitoring and Control Smart Field Solutions. *Subsea Rio 2004 Conference*, pages 1–13, 2004.

O. Cadet. Introduction to Kalman Filter and its Use in Dynamic Positioning Systems. In *DYNAMIC POSITIONING CONFERENCE*, Houston, 2003.

E. Carrera, G. Giunta, and M. Petrolo. *Beam structures : classical and advanced theories*. Wiley, Hoboken, N.J., 1st edition, 2011. ISBN 9781119978565.

T. Clarke, R. Jacques, A. Bisognin, C. Camerini, S. Damasceno, and T. Strohaecker. Monitoring the structural integrity of a flexible riser during a full-scale fatigue test. *Engineering Structures*, 33(4):1181–1186, 2011. doi: 10.1016/j.engstruct.2010.12.039. URL http://www.sciencedirect.com/science/article/pii/S0141029611000083{#}s000010.

I. G. Currie and W. L. Cleghorn. Free lateral vibrations of a beam under tension with a concentrated mass at the mid-point. *Journal of Sound and Vibration*, 123(1):55–61, 1988. ISSN 10958568. doi: 10.1016/S0022-460X(88)80077-4.

J. J. De Wilde and R. H. M. Huijsmans. Laboratory investigation of long riser VIV response. *Proceedings of the International Offshore and Polar Engineering Conference*, pages 511–516, 2004. ISSN 10986189. URL http://www.scopus.com/inward/record.url?eid.

S. Erlicher, L. Bonaventura, and O. Bursi. The analysis of the Generalized-a method for non-linear dynamic problems. *Computational Mechanics*, 28:83–104, 2002. doi: 10.1007/s00466-001-0273-z>. URL https://hal.archives-ouvertes.fr/hal-00345290.

A. Gelb, J. F. Kasper, R. A. Nash, C. F. Price, and A. A. Sutherland. *APPLIED OPTIMAL ESTIMATION*. THE M.I.T. PRESS, Massachusets, 16th edition, 1974. ISBN 0-262-57048-3.

B. Glisic. *Fiber optic sensors for subsea structural health monitoring*. 2013. ISBN 9780857093417. doi: 10.1533/9780857093523.3.434. URL http://www.sciencedirect.com/science/article/pii/B9780857093417500170.

A. Heemink. Rekenen met Onzekerheid. Delft University Press, Delft, 1991. ISBN 90-6275-750-2/CIP.

D. Heydon. OTC 22938 Deepsea Mining - Heading Back Down to 15 , 000 Feet. (May):1–4, 2012.

R. Hibbeler. *Mechanics of Materials*, volume 8. 2011. ISBN 9780136022305. doi: 10.1017/CBO9781107415324.004.

Honeywell. GG1320AN Digital Laser Gyro, 2016. URL www.honeywell.com.

International Marine Contractors Association. Deep Water Acoustic Positioning. Technical Report July, 2014.

T. Irvine. Transverse Vibration of a Cantilever Beam Subjected To a Constant Axial load Via the Finite Element Method. pages 1–21, 2003.

T. Irvine. Transverse Vibration of a Beam Via the Finite Element Method, Revision E. (E), 2008.

R. Jacques, T. Clarke, S. Morikawa, and T. Strohaecker. Monitoring the structural integrity of a flexible riser during dynamic loading with a combination of non-destructive testing methods. *NDT and E International*, 43(6):501–506, 2010. ISSN 09638695. doi: 10.1016/j.ndteint.2010.05.005. URL http://www.sciencedirect.com/science/article/pii/S0963869510000587http://dx.doi.org/10.1016/j.ndteint.2010.05.005.

J. Journée and W. Masie. *Offshore Hydromechanics*. Number January. 2001.

D. J. Jwo and T. S. Cho. A practical note on evaluating Kalman filter performance optimality and degradation. *Applied Mathematics and Computation*, 193(2):482–505, 2007. ISSN 00963003. doi: 10.1016/j.amc.2007.04.008.

K. Kaasen, H. Lie, F. Solaas, and J. Vandiver. Norwegian Deepwater Program: Analysis of Vortex-Induced Vibrations of Marine Risers Based on Full-Scale Measurements. *Proceedings of Offshore Technology Conference*, pages 1–11, 2000. ISSN 01603663. doi: 10.4043/11997-MS.

M. Karayaka, W. Ruf, and S. Natarajan. Steel Catenary Riser Response Characterization With On-line Monitoring Devices. *International Conference on Offshore Mechanics and Arctic Engineering*, pages 1–12, 2009.

E. H. Kennard. Irrotational Flow of Frictionless Fluids, Mosty of Invariable Density. 1967.

J. M. Ko and Y. Q. Ni. Technology developments in structural health monitoring of large-scale bridges. *Engineering Structures*, 27(12 SPEC. ISS.):1715–1725, 2005. ISSN 01410296. doi: 10.1016/j.engstruct.2005.02.021.

G. L. Kuiper and A. V. Metrikine. Dynamic stability of a submerged, free-hanging riser conveying fluid. *Journal of Sound and Vibration*, 280(3-5):1051–1065, 2005. ISSN 0022460X. doi: 10.1016/j.jsv.2004.09.024.

C. M. Larsen. Vortex Induced Vibrations: A short and incomplete introduction to fundamental concepts.

B. Li, H. Wang, X. Shen, Y. Yan, F. Yang, and F. Hua. Deep-water riser fatigue monitoring systems based on acoustic telemetry. *Journal of Ocean University of China*, 13(6):951–956, 2014. ISSN 19935021. doi: 10.1007/s11802-014-2487-7.

J. Lienemann, A. Greiner, E. B. Rudnyi, J. G. Korvink, K. Georges, and D. Freiburg. Linear Beam Model. pages 1–8, 2004.

X. Liu and A. Goldsmith. Kalman filtering with partial observation losses. *Proceedings of the IEEE Conference on Decision and Control*, 4(Lmi):4180–4186, 2004. ISSN 01912216. doi: 10.1109/CDC.2004.1429408.

P. F. McLauchlan and D. W. Murray. Variable State Dimension Filter applied to Active Camera Calibration, 1993.

S. Miao, R. Veerman, E. Koenders, and A. Knobbe. Modal analysis of a concrete highway bridge: Structural calculations and vibration-based results. *Proceedings of the 6th International Conference on Structural Health Monitoring of Intelligent Infrastructure*, (December), 2013.

S. Natarajan, H. Howells, D. Deka, and D. Walters. Optimization Of Sensor Placement To Capture Riser VIV Response. pages 1–7, 2006.

N. M. Newmark. A Method of Computation For Structural Dynamics. *Journal of the Engineering Mechanics Division*, 1959.

R. H. M. Ogink and A. V. Metrikine. A wake oscillator with frequency dependent coupling for the modeling of vortex-induced vibration. *Journal of Sound and Vibration*, 329(26): 5452–5473, 2010. ISSN 0022460X. doi: 10.1016/j.jsv.2010.07.008. URL http://dx.doi.org/10.1016/j.jsv.2010.07.008.

J. R. Pedrazzani, S. M. Klute, D. K. Gifford, A. K. Sang, and M. E. Froggatt. Embedded and surface mounted fiber optic sensors detect manufacturing defects and accumulated damage as a wind turbine blade is cycled to failure. *Luna Innovations Inc*, 2012.

D. Pipa, S. Morikawa, G. Pires, C. Camerini, and J. M. Santos. Flexible riser monitoring using hybrid magnetic/optical strain gage techniques through RLS adaptive filtering. *Eurasip Journal on Advances in Signal Processing*, 2010, 2010. ISSN 16876172. doi: 10.1155/2010/176203.

X. P. Qing, S. Yuan, and Z. Wu. Current Aerospace Applications of Structural Health Monitoring in China. 2012. URL http://www.ndt.net/article/ewshm2012/papers/we3a4.pdf.

W. H. Ray. *Advanced process control*. McGraw-Hill, Michigan, 1981. ISBN 0070512507.

C. C. Remsing. Linear Control, 2006. URL https://www.ru.ac.za/media/rhodesuniversity/content/mathematics/documents/ccrlecturenotes/CCR-LN-LC.pdf.

P. Smit, T. Bartstra, S. Verichev, and R. Rotteveel. Breakthrough Solutions for Mineral Extraction and Processing in Extreme Environments. (604500):1–42, 2014.

D. solutions. No Title, 2016. URL http://www.dgi-solutions.com/solutions/riser-gimbal-systems/.

C. Sparks. Effective tension in pipes and risers : A bold but simple concept. *World oil online*, 233(December):1–8, 2012.

V. Stanislav, L. D. Jonge, W. Boomsma, and R. Norman. Deep Sea Mining : From Exploration To Exploitation. pages 126–137, 2014.

V. Thomée. From finite differences to finite elements A short history of numerical analysis of partial differential equations. *Journal of Computational and Applied Mathematics*, 128 (1-2):1–54, 2001. ISSN 03770427. doi: 10.1016/S0377-0427(00)00507-0. URL http://linkinghub.elsevier.com/retrieve/pii/S0377042700005070.

W. T. Thomson and M. D. Dahleh. *Theory of Vibration with Applications*. Fifth edition, 1998. ISBN 9780470748732.

A. Tomczak. Modern Methods Of Underwater Positioning Applied In Subsea Mining. 2011.

Valeport. Model 106 Current Meter Datasheet, 2016. URL http://www.valeport.co.uk/Products/CurrentMeters.aspx.

M. van Dort. *Monitoring of the slurry density along the length of the VTS*. PhD thesis, Technical University of Delft, 2016.

H. Vella. Balancing economics & the environment: deep sea mining the Clarion-Clipperton zone - Mining Technology, 2013. URL http://www.mining-technology.com/features/featurebalancing-economics-the-environment-deep-sea-mining-the-clarion-clipperton-zone-

M. Verhaegen and V. Verdult. *Filtering and System Identification : A Least Squares Approach.* Cambridge University Press., Cambridge, 2007. ISBN 9780521875127. URL http://web.b.ebscohost.com.tudelft.idm.oclc.org/ehost/ebookviewer/ebook/bmxlYmtfXzE5NDMwMl9fQU41?sid.

O. J. Woodman. An introduction to inertial navigation. 2007. URL https://www.cl.cam.ac.uk/techreports/UCAM-CL-TR-696.pdf.

L. Xu, H. Wang, and S. Jiang. Fatigue multi-point wireless monitoring system of water-insulated tube, 2011.

H. Yang and H. Li. Parametric Resonance of the Free Hanging Marine Risers in Ultra-Deep Water Depths. *Computational Structural Engineering*, pages 119–126, 2009. doi: 10.1007/978-90-481-2822-8_13. URL http://www.springerlink.com/index/10.1007/978-90-481-2822-8{_}13.

L. Yu, N. Neretti, and N. Intrator. Robust Motion Estimation Improves Underwater Sonar Accuracy. 2005. URL https://www.cs.tau.ac.il/{~}nin/papers/cihsps05Yu.pdf.

P. Zwahlen, A. M. Nguyen, Y. Dong, F. Rudolf, M. Pastre, and H. Schmid. Navigation grade mems accelerometer. *Proceedings of the IEEE International Conference on Micro Electro Mechanical Systems (MEMS)*, pages 631–634, 2010. ISSN 10846999. doi: 10.1109/MEMSYS.2010.5442327.

Glossary

List of Acronyms

SMT	Seafloor Mining Tool
MSV	Mining Support Vessel
VTS	Vertical Transport System
OMA	Operational Modal Analysis
SONAR	SOund Navigation And Ranging
LBL	Long Baseline system
SBL	Short Baseline system
USBL	Ultra Short Baseline system
IMU	Inertial Measurement Unit
DSM	Deep Sea Mining
VIV	Vortex Induced Vibrations
FEM	Finite Element Method
EKF	Extended Kalman Filter
KF	Kalman Filter
OMA	Operational Modal Analysis
EMA	Experimental Modal Analysis
UKF	Unscented Kalman Filter
EnKF	Ensemble Kalman Filter
GPS	Global Positioning System

MDOF	Multiple Degrees Of Freedom
SDOF	Single Degree Of Freedom
DOF	Degree Of Freedom
DOFs	Degrees Of Freedom
ODE	Ordinary Differential Equation
MEMS	MicroElectro Mechanical Systems
RMS	Root Mean Square
VAF	Variance Accounted For
RMSE	Root Mean Square Error

List of Symbols

ϵ	Axial strain
$\mathbf{\Phi}$	Discrete state-space system update matrix
$\mathbf{\Psi}$	Discrete state-space input update matrix
ν	Kinematic viscosity
ρ	Sea water density
σ	Bending stress
θ	Rotation at node
ξ	Dimensionless distance
ζ	Damping ratio
$\hat{x}_k$	Kalman filtered states
$\bar{x}$	State-space deflections and rotations in x-direction
$\mathbb{L}$	Lagrangian
$\mathbb{T}$	Kinetic energy
$\mathbb{V}$	Potential energy
$\mathbf{A}$	Prediction matrix
$\mathbf{B}$	External influence matrix
$\mathbf{D_t}$	Detectability matrix
$\mathbf{H}$	Observer update matrix
$\mathbf{I}$	Identity matrix
$\mathbf{K}_m$	Stiffness matrix
$\mathbf{K}_p$	Geometric stiffness matrix
$\mathbf{M}$	Mass matrix
$\mathbf{O}$	Observability matrix

C_d	Drag coefficient
C_m	Inertia coefficient
D	Diameter
d_i	Switching term used to add or remove observer states
dL	Element length
$E\{v_k\}$	Expected value of v_k
I_{zz}	Inertia
k	Beam curvature
K_k	Kalman gain
L	Cylinder length
M	Bending moment
m_a	Added mass
m_c	Element combined mass
Q	Process noise covariance matrix
q	Distributed force load
R	Measurement noise covariance matrix
$R(t)$	Reaction force
u_{cu}	Flow velocity
v	Motions in z direction
v_k	Gaussian distributed white process noise
w	Motions in x direction
w_k	Gaussian distributed white measurement noise
x_w	Deflection and rotation vector in x direction
y_k	Observer states
z_k	Measurement states
A	Cut-through area
E	Yougs modulus
e	Residual
F	Force
g	Gravitational constant
I	Inertia
P	Error covariance matrix
Re	Reynolds number
T	Tension force
V	Shear force
V	Volume
$_0$	Initial conditions
$_{cu}$	Current components
$_{drag}$	Drag component
$_{in}$	Inner riser

$_{max}$	Maximum
$_{o}$	Outer
$_{sea}$	Seawater
$_{sl}$	Slurry
$_{st}$	Steel
$_{tip}$	Last node of the riser
$^{-}$	A-priori state estimate
^{T}	Transform of a matrix
$^{\circ}$	Degrees